Investigating Electrostatics and Dynamics in Confinement and Constructs Using Two-Dimensional Infrared Spectroscopy and Molecular Simulations

by

Aaron Michael White

A dissertation submitted in partial fulfillment
of the requirements for the degree of
Doctor of Philosophy
(Chemistry)
in the University of Michigan
2016

Doctoral Committee:

Associate Professor Kevin J. Kubarych, Chair
Professor Eitan Geva
Associate Professor Jennifer P. Ogilvie
Professor Roseanne J. Sension

To my parents

Acknowledgements

I am truly thankful for the help and support from numerous people throughout my graduate career that made this work possible. My advisor, Kevin Kubarych, has always encouraged me to pursue my scientific interests and helped me greatly with not only his outstanding breadth of knowledge, but also the ease with which he can explain even the most complicated of topics. I would also like to thank several past and present group members in particular: Josef Dunbar, for being a good friend and lab mate who was always ready to help solve any problems I had, Derek Osborne for teaching me a great deal about 2D-IR and introducing me to a good deal of Michigan football lore, Matt Ross for his leadership and assistance on the peptide project, and Laura Kiefer for many useful discussions about science.

I also have to thank Dotie Sipowska for being a wonderful mentor and colleague to teach with for so many semesters. Fangting Yu and Karl Koebke were invaluable for their hard work synthesizing and labeling the *de novo* peptide samples.

I would also like to thank my friends and family, specifically my parents, Mike and Jackie White, for supporting and encouraging me throughout my education.

Table of Contents

List of Figures

List of Tables

Abstract

Understanding the ultrafast dynamics of enzymes is required to fully explain what makes them such efficient catalysts. Two-dimensional infrared (2D-IR) spectroscopy along with molecular modeling helps provide a more complete description of the environment of enzyme active sites and other related systems.

A carbonyl-labeled copper site in a *de novo* peptide exhibits vibrationally driven nonequilibrium dynamics when characterized using 2D-IR spectroscopy. The source of the dynamics is found to be the coupling of the CO stretching mode to the CuCO bending mode, enhanced by distortions to the histidine side chains binding the copper. QM/MM calculations show the source of the distortions to be primarily from electrostatic interactions with the peptide.

Using similar calculations, but with a refined sampling of starting structures, other *de novo* peptides are modeled to identify a candidate that will show different nonequilibrium dynamics from the original metalloenzyme. The selected enzyme is more catalytically active, and calculations predict a smaller coupling between the CO stretching and CuCO bending modes. This prediction is confirmed using 2D-IR, where the nonequilibrium dynamics have a smaller amplitude, but occur on the same time scale.

Several thiocyanate salts in the Hofmeister series are studied in neat D_2O and with alpha-cyclodextrin (a-CD). In neat D_2O, 2D-IR shows slightly faster spectral diffusion for kosmotropes and slower spectral diffusion for chaotropes. When a-CD is introduced to the system, an additional slowly decaying component of the FFCF is found. The

presence of the slower dynamics indicates the nitrogen in thiocyanate is not solvent exposed, but embedded in the interior of the a-CD.

A combination of 2D-IR and molecular modeling was also needed to characterize the structure of a labeled crown either with a nearby sodium thiocyanate contact ion pair. The spectral diffusion of the metal carbonyl label shows dynamics occurring on a slower time scale than the vibrational lifetime of the probe. DFT calculations show that two different conformations of the thiocyanate ion around the crown ether have similar energies, but produce different CO frequencies. The time to sample these states is longer than the vibrational lifetime of the metal carbonyl.

Chapter 1

Introduction

1.1 Nanoscale Confinement and Macromolecular Constructs

Enzymes are an important area of research with many applications due to their ability to selectively catalyze reactions with great efficiency.[1, 2] The ability to fully understand what makes these natural catalysts so efficient would lead to great advances in adapting them to accelerate reactions not necessarily needed in biology. Despite the advances made in our understanding of enzymes, there is still debate over some of the essential methods by which enzymes increase reaction rates – namely whether structural dynamics in proteins are important to catalysis or if an understanding of the energetic landscape of a system can explain reactivity differences.[3-6] Reducing the height of the barrier between reactants and products is clearly important in catalysis, but with a lower barrier other factors, such as recrossing of products back into reactants[7] and fluctuations in the size and shape of the barrier due to environmental fluctuations,[8, 9] have a larger influence on the system. Determining how each of these contribute to the catalytic pathway will allow for the design of better artificial enzymes.

There are two main types of *de novo* or "from the beginning" peptide design – from the "top down", where an existing enzyme is modified to incorporate a different metal or otherwise alter its function, and "bottom up" where a well-defined structure not necessarily based on any natural protein is modified to improve catalytic activity for a specific reaction.[1] Working with artificial enzymes allows us to selectively modify residues in the enzyme to more fully understand the electrostatic and steric effect the substitution has, potentially yielding insight into the dynamics play in the catalysis. However, choosing the residue to change and what to change it to will have limited

efficiency without a rationale for why the alterations are being made. This inspiration could come from nature, other *de novo* designs, or from simulations. As more information is gathered from the engineered peptides, better models can be produced, resulting in a more efficient cycle of designing an enzyme, synthesizing it, and testing it for the desired properties.

Enzymes are macromolecular constructs composed of useful and modifiable units, amino acids, that can be changed or modified to suit the needs of a particular project. For example, if a bulkier amino acid, such as leucine or tryptophan, was thought to be crowding the active site of an enzyme it could be changed to a smaller amino acid, such as alanine. Constructs can be used in other ways, such as modifying a well-studied molecule to include a probe to gain insight into the original molecule or another nearby species to better understand the nearby dynamics. Many of these constructs have been focused on biological applications or catalysis, including using isotope labels on the backbone of a helical peptide to monitor the nonequilibrium reorganization as it folds from an initially perturbed state,[10] adding cysteine-based labels to sense the electrostatics of a protein,[11] labeling silica nanoparticles to determine the distance-sensitivity of the probes,[12] and attaching a catalyst that doubles as a vibrational probe to a monolayer-forming molecule to compare the dynamics of the probe in solution, in a monolayer exposed to the air, and in a monolayer in solution.[13]

Macromolecular constructs are often studied alongside confinement, where two or more molecules are held together by non-covalent forces. These forces often involve water – where hydrophobic interactions can force molecules or ions into less polar environments such as a bicelle[14] or cyclodextrin.[15] The dynamics of the confined probe differ from the bulk, providing insight into the crowded or interfacial environment they occupy. These confined species are inherently able to fluctuate between environments, as they are not covalently bonded. The timescale to sample these environments is short, on the order of picoseconds, making them ideal systems to study with ultrafast infrared spectroscopy, where the vibrational lifetime of the confined probes is on the same timescale. This allows us to study many different systems, including the rebinding of a

dissociated carbonyl confined to the interior of a protein,[16] water confined in a reverse micelle[17] and ionic clusters in aqueous solutions.[18]

1.2 Infrared Spectroscopy

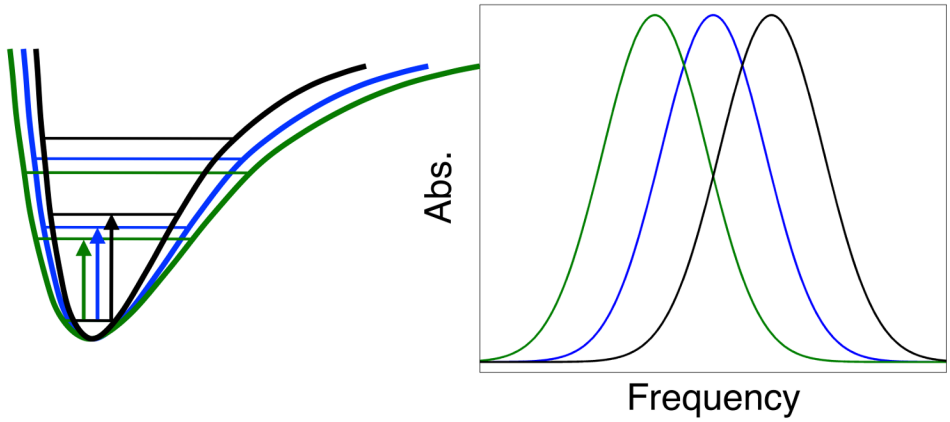

Figure 1.1 As the potential energy of the vibrational mode changes (left) the frequency will shift as well (right).

Infrared (IR) spectroscopy allows us to probe the bonds in a molecule and obtain information about their environment. Molecules absorb light in the infrared frequency range to excite a vibrational mode that will change as the environment of the mode varies as shown in Figure 1.1. This allows the infrared frequency to directly report on changes the probe experiences, such as the presence of an electric field, hydrogen bonding, or the polarity of the solvent. Each individual molecule will be in a slightly different environment, so when we probe a sample with IR light an ensemble average is detected, leading to an increased linewidth. This explains why the same molecule will have relatively narrow peaks in nonpolar solvents compared to the broad bands in more polar solvents – the movement of polar molecules will change the electrostatic environment of the probe more than a nonpolar solvent. For example, in water whether a partially positive hydrogen atom is near the probe or a partially negative oxygen is, the electrons on the probe will be slightly attracted or repelled resulting in a different frequency for the two states. Conversely, in a nonpolar alkane such as hexane the large number of C-H bonds will appear mostly identical to the probe and have essentially identical electrostatics, so there will be a smaller distribution of frequencies.

The rate at which the frequency distribution is sampled can reveal much about the molecules surrounding the probe. If the nearby molecules are moving quickly, as they are expected to in the bulk solvent, the frequencies will change relatively quickly. If the solvent molecules near the probe are not able to move quickly, for example if they are constrained or confined, the frequencies will change more slowly, as the environment will remain largely static.[19-25] The rate of these fluctuations cannot be determined by linear spectroscopy, as there is no unique way to decompose the line broadening mechanism based on a one-dimensional spectrum.[26] To discern how the system changes over time, a multidimensional spectroscopy such as two-dimensional infrared (2D-IR) spectroscopy can be used.

1.3 Two-Dimensional Infrared Spectroscopy

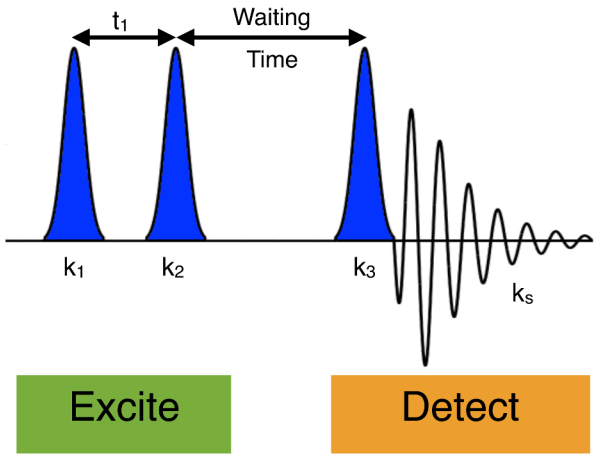

Figure 1.2 Pulse sequence for 2D-IR spectroscopy. The sample is excited by k_1 and k_2 which are separated by a time t_1 followed by a waiting time where dynamics can occur. The sample then interacts with k_3 and emits k_s in the detection time.

Two-dimensional infrared (2D-IR) spectroscopy is a third-order nonlinear process involving three field-matter interactions, as shown in Figure 1.2.[27] Briefly, the technique correlates two different frequencies – the excitation frequency, where the system starts, and the detection frequency, which is obtained after some waiting time during which the system is allowed to evolve. The detection frequency is obtained using a spectrometer and the excitation frequency is obtained by scanning the time delay between the first two pulses (with wave vectors k_1 and k_2) that interact with the sample,

separated by a time delay t_1 and Fourier transforming the complex detected signal field with respect to this delay.[28] The spectra are plotted as a function of these two frequencies to yield a 2D spectrum, such as the one shown in Figure 1.3C.

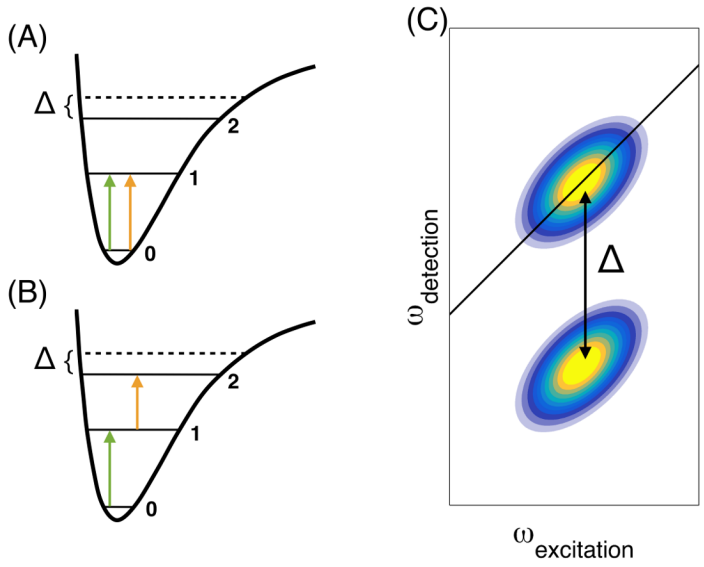

Figure 1.3 Cartoon 2D spectrum showing how anharmonicity may be observed using 2D-IR. (A) is the pathway that produces the diagonal peak, where both the excitation (green) and detection (orange) frequencies probe the 0-1 transition. (B) shows how an off-diagonal peak can arise from a single oscillator, where the excitation frequency probes the 0-1 transition and the detection frequency probes the 1-2 transition, which is lower in frequency due to the anharmonicity of the oscillator. The anharmonicity is measurable in the 2D spectrum (C) as the excited state absorption peak will appear below the diagonal, shifted by exactly the anharmonicity in the detection frequency axis.

In addition to the 0-1 transition probed by linear spectroscopy, 2D-IR allows for the exploration of higher transitions in the oscillators that are reachable because of the third-order nonlinear nature of the light-matter interactions.[27, 29] Prior to any interactions with the laser pulses, the probed vibrational mode is in the ground state, and after the first two field-matter interactions the system either returns to the ground state or is promoted to the first excited state, where it evolves as a population during the waiting time. The third field-matter interaction can then either excite the already vibrationally excited molecule further, probing the 1-2 transition as shown in Figure 1.3B, or it can stimulate emission to the ground state, thus probing the 0-1 transition as shown in Figure 1.3A. The frequency of the 1-2 transition is generally lower than the 0-1 transition due to the anharmonicity of the oscillator, which is usually a constant value

for each vibrational mode. If the anharmonicity is large enough, the excited state absorption peak will be distinctly separated from the diagonal band, as shown in Figure 1.3C. For many molecules in the condensed phase, the anharmonicity is comparable to the homogeneous (antidiagonal) linewidth, making it difficult or impossible to resolve in an absolute value spectrum. In an absorptive spectrum, which is created by summing the real parts of the rephasing ($k_s = -k_1 + k_2 + k_3$) and non-rephasing ($k_s = +k_1 - k_2 + k_3$) spectra, the two peaks will have opposite signs, so they are resolvable.[27, 30, 31] The peak shape and amplitude of 2D spectra may change as the waiting time is varied, but the peak positions should remain constant.

2D-IR spectra are very rich, and the various aspects of peak positions and shapes can be directly related to molecular structure and dynamics. For example, the relative widths of the diagonal and antidiagonal components of a peak at early waiting times provide insight into inhomogeneous and homogeneous contributions, respectively. If there are a large number of microenvironments that the probe is likely to occupy, the peak exhibits a significant inhomogeneous (diagonal) linewidth because of the different frequencies associated with the various environments (Figure 1.3C).[32] The anti-diagonal line width reflects the homogeneous dephasing that arises from very rapid frequency fluctuations or from pure dephasing. Since homogeneous broadening is non-reversible it cannot be "rephrased" and the 2D spectrum reflects this loss of correlation by exhibiting a rounder shape (Figure 1.4B). More inhomogeneously broadened spectra are associated with polar environments, where more distinct microenvironments are present, while homogeneously broadened spectra are frequently seen in nonpolar solvents where the lack of electrostatic modulations of the probe result in fewer spectroscopically distinct environments.[33]

If more than one diagonal peak is present in a 2D spectrum, it is possible to see energy transfer or coupling between the modes. If two vibrational modes in a molecule share a ground state, such as between multiple modes of coupled metal carbonyls, there will be cross-peaks between the diagonal peaks corresponding to the individual vibrational modes at early waiting times.[27, 32, 33] This coupling pattern can help to

deconvolute a congested spectrum and assign peaks to vibrational modes.[34, 35] Polarization can be used to determine the relative transition dipole moment directions, providing further structural constraints.[36] The time dependence of cross peaks can also reveal information about vibrational energy transfer, which can be either long-range Förster-like transfer[18] or short range intramolecular vibrational redistribution (IVR).[37] Cross peak dynamics been used in small peptides, for example, to track transfer between different amide bands.[38]

1.4 Spectral Diffusion

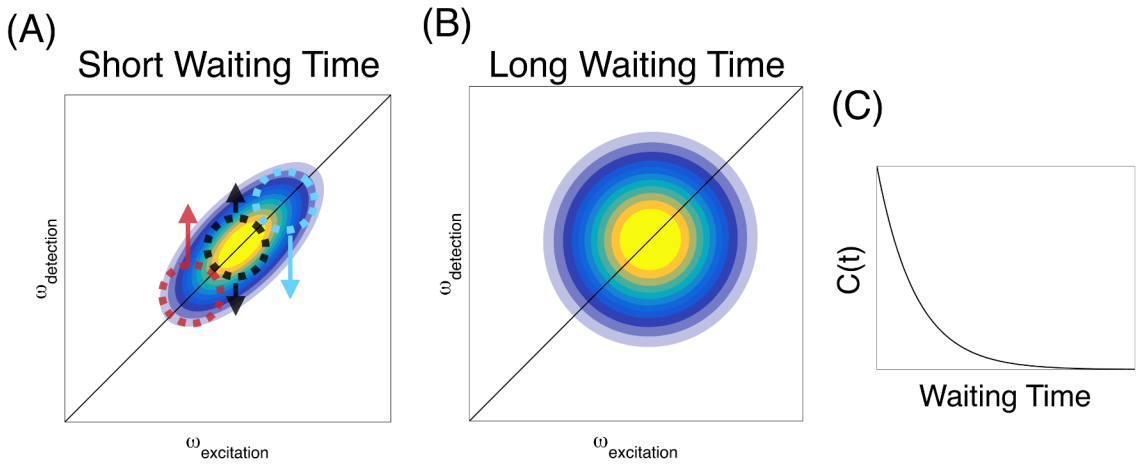

Figure 1.4 At early waiting times, the excitation and detection frequencies are well correlated (A), as frequencies have not been allowed enough time to fully sample all available microstates. (B) The frequencies fluctuate more and more as the waiting time is increased, until there is no correlation between the excited and detected frequency. This loss of correlation can be expressed in a frequency fluctuation correlation function (C) that decays exponentially.

Although a good deal of information can be obtained from a single 2D spectrum, the real power of the technique is providing insight into the ultrafast dynamics of a system by seeing how the spectra change as the waiting time is varied. At each waiting time, the excitation and detection frequency are correlated in the spectrum, making it possible to extract the frequency-fluctuation correlation function (FFCF), which provides a quantitative measurement for how fast the frequencies in a 2D-IR band are changing.[30, 31] The FFCF is commonly obtained by analyzing the lineshape of the absorptive spectrum, where the relative contributions from homogeneous and

inhomogeneous broadening lead to an asymmetrical lineshape.[39-42] For example, the slope of a line connecting the maxima of a peak can be inverted to yield an exponential decay such as Figure 1.4C.[31, 42-46] An alternative method of obtaining the FFCF that does not require absorptive spectra is the inhomogeneity index method,[30] where the normalized difference between the moduli of the rephasing and nonrephasing spectra, A_R and A_{NR} respectively, is calculated over the appropriate spectral range at each waiting time:

$$C(t) = \sin\left[\frac{\pi}{2}\left(\frac{A_R - A_{NR}}{A_R + A_{NR}}\right)\right]$$

The FFCF decays exponentially, as shown in Figure 1.4C because as the waiting time is increased a probe will be more likely to have sampled a different environment and experience a change in frequency. This diffusion of a frequency over the spectrum is known as spectral diffusion. Spectral diffusion is widely studied and provides insight into the environment of the probe and how quickly that environment changes.[47-55] The FFCF does not always decay as a single exponential function, for example in CO bound to horseradish peroxidase[31] one of the bands decays to a biexponential decay while the other decays as an offset exponential. The biexponential decay indicates that there are two timescales to the spectral diffusion – one faster, likely due to solvent fluctuations, and one slower, caused by a process with a higher energy barrier or inherently slower process, such as protein reorientation.[56] The offset in the other band is also due to one of these slower processes, but this process takes longer than the experimental window available during the vibrational lifetime of the probe, so there is no way for the frequency to sample all available environments before the amplitude of the 2D-IR signal decays to an undetectable level.

Information about a probe's environment can be obtained not just from the form of the FFCF decay, but also how quickly it decays. For example, the spectral diffusion timescale has been used to identify protein crowding,[20] confinement in interfacial water,[21, 55, 57] the effect of drugs on the influenza virus,[58] and the effects of

incorporating an unnatural amino acid into a peptide.[59] Information about the vibrational probe's environment extracted from the FFCF is generally with more accuracy than an early waiting time 2D spectrum. The correlation function will begin with a value lower than 1 due to homogeneous broadening, as a homogeneously broadened system will have already fluctuated some at the earliest detectable time.[30, 31] The inhomogeneity of a peak can be calculated when both the y-intercept of the correlation and the linear infrared linewidth are known.

1.5 Molecular Modeling

To inform a molecular interpretation one rarely can rely on experimental data alone. This dissertation reports extensive computational chemistry results using both classical and quantum mechanical representations of the molecules studied experimentally. Density Functional Theory (DFT) in particular has become a prominent method of calculating frequencies and energies of molecular structures using quantum mechanics. The harmonic frequencies calculated using DFT are typically accurate enough to assist in assigning peaks in a linear or 2D-IR spectrum, though a scaling factor is often needed to obtain frequencies in the same range as those experimentally observed.[60-62] Charges can also be obtained from the DFT calculation, although translating a quantum mechanical property like electron density into a classical charges is not trivial and many different methods exist to try and obtain results that reproduce experimentally reported values.[63-67]

One advantage of these calculations is that they may differ from the experimental conditions to simplify the system or exaggerate effects. For example, when investigating the splitting of the asymmetrical band of a carbonyl probe in a small unilamellar vesicle,[19] rather than modeling the entire probe and the lipids surrounding it, the same general properties could be obtained by modeling only a smaller part of the probe that included the metal carbonyls. A nearby ion can affect one of the degenerate modes more than the other, so a sodium cation was placed nearby and the distance from the probe was varied, qualitatively reproducing the splitting in the calculated

frequencies. This introduction of an unpaired cation to the system may have been possible experimentally, such as by using a bulky anion like tetraphenylborate to ensure the two ions are solvent separated,[68] but keeping the sodium ion near the probe without being shielded by the solvent was an experimental obstacle that was easily overcome in the model system.

DFT produces reliable results for small systems, such as those with several dozen atoms or fewer, but for larger systems the calculation times increase to the point of being unfeasible. This may be circumvented by looking only at the relevant portion of a molecule by making reasonable substitutions, but this is not possible when the greater structure of the system is important, for example in proteins where residues that are far from each other in the amino acid sequence can be in close proximity depending how the protein folds.[69, 70] To account for both the area of interest and the greater protein structure, a mixture of Quantum Mechanics and Molecular Mechanics (QM/MM) can be used to more accurately represent the system. For example, the active site of an enzyme could be modeled with DFT or another quantum mechanical treatment while the rest of the enzyme is modeled with a molecular mechanical force field like AMBER[71-73] or CHARMM.[74, 75] This allows for more accurate study of the enzyme and the reaction pathway by modeling transition states including the different conformations of rest of the protein. For example, the influence of a nearby histidine residue in myoglobin was studied using QM/MM and the dominant factor in the shifting of a bound carbonyl frequency was found to be the tautomerization state of the nearby distal histidine and not deformation of the heme pocket.[76]

One implementation of the QM/MM methodology is Our own N-layered Integrated molecular Orbital and molecular Mechanics (ONIOM)[77, 78] which allows atoms to be placed into layers that are treated with different levels of theory, either QM or MM. One advantage of ONIOM is that it is implemented in the Gaussian 09 software suite[79] that is used for DFT calculations. ONIOM has been previously used to obtain more accurate active site geometries,[80] explored intermediate structures in enzymes,[81]

explore the effects of substituting different metals into an enzyme,[82] and provide insight into the structure of proteins where the crystal structure is unknown.[83]

1.6 Summary of Chapters

In Chapter 2, we investigate a vibrationally labeled *de novo* metalloenzyme using 2D-IR to reveal unexpected nonequilibrium dynamics. The system is modeled using ONIOM to explain the vibrationally driven nonequilibrium dynamics. The advanced model predicts a coupling between two vibrational modes caused by the electrostatic environment of the peptide that was not observed using DFT on a small molecule analogue. The Appendix also contains information about this system and the details of some of the assumptions and further calculations discussed in the main chapter.

Chapter 3 expands on the modeling started in Chapter 2 by developing generating better starting structures for the ONIOM calculations. Force field parameters are also calculated for the active site so more accurate molecular dynamics simulations can be performed. Another peptide that shows better catalytic activity is studied using 2D-IR and the improved modeling method. This new peptide also shows nonequilibrium dynamics and behaves as predicted by the model.

A different system is studied in Chapter 4, where the effect of changing the cation in a series of thiocyanate salts is investigated. The cations chosen are all well studied members of the Hofmeister series, which can either cause the solubility of a protein to increase or decrease through not entirely clear interactions, but likely involving the solvation shell of water. The confinement of the thiocyanate anion in a hydrophobic cavity, α-cyclodextrin, is also investigated, although the amount of information obtained is limited due to noise in the data collected.

An additional system involving thiocyanate is studied in Chapter 5, where the complex between sodium thiocyanate and a crown ether are investigated. The crown ether is labeled with a vibrational probe to reveal dynamical information about not only the thiocyanate, but also the crown ether by combining two types of confinement. In the first, crown ethers and alkali cations form a complex with the cation confined to the

center of the crown ether, withdrawing electron density from the oxygen atoms. The second confinement is the contact ion pair formed by the ions in sodium thiocyanate in THF, where the solvent is unable to separately solvate the two ions meaning almost all of the dissolved NaSCN will exist as a contact ion pair or dimer. 2D-IR spectroscopy is able to provide information about the structure of the system when combined with DFT calculations.

The final chapter, Chapter 6, summarizes the results of the main body chapters and discusses potential future directions for each of the projects.

1.7 References

1. Yu, F.; Cangelosi, V. M.; Zastrow, M. L.; Tegoni, M.; Plegaria, J. S.; Tebo, A. G.; Mocny, C. S.; Ruckthong, L.; Qayyum, H.; Pecoraro, V. L., Protein Design: Toward Functional Metalloenzymes. *Chem. Rev.* **2014,** *114*, 3495-3578.

2. Nagel, Z. D.; Klinman, J. P., Update 1 of: Tunneling and Dynamics in Enzymatic Hydride Transfer. *Chem. Rev.* **2010,** *110*, Pr41-Pr67.

3. Hay, S.; Scrutton, N. S., Good vibrations in enzyme-catalysed reactions. *Nat. Chem.* **2012,** *4*, 161-168.

4. Glowacki, D. R.; Harvey, J. N.; Mulholland, A. J., Taking Ockham's razor to enzyme dynamics and catalysis. *Nat. Chem.* **2012,** *4*, 169-176.

5. Henzler-Wildman, K.; Kern, D., Dynamic personalities of proteins. *Nature* **2007,** *450*, 964-972.

6. Villa, J.; Warshel, A., Energetics and dynamics of enzymatic reactions. *J. Phys. Chem. B* **2001,** *105*, 7887-7907.

7. Hänggi, P.; Talkner, P.; Borkovec, M., Reaction-rate theory: fifty years after Kramers. *Rev. Mod. Phys.* **1990,** *62*, 251-341.

8. Steinbach, P. J.; Ansari, A.; Berendzen, J.; Braunstein, D.; Chu, K.; Cowen, B. R.; Ehrenstein, D.; Frauenfelder, H.; Johnson, J. B.; Lamb, D. C.; Luck, S.; Mourant, J. R.; Nienhaus, G. U.; Ormos, P.; Philipp, R.; Xie, A. H.; Young, R. D., Ligand-Binding to Heme-Proteins - Connection between Dynamics and Function. *Biochemistry* **1991,** *30*, 3988-4001.

9. Hynes, J. T., Chemical-Reaction Dynamics in Solution. *Annu. Rev. Phys. Chem.* **1985,** *36*, 573-597.

10. Tucker, M. J.; Abdo, M.; Courter, J. R.; Chen, J. X.; Brown, S. P.; Smith, A. B.; Hochstrasser, R. M., Nonequilibrium dynamics of helix reorganization observed by transient 2D IR spectroscopy. *Proc. Natl. Acad. Sci. U. S. A.* **2013,** *110*, 17314-17319.

11. Woys, A. M.; Mukherjee, S. S.; Skoff, D. R.; Moran, S. D.; Zanni, M. T., A Strongly Absorbing Class of Non-Natural Labels for Probing Protein Electrostatics and Solvation with FTIR and 2D IR Spectroscopies. *J. Phys. Chem. B* **2013,** *117*, 5009-5018.

12. Huber, C. J.; Egger, S. M.; Spector, I. C.; Juelfs, A. R.; Haynes, C. L.; Massari, A. M., 2D-IR Spectroscopy of Porous Silica Nanoparticles: Measuring the Distance Sensitivity of Spectral Diffusion. *J. Phys. Chem. C* **2015,** *119*, 25135-25144.

13. Rosenfeld, D. E.; Gengeliczki, Z.; Smith, B. J.; Stack, T. D.; Fayer, M. D., Structural dynamics of a catalytic monolayer probed by ultrafast 2D IR vibrational echoes. *Science* **2011,** *334*, 634-9.

14. Hu, W. H.; Webb, L. J., Direct Measurement of the Membrane Dipole Field in Bicelles Using Vibrational Stark Effect Spectroscopy. *J. Phys. Chem. Lett.* **2011,** *2*, 1925-1930.

15. Douhal, A., Ultrafast guest dynamics in cyclodextrin nanocavities. *Chem. Rev.* **2004,** *104*, 1955-1976.

16. Treuffet, J.; Kubarych, K. J.; Lambry, J. C.; Pilet, E.; Masson, J. B.; Martin, J. L.; Vos, M. H.; Joffre, M.; Alexandrou, A., Direct observation of ligand transfer and bond formation in cytochrome c oxidase by using mid-infrared chirped-pulse upconversion. *Proc. Natl. Acad. Sci. U. S. A.* **2007,** *104*, 15705-15710.

17. Bakulin, A. A.; Cringus, D.; Pieniazek, P. A.; Skinner, J. L.; Jansen, T. L. C.; Pshenichnikov, M. S., Dynamics of Water Confined in Reversed Micelles: Multidimensional Vibrational Spectroscopy Study. *J. Phys. Chem. B* **2013,** *117*, 15545-15558.

18. Bian, H. T.; Wen, X. W.; Li, J. B.; Chen, H. L.; Han, S. Z.; Sun, X. Q.; Song, J. A.; Zhuang, W.; Zheng, J. R., Ion clustering in aqueous solutions probed with vibrational energy transfer. *Proc. Natl. Acad. Sci. U. S. A.* **2011,** *108*, 4737-4742.

19. Osborne, D. G.; Dunbar, J. A.; Lapping, J. G.; White, A. M.; Kubarych, K. J., Site-Specific Measurements of Lipid Membrane Interfacial Water Dynamics with Multidimensional Infrared Spectroscopy. *J. Phys. Chem. B* **2013,** *117*, 15407-15414.

20. King, J. T.; Arthur, E. J.; Brooks, C. L.; Kubarych, K. J., Crowding Induced Collective Hydration of Biological Macromolecules over Extended Distances. *J. Am. Chem. Soc.* **2014,** *136*, 188-194.

21. King, J. T.; Arthur, E. J.; Brooks, C. L.; Kubarych, K. J., Site-Specific Hydration Dynamics of Globular Proteins and the Role of Constrained Water in Solvent Exchange with Amphiphilic Cosolvents. *J. Phys. Chem. B* **2012,** *116*, 5604-5611.

22. Fenn, E. E.; Wong, D. B.; Fayer, M. D., Water dynamics in small reverse micelles in two solvents: Two-dimensional infrared vibrational echoes with two-dimensional background subtraction. *J. Chem. Phys.* **2011,** *134*, 054512.

23. Bonn, M.; Bakker, H. J.; Ghosh, A.; Yamamoto, S.; Sovago, M.; Campen, R. K., Structural Inhomogeneity of Interfacial Water at Lipid Monolayers Revealed by Surface-Specific Vibrational Pump-Probe Spectroscopy. *J. Am. Chem. Soc.* **2010,** *132*, 14971-14978.

24. Bredenbeck, J.; Ghosh, A.; Nienhuys, H. K.; Bonn, M., Interface-Specific Ultrafast Two-Dimensional Vibrational Spectroscopy. *Acc. Chem. Res.* **2009,** *42*, 1332-1342.

25. Ghosh, A.; Smits, M.; Sovago, M.; Bredenbeck, J.; Muller, M.; Bonn, M., Ultrafast vibrational dynamics of interfacial water. *Chem. Phys.* **2008,** *350*, 23-30.

26. Loring, R. F.; Mukamel, S., Selectivity in Coherent Transient Raman Measurements of Vibrational Dephasing in Liquids. *J. Chem. Phys.* **1985,** *83*, 2116-2128.

27. Khalil, M.; Demirdoven, N.; Tokmakoff, A., Coherent 2D IR spectroscopy: Molecular structure and dynamics in solution. *J. Phys. Chem. A* **2003,** *107*, 5258-5279.

28. Nee, M. J.; McCanne, R.; Kubarych, K. J.; Joffre, M., Two-dimensional infrared spectroscopy detected by chirped pulse upconversion. *Opt. Lett.* **2007,** *32*, 713-5.

29. Ogilvie, J. P.; Kubarych, K. J., Multidimensional Electronic and Vibrational Spectroscopy: An Ultrafast Probe of Molecular Relaxation and Reaction Dynamics. *Advances in Atomic, Molecular, and Optical Physics, Vol 57* **2009,** *57*, 249-321.

30. Roberts, S.; Loparo, J.; Tokmakoff, A., Characterization of spectral diffusion from two-dimensional line shapes. *J. Chem. Phys.* **2006,** *125*, 084502.

31. Kwak, K.; Park, S.; Finkelstein, I.; Fayer, M., Frequency-frequency correlation functions and apodization in two-dimensional infrared vibrational echo spectroscopy: A new approach. *J. Chem. Phys.* **2007,** *127*, 124503.

32. Cho, M., Coherent two-dimensional optical spectroscopy. *Chem. Rev.* **2008,** *108*, 1331-1418.

33. Baiz, C. R.; Mcrobbie, P. L.; Anna, J. M.; Geva, E.; Kubarych, K. J., Two-Dimensional Infrared Spectroscopy of Metal Carbonyls. *Acc. Chem. Res.* **2009,** *42*, 1395-1404.

34. Messmer, A. T.; Lippert, K. M.; Schreiner, P. R.; Bredenbeck, J., Structure analysis of substrate catalyst complexes in mixtures with ultrafast two-dimensional infrared spectroscopy. *Phys. Chem. Chem. Phys.* **2013,** *15*, 1509-1517.

35. Bian, H. T.; Li, J. B.; Wen, X. W.; Sun, Z. G.; Song, J. A.; Zhuang, W.; Zheng, J. R., Mapping Molecular Conformations with Multiple-Mode Two-Dimensional Infrared Spectroscopy. *J. Phys. Chem. A* **2011,** *115*, 3357-3365.

36. Chen, H. L.; Zhang, Y. F.; Li, J. B.; Liu, H. J.; Jiang, D. E.; Zheng, J. R., Vibrational Cross-Angles in Condensed Molecules: A Structural Tool. *J. Phys. Chem. A* **2013,** *117*, 8407-8415.

37. Kurochkin, D. V.; Naraharisetty, S. R. G.; Rubtsov, I. V., A relaxation-assisted 2D IR spectroscopy method. *Proc. Natl. Acad. Sci. U. S. A.* **2007,** *104*, 14209-14214.

38. Zanni, M.; Hochstrasser, R., Two-dimensional infrared spectroscopy: a promising new method for the time resolution of structures. *Curr. Opin. Struct. Biol.* **2001,** *11*, 516-522.

39. Eaves, J.; Loparo, J.; Fecko, C.; Roberts, S.; Tokmakoff, A.; Geissler, P., Hydrogen bonds in liquid water are broken only fleetingly. *Proc. Natl. Acad. Sci. U. S. A.* **2005,** *102*, 13019-13022.

40. Kwac, K.; Cho, M., Two-color pump-probe spectroscopies of two- and three-level systems: 2-dimensional line shapes and solvation dynamics. *J. Phys. Chem. A* **2003,** *107*, 5903-5912.

41. Hybl, J. D.; Yu, A.; Farrow, D. A.; Jonas, D. M., Polar solvation dynamics in the femtosecond evolution of two-dimensional Fourier transform spectra. *J. Phys. Chem. A* **2002,** *106*, 7651-7654.

42. Bakulin, A. A.; Liang, C.; Jansen, T. L.; Wiersma, D. A.; Bakker, H. J.; Pshenichnikov, M. S., Hydrophobic Solvation: A 2D IR Spectroscopic Inquest. *Acc. Chem. Res.* **2009,** *42*, 1229-1238.

43. Bandaria, J. N.; Dutta, S.; Nydegger, M. W.; Rock, W.; Kohen, A.; Cheatum, C. M., Characterizing the dynamics of functionally relevant complexes of formate dehydrogenase. *Proc. Natl. Acad. Sci. U. S. A.* **2010,** *107*, 17974-17979.

44. Ramasesha, K.; De Marco, L.; Mandal, A.; Tokmakoff, A., Water vibrations have strongly mixed intra- and intermolecular character. *Nat. Chem.* **2013,** *5*, 935-940.

45. Park, S.; Ji, M. B.; Gaffney, K. J., Ligand Exchange Dynamics in Aqueous Solution Studied with 2DIR Spectroscopy. *J. Phys. Chem. B* **2010,** *114*, 6693-6702.

46. Kwak, K.; Rosenfeld, D.; Fayer, M., Taking apart the two-dimensional infrared vibrational echo spectra: More information and elimination of distortions. *J. Chem. Phys.* **2008,** *128*, 204505.

47. Kozinski, M.; Garrett-Roe, S.; Hamm, P., 2D-IR spectroscopy of the sulfhydryl band of cysteines in the hydrophobic core of proteins. *J. Phys. Chem. B* **2008,** *112*, 7645-7650.

48. Osborne, D. G.; Kubarych, K. J., Rapid and accurate measurement of the frequency-frequency correlation function. *J. Phys. Chem. A* **2013,** *117*, 5891-8.

49. Lawrence, C.; Skinner, J., Vibrational spectroscopy of HOD in liquid D2O. III. Spectral diffusion, and hydrogen-bonding and rotational dynamics. *J. Chem. Phys.* **2003,** *118*, 264-272.

50. Ohta, K.; Maekawa, H.; Saito, S.; Tominaga, K., Probing the spectral diffusion of vibrational transitions of OCN- and SCN- in methanol by three-pulse infrared photon echo spectroscopy. *J. Phys. Chem. A* **2003,** *107*, 5643-5649.

51. Piletic, I.; Gaffney, K.; Fayer, M., Structural dynamics of hydrogen bonded methanol oligomers: Vibrational transient hole burning studies of spectral diffusion. *J. Chem. Phys.* **2003,** *119*, 423-434.

52. Tang, J.; Marcus, R., Photoinduced spectral diffusion and diffusion-controlled electron transfer reactions in fluorescence intermittency of quantum dots. *J. Chin. Chem. Soc. (Taipei, Taiwan)* **2006,** *53*, 1-13.

53. Kozinski, M.; Garrett-Roe, S.; Hamm, P., Vibrational spectral diffusion of CN- in water. *Chem. Phys.* **2007,** *341*, 5-10.

54. King, J. T.; Baiz, C. R.; Kubarych, K. J., Solvent-Dependent Spectral Diffusion in a Hydrogen Bonded "Vibrational Aggregate". *J. Phys. Chem. A* **2010,** *114*, 10590-10604.

55. Fenn, E. E.; Wong, D. B.; Giammanco, C. H.; Fayer, M. D., Dynamics of Water at the Interface in Reverse Micelles: Measurements of Spectral Diffusion with Two-Dimensional Infrared Vibrational Echoes. *J. Phys. Chem. B* **2011,** *115*, 11658-11670.

56. King, J. T.; Kubarych, K. J., Site-specific coupling of hydration water and protein flexibility studied in solution with ultrafast 2D-IR spectroscopy. *J. Am. Chem. Soc.* **2012,** *134*, 18705-12.

57. Stirnemann, G.; Castrillon, S. R.-V.; Hynes, J. T.; Rossky, P. J.; Debenedetti, P. G.; Laage, D., Non-monotonic dependence of water reorientation dynamics on surface hydrophilicity: competing effects of the hydration structure and hydrogen-bond strength. *Phys. Chem. Chem. Phys.* **2011,** *13*, 19911-19917.

58. Ghosh, A.; Wang, J.; Moroz, Y. S.; Korendovych, I. V.; Zanni, M.; DeGrado, W. F.; Gai, F.; Hochstrasser, R. M., 2D IR spectroscopy reveals the role of water in the binding of channel-blocking drugs to the influenza M2 channel. *J. Chem. Phys.* **2014,** *140*.

59. Bloem, R.; Koziol, K.; Waldauer, S. A.; Buchli, B.; Walser, R.; Samatanga, B.; Jelesarov, I.; Hamm, P., Ligand Binding Studied by 2D IR Spectroscopy Using the Azidohomoalanine Label. *J. Phys. Chem. B* **2012,** *116*, 13705-13712.

60. Scott, A. P.; Radom, L., Harmonic vibrational frequencies: An evaluation of Hartree-Fock, Moller-Plesset, quadratic configuration interaction, density functional theory, and semiempirical scale factors. *J. Phys. Chem.* **1996,** *100*, 16502-16513.

61. Halls, M. D.; Velkovski, J.; Schlegel, H. B., Harmonic frequency scaling factors for Hartree-Fock, S-VWN, B-LYP, B3-LYP, B3-PW91 and MP2 with the Sadlej pVTZ electric property basis set. *Theor. Chem. Acc.* **2001,** *105*, 413-421.

62. Merrick, J. P.; Moran, D.; Radom, L., An evaluation of harmonic vibrational frequency scale factors. *J. Phys. Chem. A* **2007,** *111*, 11683-11700.

63. Singh, U. C.; Kollman, P. A., An Approach to Computing Electrostatic Charges for Molecules. *J. Comput. Chem.* **1984,** *5*, 129-145.

64. Besler, B. H.; Merz, K. M.; Kollman, P. A., Atomic Charges Derived from Semiempirical Methods. *J. Comput. Chem.* **1990,** *11*, 431-439.

65. Chirlian, L. E.; Francl, M. M., Atomic Charges Derived from Electrostatic Potentials - a Detailed Study. *J. Comput. Chem.* **1987,** *8*, 894-905.

66. Hu, H.; Lu, Z. Y.; Yang, W. T., Fitting molecular electrostatic potentials from quantum mechanical calculations. *J. Chem. Theory Comput.* **2007,** *3*, 1004-1013.

67. Foster, J. P.; Weinhold, F., Natural Hybrid Orbitals. *J. Am. Chem. Soc.* **1980,** *102*, 7211-7218.

68. Lin, J. D.; Popov, A. I., Nuclear Magnetic-Resonance Studies of Some Sodium-Ion Complexes with Crown Ethers and [2]Cryptands in Various Solvents. *J. Am. Chem. Soc.* **1981,** *103*, 3773-3777.

69. Friesner, R. A.; Guallar, V., Ab initio quantum chemical and mixed quantum mechanics/molecular mechanics (QM/MM) methods for studying enzymatic catalysis. *Annu. Rev. Phys. Chem.* **2005,** *56*, 389-427.

70. Senn, H. M.; Thiel, W., QM/MM Methods for Biomolecular Systems. *Angewandte Chemie-International Edition* **2009,** *48*, 1198-1229.

71. Cornell, W. D.; Cieplak, P.; Bayly, C. I.; Gould, I. R.; Merz, K. M.; Ferguson, D. M.; Spellmeyer, D. C.; Fox, T.; Caldwell, J. W.; Kollman, P. A., A Second Generation Force Field for the Simulation of Proteins, Nucleic Acids, and Organic Molecules. *J. Am. Chem. Soc.* **1995,** *117*, 5179-5197.

72. Kollman, P. A., Advances and continuing challenges in achieving realistic and predictive simulations of the properties of organic and biological molecules. *Acc. Chem. Res.* **1996,** *29*, 461-469.

73. Hornak, V.; Abel, R.; Okur, A.; Strockbine, B.; Roitberg, A.; Simmerling, C., Comparison of multiple amber force fields and development of improved protein backbone parameters. *Proteins-Structure Function and Bioinformatics* **2006,** *65*, 712-725.

74. MacKerell, A. D.; Bashford, D.; Bellott, M.; Dunbrack, R. L.; Evanseck, J. D.; Field, M. J.; Fischer, S.; Gao, J.; Guo, H.; Ha, S.; Joseph-McCarthy, D.; Kuchnir, L.; Kuczera, K.; Lau, F. T. K.; Mattos, C.; Michnick, S.; Ngo, T.; Nguyen, D. T.; Prodhom, B.; Reiher, W. E.; Roux, B.; Schlenkrich, M.; Smith, J. C.; Stote, R.; Straub, J.; Watanabe, M.; Wiorkiewicz-Kuczera, J.; Yin, D.; Karplus, M., All-atom empirical potential for molecular modeling and dynamics studies of proteins. *J. Phys. Chem. B* **1998,** *102*, 3586-3616.

75. Best, R. B.; Zhu, X.; Shim, J.; Lopes, P. E. M.; Mittal, J.; Feig, M.; MacKerell, A. D., Optimization of the Additive CHARMM All-Atom Protein Force Field Targeting Improved Sampling of the Backbone phi, psi and Side-Chain chi(1) and chi(2) Dihedral Angles. *J. Chem. Theory Comput.* **2012,** *8*, 3257-3273.

76. Rovira, C.; Schulze, B.; Eichinger, M.; Evanseck, J. D.; Parrinello, M., Influence of the heme pocket conformation on the structure and vibrations of the Fe-CO bond in myoglobin: A QM/MM density functional study. *Biophys. J.* **2001,** *81*, 435-445.

77. Dapprich, S.; Komaromi, I.; Byun, K. S.; Morokuma, K.; Frisch, M. J., A new ONIOM implementation in Gaussian98. Part I. The calculation of energies,

gradients, vibrational frequencies and electric field derivatives. *J. Mol. Struct. Theochem* **1999,** *461*, 1-21.

78. Vreven, T.; Byun, K. S.; Komaromi, I.; Dapprich, S.; Montgomery, J. A.; Morokuma, K.; Frisch, M. J., Combining quantum mechanics methods with molecular mechanics methods in ONIOM. *J. Chem. Theory Comput.* **2006,** *2*, 815-826.

79. Frisch, M. J.; Trucks, G. W.; Schlegel, H. B.; Scuseria, G. E.; Robb, M. A.; Cheeseman, J. R.; Scalmani, G.; Barone, V.; Mennucci, B.; Petersson, G. A.; Nakatsuji, H.; Caricato, M.; Li, X.; Hratchian, H. P.; Izmaylov, A. F.; Bloino, J.; Zheng, G.; Sonnenberg, J. L.; Hada, M.; Ehara, M.; Toyota, K.; Fukuda, R.; Hasegawa, J.; Ishida, M.; Nakajima, T.; Honda, Y.; Kitao, O.; Nakai, H.; Vreven, T.; Montgomery Jr., J. A.; Peralta, J. E.; Ogliaro, F.; Bearpark, M. J.; Heyd, J.; Brothers, E. N.; Kudin, K. N.; Staroverov, V. N.; Kobayashi, R.; Normand, J.; Raghavachari, K.; Rendell, A. P.; Burant, J. C.; Iyengar, S. S.; Tomasi, J.; Cossi, M.; Rega, N.; Millam, N. J.; Klene, M.; Knox, J. E.; Cross, J. B.; Bakken, V.; Adamo, C.; Jaramillo, J.; Gomperts, R.; Stratmann, R. E.; Yazyev, O.; Austin, A. J.; Cammi, R.; Pomelli, C.; Ochterski, J. W.; Martin, R. L.; Morokuma, K.; Zakrzewski, V. G.; Voth, G. A.; Salvador, P.; Dannenberg, J. J.; Dapprich, S.; Daniels, A. D.; Farkas, Ö.; Foresman, J. B.; Ortiz, J. V.; Cioslowski, J.; Fox, D. J. *Gaussian 09, Revision A.02*, Gaussian, Inc.: Wallingford, CT, USA, 2009.

80. Torrent, M.; Vreven, T.; Musaev, D. G.; Morokuma, K.; Farkas, O.; Schlegel, H. B., Effects of the protein environment on the structure and energetics of active sites of metalloenzymes. ONIOM study of methane monooxygenase and ribonucleotide reductase. *J. Am. Chem. Soc.* **2002,** *124*, 192-193.

81. Izquierdo, R.; Rodriguez, L. J.; Anez, R.; Sierraalta, A., Direct catalytic decomposition of NO with Cu-ZSM-5: A DFT-ONIOM study. *Journal of Molecular Catalysis a-Chemical* **2011,** *348*, 55-62.

82. Rajapandian, V.; Hakkim, V.; Subramanian, V., ONIOM Calculation on Azurin: Effect of Metal Ion Substitutions. *J. Phys. Chem. A* **2009,** *113*, 8615-8625.

83. Dalosto, S. D., Computer simulation of the interaction of Cu(I) with Cys residues at the binding site of the yeast metallochaperone Cu(I)-Atx1. *J. Phys. Chem. B* **2007,** *111*, 2932-2940.

Chapter 2

Histidine Orientation Modulates the Structure and Dynamics of a *de novo* Metalloenzyme Active Site

The work in this chapter and the Appendix has been published as the following article:

M. R. Ross, A. M. White, F. Yu, J. T. King, V. L. Pecoraro, K. J. Kubarych *"Histidine Orientation Modulates the Structure and Dynamics of a de Novo Metalloenzyme Active Site*" Journal of the American Chemical Society, 137, 2015, 10164-10176

2.1 Introduction

De novo enzyme design offers opportunities to engineer new catalysts, while furnishing insights into natural biochemical function. There has been remarkable recent progress in designing novel macromolecules with enzymatic functionalities, adopting both "bottom up" and "top down" approaches.[1] Whereas top down strategies modify existing enzymes with well-defined scaffolds to alter their functions, bottom up schemes assemble catalysts that may range from models of natural enzymes to entirely novel macromolecules lacking any similarities to native enzymes. Refining selectivity and efficiency requires either an evolutionary strategy mimicking biology, or a rational chemical approach based on principles of biophysical and bioinorganic chemistry. We seek to advance design optimization from a chemical perspective, bridging the expanse from small-molecule catalysts to biological macromolecules.

By borrowing binding site motifs found in natural enzymes, we have already established that metal ions coordinated within stable peptide matrices are potent catalysts. Using engineered metal binding sites, we have recently shown efficient hydrolytic (Zn) and nitrite reductase (Cu) activity.[2, 3] In these first-generation *de novo*

metalloenzymes, the metal binding sites are established within the stable scaffold of a coiled-coil, homotrimeric peptide. That is, these novel catalysts function despite a lack of any modifications to the active site pocket formed by the hydrophobic side chains that drive the peptide trimer self-assembly, though changes to residues near the active site can modulate efficiency.[4] Hence, it is clear that optimizing the selectivity and efficiency will rest on the ability to modify and control the second coordination sphere by altering the side chains that line the active site within the hydrophobic coiled-coil interior. There is, however, another much less intuitive contribution to the chemistry at the active site, and it is due to the highly directional electrostatic landscape produced by the parallel a-helical protein matrix of TRI family peptide assemblies. Though common elements of structural proteins, parallel coiled-coils are rarely found in natural enzymes, and offer both a challenge and an opportunity for new avenues of *de novo* enzyme optimization. A question arises regarding the degree to which the electrostatic environment can be tailored to specific chemical transformations, for example, by stabilizing transition states to bias the catalytic outcome.[5, 6] Energetic modulations are often seen as paramount to the catalytic speedup performed by enzymes, for example, by lowering a reaction's free energy barrier ($\Delta G^{\ddagger}$). It can be challenging to isolate the role, if any, of the molecular dynamics in governing the rate and selectivity of an ezyme catalyzed transformation. For high barrier, uncatalyzed reactions, dynamical phenomena such as friction and barrier fluctuations influence reaction rates only negligibly. On the other hand, given that catalysts significantly reduce energetic barriers, dynamical aspects, which are neglected by conventional transition state theory, can assume far greater significance.[7-12] It is widely recognized that electrostatics are central to enzyme function,[5] but *in situ* experimental measures of the electric fields and potentials still remain open challenges. Recent progress by Boxer *et al*. has shown how vibrational probes at enzyme active sites can be especially powerful sensors of electric fields that drive catalysis.[13]

The full picture of the reaction dynamics will need to be able to treat the catalysis from the points of view of both dynamical fluctuations and static energetic

considerations. Based on the approach to elucidating the power of enzyme catalysis developed by Warshel, a complete description of catalysis requires an understanding of both the dynamics and energetics of the following processes: 1. the uncatalyzed reaction in water; 2. the enzymatic mechanism in solution (i.e. water); and 3. the catalysis reaction that takes place in the enzyme. In the context of do novo design, for a given net chemical reaction the uncatalyzed path is a constant reference, whereas the enzymatic reaction mechanism in solution may change with mutations to the *de novo* enzyme since they may change the enzyme mechanism. Nevertheless, it is possible to determine the static energetics using experiment or quantum chemistry.[14] Since the reaction free energy barriers for the aqueous protein mechanism paths can be very similar to the uncatalyzed paths in solution,[6] we would anticipate a relatively diminutive role for dynamics in all but the protein catalyzed case, where the barrier is lowered substantially. For this reason, we focus in the current work on studying the structure and dynamics within the protein, but we do anticipate that future studies will need to take into consideration all three of the relevant reaction pathways. *De novo* enzyme design enables us to make minor modifications to the protein catalyzed pathway, while essentially keeping the other two pathways constant, and we feel it is ideally suited to the approach devised by Warshel.

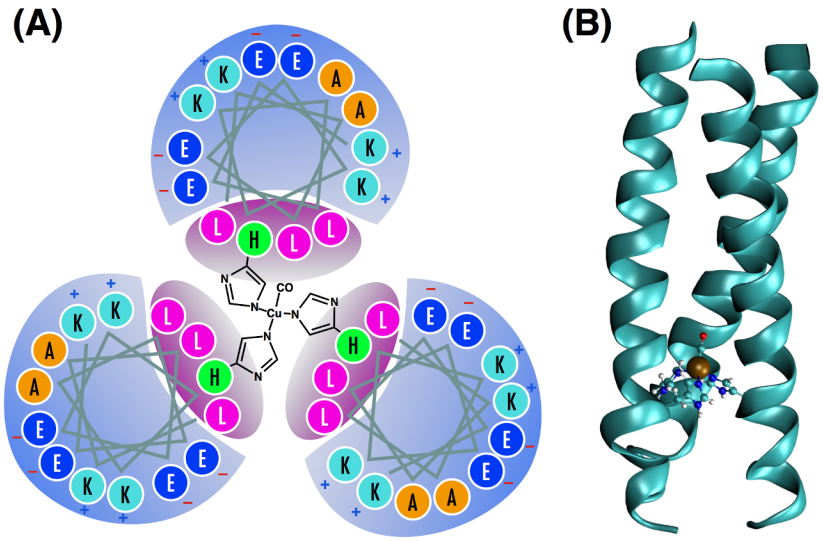

Figure 2.1(*A*) The helix wheel diagram of TRI(L2W)L23H-Cu(I)CO metallopeptide, which is a coiled-coil of three parallel α-helices built from the repeating seven-residue motif LKALEEK. The leucine-rich interior provides a hydrophobic environment in which the type-II copper(I) site is coordinated by three histidine side chains in a distorted tetrahedral geometry. The bound CO ligand serves as a vibrational probe of the active site dynamics. (*B*) QM/MM optimized geometry of the protein showing the coiled-coil tertiary structure, and the distorted tetrahedral metal binding site with coordinated CO.

In metalloenzymes, it has been shown that electrostatics can influence electronic structure and energetics leading to altered redox potentials of metal sites.[15] It remains a significant challenge to predict and design electrostatics, particularly over the large 0.1 to 10 nm range of distances spanned by the TRI peptide scaffolds. Since the protein environment is not static, an experimental probe should also be able to sense active site flexibility, which is directly related to substrate transport into and out of the active site, as well as to the dynamics of a fluctuating reaction barrier resulting from temporal variations of both local structure and more delocalized electrostatics.[16, 17] The transport properties relevant to enzyme catalysis are distinct from those operating in bulk solution due to the significant degree of structural heterogeneity, nanoscale confinement, and macromolecular crowding.[16, 18]

In this paper, we use two-dimensional infrared spectroscopy[19] to study the ultrafast vibrational dynamics of a carbon monoxide ligand bound in the active site of a *de novo* metalloenzyme in which we have previously demonstrated nitrite reductase activity.[4] The CO ligand is bound to a Cu(I) coordinated by three histidine side chains,

and provides an *in situ* probe of the active site (Figure 2.1). Many naturally occurring copper enzymes are capable of binding CO, such as hemocyanins,[20] and the Cu_B site of cytochrome *c* oxidase,[21, 22] and thus provide valuable references against which to compare our vibrational spectroscopy results. As numerous studies of CO-bound heme proteins have shown, the single CO oscillator bound to transition metal atoms can be a particularly sensitive and tractable probe, offering a powerful sensor of structure and dynamics.[23-27]

Here we show for the first time that Cu-CO within a metalloprotein displays an unexpected sensitivity to the electrostatic environment produced by the protein scaffold. For a single oscillator, the 2D-IR spectrum correlates excited and detected vibrational frequencies, resulting in two bands corresponding to the fundamental (v=0 to v=1) and excited state (v=1 to v=2) transitions. The difference in the band center frequencies is the vibrational anharmonicity, and it reflects the curvature of the potential energy surface. With increased time delay between the excitation and detection steps, although the shapes of these bands typically evolve reflecting dynamics sensed by the probe, their frequency centers remain constant. Eventually the signal decays due to vibrational relaxation to the ground state.

In our measurements of the Cu-CO probe ligand, we find that following vibrational excitation, the spectrum of the bound CO ligand undergoes a surprising ultrafast frequency shift on a few picosecond timescale, where the two bands in the 2D-IR spectrum become closer in frequency. This band shifting phenomenon has not previously been observed in 2D-IR spectroscopy, but it appears to be analogous to a fluorescence Stokes shift in electronic spectroscopy, which arises due to non-equilibrium motion of the solvent around the fluorophore. Though we do not expect excitation of a CO vibration to cause the protein to move, it is possible that the CO itself could respond to its vibrational excitation by sampling new conformations, which may in turn lead to non-equilibrium spectral changes.

Determining the origin of these spectral changes requires information about the structure and the electrostatics, which we modeled using hybrid QM/MM calculations

as well as DFT calculations of a small-molecule active site analogue. Our computational results are consistent with the intuitive picture, revealing a slight bending of the Cu-C-O bond angle caused by vibrational excitation, which is modeled by constraining the CO bond to be 10% longer than it is in the optimized geometry. Comparing the small-molecule $(ethylimidizole)_3CuCO$ cluster to the full structure we show that the structural change arises almost entirely due to the protein scaffold's distortion of the geometry of histidine coordination to the copper, which is found to be largely mediated by electrostatics by virtue of the substantial (~4 Debye) dipole moments of the histidine rings. Specifically, we find a dependence of the Cu-C-O bond angle on the C_δ-N_ε-Cu-C dihedral angle. The electrostatic interactions induce structural distortions of the histidines, which in turn activate the coupling between the CO stretch and the Cu-C-O bending motions. This finding suggests that active site energetics can be remotely tuned by modifying electrostatics, providing an avenue for directing mutation strategies, or possibly for engineering long-range allosteric regulation into the *de novo* enzyme.

2.2 Methods

2.2.1 Sample Preparation

Preparation of all solutions was carried out in an inert atmosphere box at room temperature. The apo-peptide solution was prepared by dissolving purified dry peptide powder in a degassed buffer solution in 100% D_2O (50 mM HEPES). 1 eq. (wrt. 3SCC) Cu(I) tetra(acetonitrile) tetrafluoroborate was added to form ~1 mM Cu(I)(**TRI**L2WL23H)$_3^+$ complex. The pH of the solution was then adjusted to 7.5 by adding small aliquots of concentrated KOH in 100% D_2O. Carbon monoxide gas (MetroGas) was purged through the solution for 20 min.

2.2.2 2D-IR Setup

A dual-frequency optical parametric amplifier with independent difference frequency generation stages, pumped by a titanium-sapphire laser amplifier, produce 100-fs mid-IR pulses centered near 2060 cm^{-1}. 2D-IR spectra were recorded for both

rephasing and nonrephasing pulse orderings using our chirped-pulse upconversion method of infrared detection described in previous reports. The coherence time delay between the first two pulses in the photon echo sequence was scanned continuously over a range of roughly 10 ps, resulting in experimental resolution of 3 cm^{-1}. Waiting time delays were fixed at values between -0.25 and 4.5 ps in steps of 0.25 ps, 5 and 20 ps in steps of 0.5 ps, 21 and 30 ps in steps of 1 ps, and 32 and 60 ps in steps of 2 ps. The complex signal field is obtained using spectral interferometry optical heterodyne detection. The local oscillator reference and generated signal fields are detected by sum-frequency generation in a MgO:$LiNbO_3$ crystal pumped with an uncompressed 800 nm pulse from the amplifier system. The resulting visible light centered at 685 nm is detected using a 0.5 m monochromator equipped with a 1200 grooves/mm diffraction grating and a 1300x100 pixel CCD camera synchronized to the 1 kHz laser pulses.

2.2.3 Computational Details

All DFT calculations were performed in Gaussian 09 using the B3LYP functional and 6-311G(d,p) basis set on all atoms with symmetry disabled and tight optimization criteria. For the QM/MM ONIOM calculations, the QM layer (B3LYP/6-311G(d,p)) contains the active site and is almost identical to the smaller cluster calculation described above, consisting of the copper ion, three 5-methylimidazole ligands and a carbonyl ligand. The larger MM layer includes all atoms in the metalloenzyme, with atoms in residues located more than four residues away on either side of the histidine groups frozen to reduce computational cost. The MM layer was treated using the AMBER force field and relaxed prior to performing ONIOM calculations. Electronic embedding was enabled so that the atomic charges from the MM layer would be included in the QM calculations, reproducing the electrostatic interactions as well as the van der Waals interactions that are automatically included. Similarly to the DFT calculation, symmetry was disabled and tight optimization criteria were enabled. The structure was optimized using microiterations with a quadratic coupled algorithm.

2.3 Results and Discussion

2.3.1 Peptide Sequence

TRI-family peptides are designed based on the amphipathic heptad repeat approach. A heptad contains seven amino acid residues *abcdefg*, with hydrophobic residues at the *a* and *d* positions, and hydrophilic, salt-bridging residues *at the e* and *g* positions.[28] The monomer peptides assemble into helical coiled coils upon dissolving in water through hydrophobic collapse.[29-32] Near neutral pH (6-8), it forms parallel three-stranded coiled coils (3SCC).[33, 34] The sequence of the peptide **TRI**L2WL23H is Ac-G WKALEEK LKALEEK LKALEEK **H**KALEEK G-NH_2 with the N-terminus acetylated and C-terminus amidated. The peptide was synthesized on an Applied Biosystem 433A peptide synthesizer using standard protocols[35] and purified and characterized as previously reported.[36] Previous reports demonstrated that derivatives of TRI peptide, **TRI**(L2W)L23H, can bind to Zn(II) and Cu(I)/(II), forming metallopeptides that are excellent structural and functional models for carbonic anhydrase and copper nitrite reductase, respectively.[3, 37] This system is particularly interesting to us because it maintains significant levels of protein complexity in a much-simplified scaffold.

2.3.2 Ultrafast 2D-IR Spectroscopy

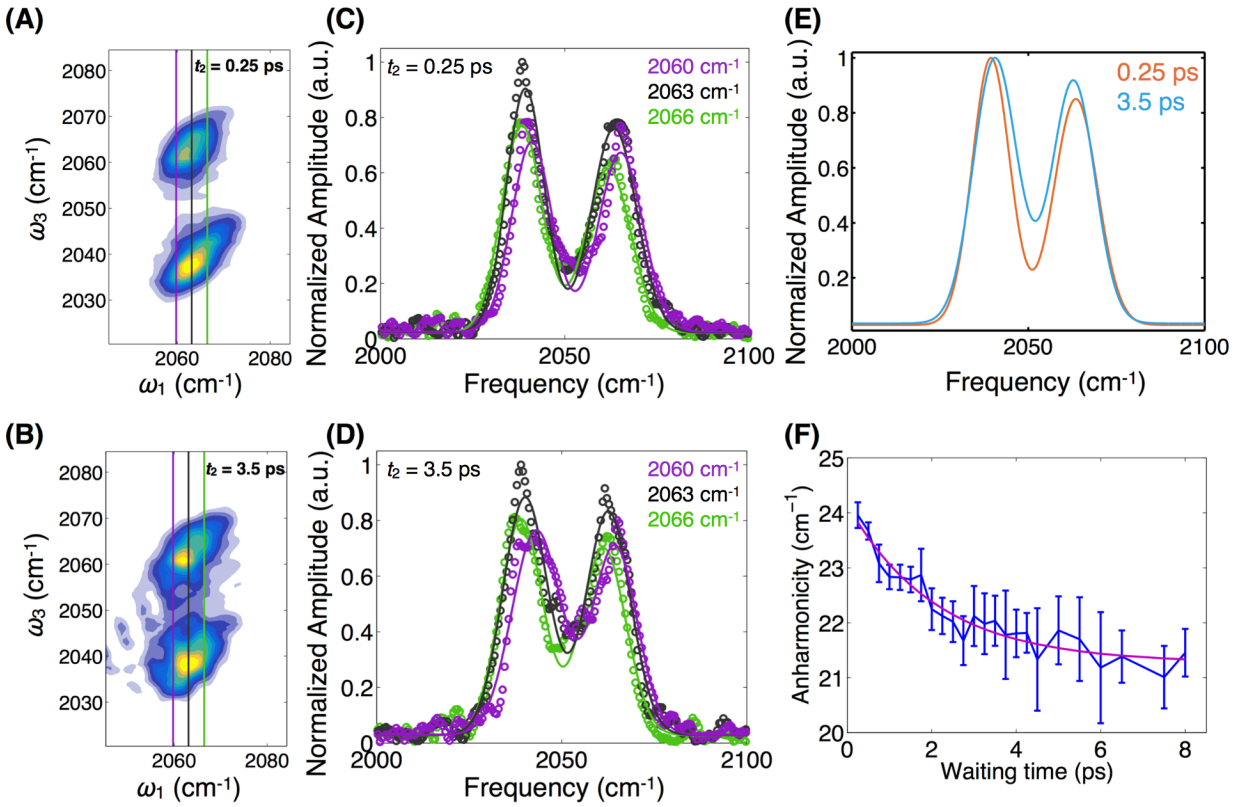

Figure 2.2 Absolute magnitude 2D rephasing spectra recorded at 0.25 ps (*A*) and 3.5 ps (*B*) waiting times. Diagonally elongated band shapes indicate inhomogeneous broadening and the detection frequency (ω_3) difference between the two bands gives the vibrational anharmonicity. Quantitative analysis of the detection frequency-dependent spectra at different values of the excitation frequency (w_1) for t_2 = 0.25 ps (*C*) and 3.5 ps (*D*) show waiting time dependent changes to both amplitudes and centers. Three detection frequency spectra are shown for each waiting time in purple (2060 cm^{-1}), black (2063 cm^{-1}), and green (2066 cm^{-1}), shown in the 2D spectra as vertical lines. (*E*) Fitting the bands for all frequencies between 2060 and 2066 cm^{-1} as described in the text and showing them together highlights the band coalescence. (*F*) The waiting time dependent relaxation of the apparent vibrational anharmonicity is well fit with a decay constant of 2 ps.

2D-IR spectra recorded at a series of waiting time delays (t_2) between the excitation pulse pair and the detection pulse, show an inhomogeneously broadened band centered near 2063 cm^{-1}. The band at lower detection frequency (2039 cm^{-1}) corresponds to excited state absorption from the v=1 to v=2 levels (denoted v_{12}), and is red shifted due to the vibrational anharmonicity of the CO oscillator. The 2063 cm^{-1} fundamental (v=0 to v=1, denoted v_{01}) CO absorption frequency is typical of Cu-CO vibrations observed in other proteins such as the CuB site of cytochrome c oxidase, and

within the bimetallic binding site of hemocyanins.[20, 21] Relative to 1950-1960 cm^{-1} Fe-CO vibrations in heme proteins, the ~100 cm^{-1} blue shifted transition indicates that the copper-carbon bond is weaker, and the degree of p back bonding is also reduced. We note that under the low <1 mM protein concentration we used, it was difficult to record even linear FT-IR spectra, making the measurement of absorptive 2D spectra impossible given our 2D spectrometer's sensitivity. Although the data shown in Figure 2.2 are absolute value rephasing spectra, from which accurate line shape information is not readily extracted, it is nevertheless clear that the anti-diagonal spectral widths are very narrow. We attribute the preponderance of inhomogeneous broadening to the unique environment experienced by the CO vibrational probe. The CO resides in the hydrophobic core of the homotrimeric coiled-coil lined by nonpolar leucine side chains. Numerous previous studies by us and others have shown that metal carbonyl complexes in alkane solvents are generally homogeneously broadened due to the lack of spectral fluctuations induced by the motion of solvating nonpolar liquid molecules.[38] Although the CO is effectively solvated by a nonpolar shell of alkane side chains, it is nevertheless embedded within a complex protein scaffold, which has charged residues on the solvent-exposed exterior, as well as highly oriented CO···NH bonds of the largely a helical peptide chains. In addition, as we detail below, the histidine side chains coordinating the Cu are significantly polar, having average dipole moments of 3.6 D.[39] The low polarity of the interior does not attenuate the electrostatic influence of the charges due to the low effective dielectric constant.[40] The substantial inhomogeneous broadening thus reflects the distribution of peptide conformations, including the coiled-coil packing, which induce shifts in the CO vibrational frequency.

2.3.3 Dynamic Evolution of the 2D-IR Bands

Waiting-time dependent changes in the 2D line shape are routinely monitored using peak shape analysis of absorptive spectra, or by using the inhomogeneity index.[41-43] The diagonal elongation of the line shape reflects the frequency correlation within the inhomogeneously broadened spectral band, and as stochastic modulations cause equilibrium fluctuations of the excited vibrations, the correlation becomes lost as a

function of the waiting time. This stochastic frequency sampling is called spectral diffusion, and is a powerful observable in 2D-IR spectroscopy. The decay of the correlation is related to the frequency fluctuation correlation function, $\langle \delta\omega(0)\delta\omega(t) \rangle$, where the instantaneous frequency $\omega(t) = \langle \omega \rangle + \delta\omega$.[44] The meaning of this correlation function is somewhat poorly defined when the system is evolving out of equilibrium, as is the case for the vibrationally excited CO bound to the Cu active site.

On the few-ps time scale (Figure 2.2), increasing the waiting time in the 2D-IR pulse sequence does not lead to significant spectral reshaping besides that due to scattering from our weakly absorbing sample. The survival of spectral correlation on this timescale (<5 ps) indicates that much of the spectral diffusion takes place on slower timescales, as is expected in complex macromolecular environments.[45, 46] We do note, however, a subtle but significant change in the 2D spectra that, to our knowledge, has not been described previously. The shift in wavenumber between the two bands in the 2D-IR spectrum gives the difference in energy between the 0-1 and 1-2 vibrational transitions, which is a measure of the vibrational anharmonicity. The value obtained at 250 fs waiting time is 24 cm^{-1}, which is typical of a single CO bound to a metal.[47] With increased waiting time, we observe a surprising *decrease* in the frequency separation between the two detected bands.

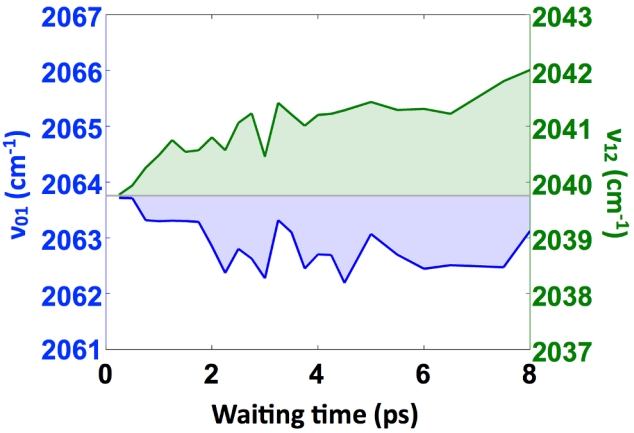

Figure 2.3 Waiting time dependent fitted band centers for the 0-1 (blue) and 1-2 (green) transitions show that the apparent time dependent anharmonicity arises due to the simultaneous red shifting of the 0-1 band and blue shifting of the 1-2 band. Within the simple Morse oscillator model, this trend requires that the dissociation energy D_e increases, while the Morse width parameter a decreases (defined in the Appendix). Both parameters influence the harmonic force constant since $k_{harm} = 2a^2D_e$.

The apparently time-evolving "anharmonicity" is more evident in a quantitative analysis of the bands. Taking slices along the detection frequency axis at each value of the excitation frequency between 2060 and 2066 cm^{-1}, we fit the two bands using Gaussian functions (Figure 2.2). We then average the differences of the fitted center frequencies over all of the excitation frequencies. Plotting the waiting time dependent decay of the averaged differences reveals a clear dynamical signature. The decay of the apparent anharmonicity, due to the spectral evolution of the bands, is well fit to an exponential function with a 2.1 ± 0.8 ps decay constant, plus a constant offset determined by the long-time anharmonicity of 21 cm^{-1}. In addition to plotting the frequency differences between the fitted peak centers, we also show the centers themselves in Figure 2.3. The fitted centers show that the 0-1 transition red shifts, while the 1-2 transition blue shifts. It is interesting to note that the magnitude of the red shift of the 0-1 band is less than the blue shift of the 1-2 band. This difference may be due to the fact that roughly half of the amplitude of the 0-1 band arises from the ground state evolution pathway, where we do not expect any frequency shift.

This observation of an apparent time-dependent anharmonicity is the central experimental finding of this work, and provides the motivation for the subsequent

computational efforts to identify the origin of this dynamical phenomenon. We note that we have observed nearly identical behavior in a different peptide sequence (shown in the SI) in which the positively charged lysine residues on the exterior of the peptide have been mutated to glutamine, indicating that this result is reproducible and is likely a general feature of the coiled-coil protein family we have investigated. Future studies will examine several other peptide sequences which have been shown to exhibit varying degrees of nitrite reductase activity. Importantly, we do not observe this dynamical anharmonicity in a small-molecule iron-monocarbonyl complex we have studied in earlier work (shown in the Appendix); this observation provides a hint that the dynamical evolution is due to the protein environment. Ideally we would compare the same active site structure experimentally in solution as well as embedded within the protein scaffold, but doing so would require synthesizing a complex such as $(ethylimidizole)_3CuCO$. There are monocarbonyl complexes of Cu that could provide useful comparison systems, but which lack the imidazole rings,[48] which we have found to be essential in modulating the Cu-C-O potential energy surface.

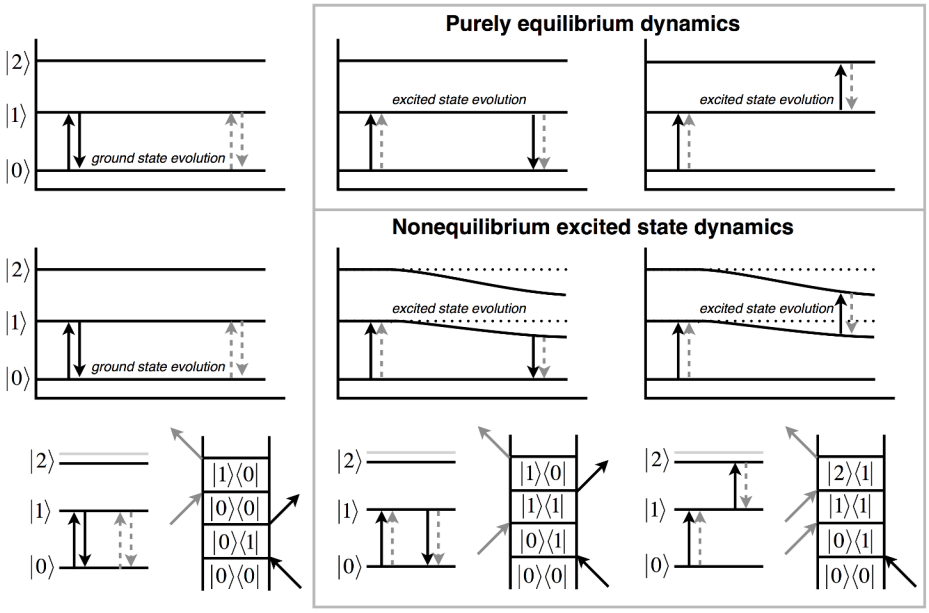

Figure 2.4 Energy level diagrams and rephasing Liouville space diagrams for the three accessible vibrational states of the copper-bound CO ligand show that two of the three pathways involve population evolution on the v=1 vibrational excited state, whereas only one involves ground state evolution. The three contributions to the 2D spectrum are shown in the columns: (*left*) ground state bleach, GSB; (*middle*) stimulated emission, SE; and (*right*) excited state absorption, ESA. The top row illustrates the conventional picture where vibrational excitation is fully uncoupled to the sensed ultrafast dynamics. The middle row shows a time-evolving CO vibrational energy level structure due to continuous modulation by anharmonic coupling to a slow degree of freedom. The bottom row shows the wave-matching energy level diagrams and double-sided Feynman diagrams corresponding to the GSB, SE, and ESA signal contributions.

2D-IR spectroscopy is often analyzed from the point of view where the spectral fluctuations that lead to decay of the correlation of frequency fluctuations are not influenced by the measurement process. For example, the slope of the 2D peak shape's asymmetry is often taken to report the frequency correlation present at a given waiting time, and as the oscillators stochastically sample their full conformational space, including the solvent or other nearby environment, the frequency performs a random walk through the inhomogeneously broadened band.[42, 49, 50] The decay of frequency correlation is generally linked to molecular motions of the probe and of its surroundings. Since nearly all published examples analyze the diagonal 0-1 transition, it is tacitly assumed that the two pathways producing signal on the diagonal report the same equilibrium molecular dynamics. As shown in Figure 2.4, however, the two pathways are clearly distinct, since the ground state bleach pathway corresponds to waiting-time

evolution on the ground state, whereas the stimulated emission pathway corresponds to evolution on the excited vibrational state. If vibrational excitation launches nonequilibrium motion, the diagonal peak will not reflect solely the equilibrium frequency fluctuation correlation function often associated with spectral diffusion. Studies of methanol[51] and of acetic acid[52] have shown that vibrational population relaxation can produce "photoproducts" such as broken hydrogen bonds, as well as hot intermediates. We argue that our observation here of a continuously evolving spectral shift reflects nonequilibrium dynamics not due to cascaded population flow since the motion in the low-frequency coordinate is promptly launched by the $v = 0$ to $v = 1$ CO excitation, and the vibrational relaxation is quite slow (>30 ps, shown in the Appendix). Alternatively, this phenomenon is analogous to nonequilibrium dynamics commonly observed in fluorescent dyes, where solvation induces dynamically shifting Stokes emission.[53-56] Though the solvation coordinate is often treated only qualitatively, in the present case of nonequilibrium vibrational dynamics, it should be possible to identify a candidate for the coordinate along which motion is driven. Indeed the analogy with polar solvation is particularly apt, as discussed below, since our quantum chemistry calculations show a significant increase in CO bond dipole associated with vibrational excitation, which then senses the collective electrostatic environment (see Table A2 in the Appendix). The central question of the remainder of this chapter, therefore, is to determine the molecular origin of the otherwise hidden motional coordinate, as well as the degree to which the motion is driven by local, bonded interactions or by more collective electrostatic influences.

Figure 2.2E shows that the two bands become closer to each other as a function of time, which requires the following interpretation regarding the shifts of the vibrational levels. For the ground state bleach band ($v = 0$ to $v = 1$), the contribution due to the ground-state pathway is unshifted and only exhibits equilibrium spectral diffusion. The stimulated emission contribution evolving on the excited state, however, must red shift to cause the observed spectral change, whereas the excited state absorption ($v = 1$ to $v = 2$) must blue shift. Therefore, one straightforward, though unusual, conclusion is

that the CO vibration becomes more harmonic once it is excited. Within the Morse oscillator model, which describes single and multiple metal carbonyl complexes very well,[57] a red shifted fundamental and reduced anharmonicity means that the bond dissociation energy D_e must increase. Although it is counterintuitive to associate a red shifted frequency with a stronger bond, that intuition is based on a one-dimensional harmonic oscillator picture where the bond strength is encoded in the force constant k; the simple harmonic model is necessarily not able to account for the anharmonicity of real bonding potential energy functions. We discuss this point further below in the context of our computational results.

2.3.4 Quantum Chemical Model of the Copper Site

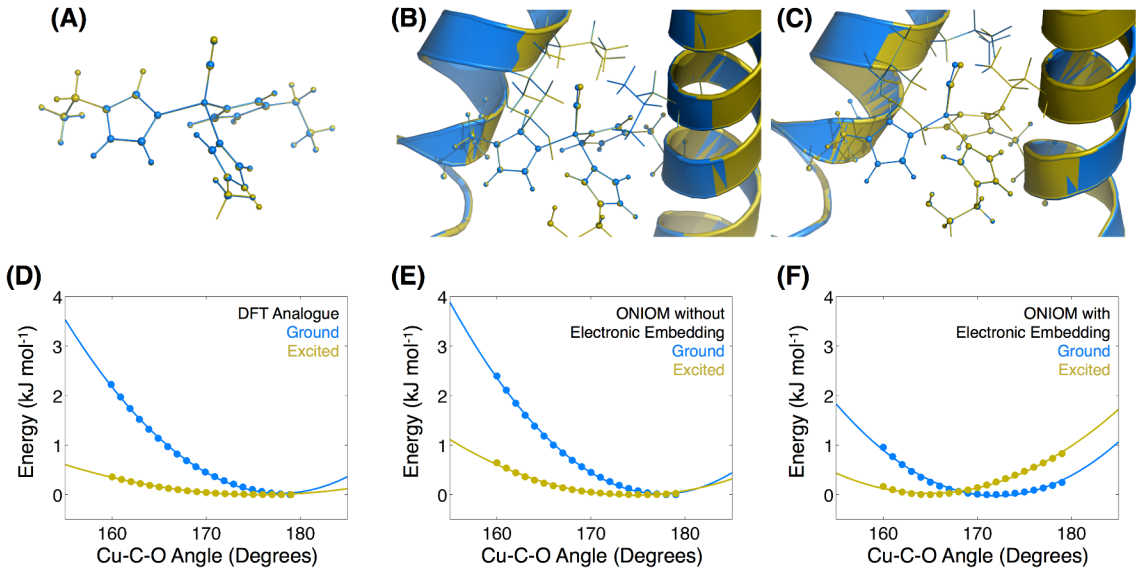

Figure 2.5 The optimized structures of the ground (blue) and vibrationally excited (yellow) states for the small molecule analogue (*A*), peptide calculated with ONIOM without electronic embedding (*B*), and peptide modeled with ONIOM including electronic embedding (*C*). The Cu-C-O bond angle tilting potential is shown for the three cases (*D-F*), with a clear difference between the ONIOM with EE potential and the other two. Calculated energies are shown as points with quadratic fits shown as curves.

To assess the likelihood that the nonequilibrium relaxation is due to the local bonding environment of the copper site, we first considered a small molecule analogue consisting of the copper ion with three 5-ethylimidazole ligands and a carbonyl ligand. In general, we are using the computational study to determine what degrees of freedom

are coupled to the CO stretching mode. We investigate the small molecule analogue for two main reasons. Firstly, the small molecule calculation enables a direct comparison to the case with the protein scaffold, which allows us to determine what role the protein plays in modulating the vibrational coupling. Secondly, the small molecule can be subsequently manipulated in order to understand why the protein is able to modulate the Cu-CO potential energy surface. The starting structure was based on the crystal structure of a similar peptide, $Hg(II)_S[Zn(II)_N(H_2O)](\mathbf{CS}L9CL23H)_3^+$ (PDB ID code 3PBJ), and the geometry of the small molecule was optimized in Gaussian 09 using the B3LYP functional and the 6-311G(d,p) basis set for all atoms as further described in the methods section.[58] To simulate the structural change associated with vibrational excitation, the C-O bond length was fixed at 110% of the globally optimized bond length while the remaining atoms were allowed to reoptimize. This increase in bond length is the expected change for a Morse oscillator with a first excitation frequency of 2063 cm^{-1}, an anharmonicity of 24 cm^{-1}, and the same reduced mass as CO (see Appendix for details of the Morse potential). The calculated vibrationally excited geometry was very similar to the ground state (Figure 2.5A) with a RMSD of 0.023 Å for the atoms excluding the carbonyl. A more detailed discussion of the geometry change upon vibrational excitation can be found in the Appendix. The coordinate we expect to show the largest change from coupling to the CO displacement is the Cu-C-O bond angle, which changes by less than one degree upon vibrational excitation. To compute the expected thermal angle distribution we froze the CO bond length at the ground or excited state value, and then scanned through a range of angles between 160° and 180° while relaxing the other degrees of freedom. The results of this relaxed potential energy surface scan are shown in Figure 2.5D, where the only clear difference is the curvature of the potentials, which is 4.4 times greater in the ground state than the excited state, indicating a difference in the stiffness of the Cu-C-O angle potential.

2.3.5 QM/MM Model of the Full *de novo* Enzyme

Since we were unable to identify an obvious candidate for the hidden motional coordinate by considering only the local bonding environment, we performed hybrid

QM/MM calculations to account for the steric and electrostatic interactions arising from the entire peptide trimer. The QM/MM calculations were carried out with the ONIOM method (our own n-layered integrated molecular orbital and molecular mechanics) as implemented in Gaussian 09 using two layers (described in *Methods*) [59-61]. With ONIOM the vibrational ground and excited state geometries can be compared in a similar way as was done for the small molecule analogue: optimizing the geometry for the ground state and then freezing the extended CO bond while optimizing the rest of the geometry for the vibrational excited state. In the ONIOM model, the optimized Cu-C-O bond angle is found to decrease by more than 6° upon vibrational excitation, as shown in Figure 2.5C. The relaxed potential energy surface scan is also included in Figure 2.5F and shows a clear difference between the ground and excited state Cu-C-O angle potential energy surfaces, although the change in curvature is less pronounced than for the small molecule analogue. In the peptide with electronic embedding, the curvature in the ground state is greater by a factor of 1.5 relative to the excited state, which is a considerably smaller difference than in the small molecule analogue. These calculations support the attribution of the hidden motional coordinate to the Cu-C-O bond angle, and that the presence of the peptide enhances the coupling to the CO stretch. The identification of the bend as the coupled degree of freedom is consistent with the 1-2 ps time scale of the vibrational frequency shifting dynamics. Our frequency analyses yield normal modes that most closely resemble the bending motion to have frequencies of 27.37 cm^{-1} (small molecule) and 31.30 cm^{-1} (ONIOM with embedding). Both of these frequencies correspond to vibrational periods of about 1 ps, which is consistent with our measured timescale.

In order to separate the contributions due to electrostatic and other nonbonding interactions, we repeated the ONIOM calculations with electronic embedding disabled so that the electrostatic contribution from atoms not included in the QM layer would be ignored. Comparing the results obtained in the presence and absence of the MM charges enables us to isolate the electrostatic interactions from the excluded-volume, or hard-sphere collisions, for example, between the vibrationally excited carbonyl and the

leucine residues above the active site in the interior of the peptide. The resulting potentials, shown in Figure 2.5E, are much more similar to those of the small molecule analog than the ONIOM calculations including electronic embedding. Both the ground and vibrationally excited states have Cu-C-O bond angles closer to 180° and the difference between the two is less than 3°. The curvature of the ground state potential is 2.6 times that of the excited state in this case, again showing that the ONIOM model without electronic embedding again falls between the values found for the other calculations. This comparison shows that the coupling of the Cu-C-O bond angle to the CO stretching frequency is more strongly influenced by the electrostatic interactions than by the van der Waals interactions.

Though there have been no previous reports of copper carbonyl proteins or small molecules studied with 2D-IR, there have been several experimental and theoretical investigations of heme proteins, which leverage the Fe-CO vibrational probe to study the dynamics of the heme site.[47, 62-69] Though the present study does not rely upon computations to model the dynamics or 2D-IR spectra for comparison to experiment, several previous reports of heme proteins have taken this approach, and we summarize their basic characteristics here. A very successful strategy used to simulate 2D-IR spectra and associated dynamical observables employs classical molecular dynamics simulations coupled with an electrostatic-based mapping procedure for generating instantaneous vibrational frequencies at each simulation step.[70-75] In the case of myoglobin, which has received significant attention, two varieties of mapping approaches have been implemented, and represent the range of complexity used in other 2D-IR simulation studies. To model three-pulse vibrational photon echo spectroscopy, which can be considered to be a subset of 2D-IR spectroscopy, Fayer and Loring's groups used MD simulations of carboxymyoglobin, producing CO frequencies by using the experimental Stark tuning rate determined by Boxer *et al*.[47] They used the frequency trajectories to construct the third-order response function and found good agreement with experiment.

An alternative approach was taken by Cho *et al.*, using a much more sophisticated frequency mapping procedure based on a multi-site evaluation of the electrostatic potential.[68] This multi-site approach enables the detailed treatment of directional hydrogen bonding, which is particularly important in capturing the subtle interactions between the histidine side chain and the CO ligand.

Recent theoretical and experimental investigations of heme proteins by Falvo *et al.* used an explicit quantum mechanical treatment of the CO vibrational frequency and transition dipole moment.[67] In that approach, the CO vibrational potential is parameterized in such a way that electrostatics and anharmonic couplings are included, yielding a time-dependent CO potential energy surface.[76] Solving the 1D Schrödinger equation for that surface provides the vibrational frequencies, anharmonicities and transition moments needed to compute linear and nonlinear response functions. Even this method, however, does not explicitly propagate the CO in an excited state to calculate the excited state absorption and the stimulated emission pathways. Hence, the method essentially makes the assumption that vibrational excitation does not alter the spectral dynamics. Given the excellent agreement between experiment and simulation, it appears that the ground state assumption is valid for hemoglobin. It is noteworthy that these investigators did include an explicit anharmonic coupling between the CO stretch and the Fe-C-O bend coordinates to reflect the red shift that occurs as the Fe-C-O bond angle is distorted from linear. Thus, the model treats the case where the protein environment's distortion of the bond angle alters the CO stretch potential surface. This coupling necessarily works both ways, however, so that it is possible that exciting the CO also causes a bending motion. Evidently the effect is too weak to be seen in the experimental data, so neglecting the explicit CO stretch excitation seems to be a valid simplification.

In summary, these approaches to simulating 2D-IR spectra of heme proteins do not explicitly include the effect of vibrational excitation for the two paths that evolve in excited states since it is hypothesized that the dynamics of the surroundings will not be

altered. This hypothesis seems quite reasonable in the case of myoglobin and hemoglobin since the major dynamical contribution is from the histidine motion.

There are cases where vibrational excitation does induce dynamics. For example, in methanol, exciting the OH (or OD) stretch can break the OH···O hydrogen bond, causing the dangling OH bond to blue shift.[51, 77-80] This process has been denoted a vibrational photochemical reaction, and leads to new cross peaks in the 2D-IR spectrum, which have been reproduced by theoretical modeling.[81, 82] There are also examples of coupled, hydrogen bonded dimers, such as those of acetic acid and of 7-azaindole.[83-88] In these cases, there are clear observations of vibrational quantum beats launched by excitation of the OH stretches that are anharmonically coupled to low-frequency inter-dimer motions. It is these types of couplings that are perhaps the most similar to our present studies of the *de novo* metalloenzyme, though in our case we find the anharmonic coupling to be highly dependent on the details of the coordination geometry at the metal site.

2.3.6 Electrostatic Potential is Indirectly Responsible for the Vibrational Coupling

The computational results suggest that the electrostatic environment of the peptide enhances the coupling of the carbonyl stretching mode to the Cu-C-O angle. The Adaptive Poisson-Boltzmann Solver (APBS) software[89] was used to calculate the electrostatic potential, and from that the electric field projected along a vector defined by the carbonyl bond as described in the Appendix. The electric field magnitude along the carbonyl bond was found to vary greatly for two different conformers of the peptide, both optimized from different starting structures using the ONIOM scheme described above. The fields of the two conformers differ by about 35 MV/cm, principally in the contribution from the histidine residues, where a fairly small geometrical change (RMSD of $(His)_3CuCO$ is 0.75 Å) results in a RMS Mulliken charge difference of 0.04 *e* for the same atoms. Despite the large field difference, the carbonyl tilts upon vibrational excitation in both conformers and the electric field magnitude changes along the carbonyl in the ground and excited states are similar. So rather than the electric field

directly affecting the carbonyl, it appears that the electric field from the peptide scaffold distorts the coordination of the histidines to the copper atom, which is responsible for inducing the coupling between the CO stretch and the Cu-C-O bend coordinates.

To test the role of the three histidines in modulating the CuCO potential surface and to simulate a distortion of the histidines caused by the electric field, we performed DFT calculations on the small molecule analogue holding the C-N-Cu-C dihedral angles of each histidine fixed at values slightly larger than those of the optimal geometry. Without an applied field, we find that the Cu-C-O angle becomes tilted in the vibrational excited state, confirming the subtle coupling between the histidine coordination, the CO stretch and the Cu-C-O bend. Though the electric field will still likely cause a frequency shift and some of the CO tilting, the nonequilibrium dynamical signatures we observe appear to arise primarily from the bonding environment of the $(His)_3Cu$ coordination. In other words, the histidines transduce their electrostatic interactions with the peptide scaffold to the copper active site *via* their coordination, which in turn alters the energetics of exogenous ligand binding, CO in this case. We note here that the link between histidine coordination geometry and the coupling between the CO stretch and Cu-C-O bend can be completely determined using the DFT calculations. Hence, we can regard the QM/MM calculations as providing a guide for the small molecule DFT calculation. That our structural finding is essentially independent of the QM/MM results is reassuring since there are more sophisticated QM/MM methods than ONIOM.

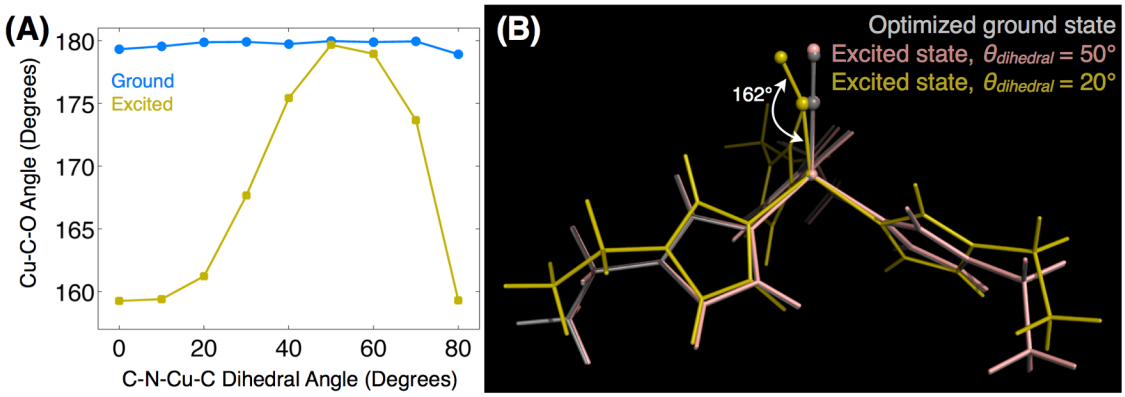

Figure 2.6 The propensity for excited state structural changes appears to be controlled by the geometry of the histidine's coordination with copper. Results of DFT calculations of the small $Cu(EtIm)_3CO$ cluster in the absence of the protein matrix show that (*A*) the optimized Cu-C-O bond angle is insensitive to the C_δ-N_ε-Cu-C dihedral angle in the CO vibrational ground state. In the excited state, however, the bond angle and tilt become acutely sensitive to the histidine coordination geometry. (*B*) Structures selected from the full dihedral angle scan with dihedral angles of 20° and 50° illustrate the link between the histidine coordination and the copper-ligand bonding. This geometrical distortion only occurs in the CO excited state, suggesting the inadequacy of ground-state equilibrium structures to reveal reactivity. Similar structures showing no substantial changes on the ground state are shown in the Appendix.

To investigate the histidine dihedral angle dependence further, we varied the C_δ-N_ε-Cu-C dihedral angles for each imidazole in the $Cu(EtIm)_3CO$ cluster systematically, optimizing the other atoms at each angle. Figure 2.6 shows the optimized CuCO angle as a function of the histidine coordination geometry computed for both the CO vibrational ground state as well as the simulated CO $v = 1$ state. Whereas there is essentially no dependence on the histidine geometry in the vibrational ground state, the excited state geometry is highly sensitive to the histidine coordination. These findings show that the CO excited state, more than the ground state, is remarkably sensitive to molecular and electronic structure changes in the first coordination sphere, which are themselves highly influenced by the overall electrostatics of the macromolecular construct. In general, the importance of histidine coordination and the structural changes upon ligand binding or dissociation are well known.[90]

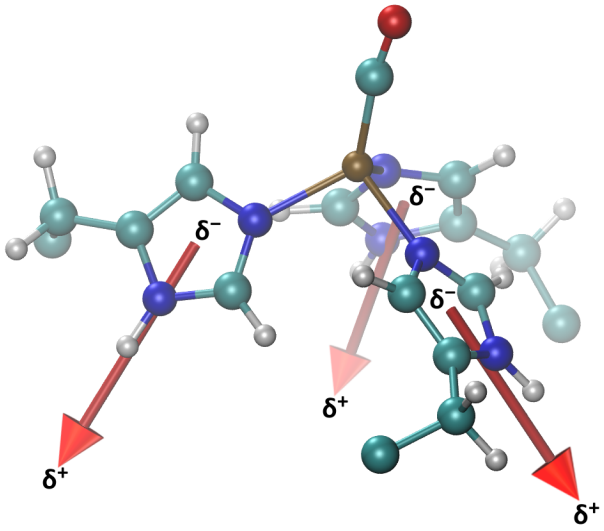

Figure 2.7 Dipole moment of each histidine ring, in Cu(I)(TRIL2WL23H)$_3$(CO)$^+$ with average magnitude of 3.6 D. These dipolar side chains are able to couple to the electrostatic environment produced by the protein scaffold.

It remains to be determined *why* the histidines are so susceptible to structural modification by electrostatics. By considering in detail the partial charges on the histidine CH and NH bonds, we find that, averaged over the three histidines, the N_δ-H and C_δ-H bonds are substantially more polar than the C_ε-H bonds, leading to a net dipole moment of roughly 3.6 D for each histidine side chain (Figure 2.7, see details in the Appendix). This computational result agrees very well with the value determined from microwave spectroscopy of imidazole.[39] The electric field presented by the protein applies a torque on the histidines through the charge asymmetry, which is enhanced relative to the uncoordinated histidines due to the metal coordination. This polarization has been observed in other copper binding sites, such as in cytochrome *c* oxidase's Cu_B site.[91] It is interesting to note that in cytochrome c oxidase, it is the epsilon carbons that point toward the ligand binding site, rather than the present case of the delta carbons. In our QM/MM results, the C_δ-H bonds are more polarized than are the C_ε-H bonds in cytochrome *c* oxidase. The metal-induced polarization of CH bonds in histidines has been identified as a source of structure stabilizing CH···O hydrogen bonds in a series of metalloenzymes.[92] Indeed, CH···O hydrogen bonding to mutated side chains or

substrates in the active site of our *de novo* metalloenzyme may also be leveraged to optimize catalytic efficiency and selectivity.[93]

2.3.7 Relationship Between Bond Angle and CO Frequency

The identification of the Cu-C-O angle as the hidden coordinate coupled to carbonyl vibrational excitation does not necessarily explain why the CO frequencies appear to evolve dynamically. To compute the nonequilibrium vibrational transition energy would require a quantum dynamical treatment of a much higher dimensional potential energy surface. Nevertheless, there is ample evidence from previous studies of metal-CO bonding in heme proteins to help draw the link between bond angle and CO frequency. In contrast to smaller coordination complexes, where nonbridged metal-CO bonds rarely deviate from linear geometries,[94] influences from the protein do indeed induce distortions in ligand binding. One particularly well-known example is the heme protein myoglobin, where X-ray crystallography models showed significantly bent Fe-C-O bond angles, apparently in conflict with energetic constraints imposed by such highly distorted structures.[24, 25, 27, 95, 96] The discrepancies were ultimately resolved by improvements in crystallography, and by considering the results of picosecond infrared transient anisotropy measurements, which indicated much more linear bond angles, even after careful consideration of finite sample thickness effects as well as accounting for the precise orientation of the CO transition dipole moment.[97] The infrared studies of myoglobin and hemoglobin, where the primary focus was on the geometry of the Fe-C-O and its orientation relative to the heme plane, are particularly helpful in understanding the dynamic frequency shifts we observe in the Cu-CO embedded within the peptide coiled-coil. Taking the values obtained in the heme proteins for CO wavenumber as a function of Fe-C-O bond angle determined from crystallography and IR spectroscopy, we can estimate a shift of roughly 5 cm^{-1} for a 6° change in the angle assuming a linear regression of the angle-dependent vibrational frequency (details in the Appendix). While this frequency shift is larger than the 3-4 cm^{-1} shift we observe in the CuCO case, in heme proteins the Fe-C bond is shorter, as evidenced by the considerably lower Fe-CO transition energy (1930-1950 cm^{-1} in heme proteins in

contrast to the 2063 cm^{-1} in the CuCO peptide). Hence, for Cu-CO one would expect a reduced coupling between bond angle and CO bond strength. It is noteworthy that in the heme case, much of the distortion energy (~85%) can be attributed to the strong polar contact through hydrogen bonding to the nearby histidine residue,[96] whereas in the present CuCO case, the distortion from the linear form arises nearly entirely from variation in the histidine orientation, which itself reflects the longer range electrostatic interactions with the protein scaffold. Future work to understand the CO frequency dynamics will be undertaken following the approach of Falvo and Meier,[67, 76] using a multidimensional potential surface combined with quantum dynamics to evaluate the non-equilibrium transition frequencies.[98]

2.3.8 Rationale for Nonequilibrium Decreases in Fundamental Frequency and in the Vibrational Anharmonicity

The vibrational states of CO bound to transition metals are typically well described using Morse oscillators, even in the case of multiple coupled CO ligands.[57] The Morse potential is characterized by two parameters D_e, the dissociation energy (from the potential minimum), and a term, a, that controls the stiffness.[99] Although the Morse potential can only be viewed as an approximate model of the CO bond, it is helpful in providing a chemical interpretation of the vibrational spectra. In the present case, we find that the nonequilibrium motion leads to both a red-shift of the carbonyl n_{01} (where n_{01} is the frequency difference between the v=0 and v=1 vibrational states) fundamental vibration and a decrease in the vibrational anharmonicity. Since v_{01} and Δ uniquely specify the Morse potential, we can extract Morse potential parameters from our 2D-IR data (details in the SI). A decrease in both v_{01} and Δ requires an *increase* in the dissociation energy. In chemical terms, vibrational excitation of CO bound to Cu within the protein's electrostatic environment produces a slightly bent Cu-CO bond where the CO bond is actually stronger (as measured from the minimum of the V_{CO} potential surface). Within the Morse model, in order for a bond to become stronger while exhibiting a spectroscopic red shift, it must become more harmonic. The harmonic force constant for a Morse oscillator, evaluated at the position of the potential minimum, is

$k_{harm} = 2a^2D_e$, where a is the Morse width parameter, and D_e is the classical dissociation energy. Since both a and D_e determine the harmonic force constant, conventional linear spectroscopy will not be able to sense the competing influences of the two potential parameters. We do note, however, that unconventional IR spectroscopy performed on a crystal of carboxymyoglobin has been able to determine the vibrational anharmonicity using the overtone (i.e. 0-2) transition, which is two orders of magnitude weaker than the fundamental.[100] This method is not likely to be widely applicable, however, especially for proteins that are difficult to crystallize. There is evidence in recent ATR 2D-IR experiments of reduced anharmonicity for nonlinear metal-CO bonds relative to nearly chemically identical linear metal-CO bonds.[101] Standard arguments from inorganic chemistry provide the rationale for the increase in CO dissociation energy: the Cu-CO bond angle tilt reduces the spatial overlap between the metal *d* orbitals and the CO π* orbitals, reducing back bonding and returning electron density to the CO which strengthens the bond. In fact, these arguments appear to be able to explain the paradoxical observation in heme proteins that increased deviation from linear metal-CO bond angles correlates with red shifted carbonyl vibrations, though those earlier experiments did not measure the vibrational anharmonicity. Finally, it is important to mention that the Morse oscillator is still a model of the CO interatomic potential, and is not exact. The changes we have measured are quite small, and it is evident that future work will need to model the CO potential energy surface using quantum chemistry.

2.3.9 Prospects for Future Design Innovations

The central question driving this chapter—one that we have not answered yet—is how to leverage the finding that histidine coordination can modulate the metal-ligand potential energy surface which likely plays a role in the catalysis. While addressing this challenge is a focus of ongoing and future investigations, we can make some general comments. In particular, having the potential ability to tune the reactivity somewhat remotely through the histidine coordination geometry enables design flexibility, since modifications can be made both "above" the Cu site (i.e. in the substrate binding cavity) and below the Cu site. Modifications in the binding site can exert structural control, for

example, by preforming the transition state species *via* a differential binding mechanism, whereas mutations below the binding site may influence the reactivity without necessarily altering the structural preformation. The histidine coordination geometry will be influenced both by packing and sterics in the core of the coiled-coil as well as by the longer range coupling to the electrostatics through the imidazole ring dipole moments. By varying the packing near the histidines, the steric interactions may be able to constrain the ring planes to be alternatively more co-planar or more aligned with the long axis of the coiled-coil. Since structural consequences of side chain modifications are not necessarily straightforward to predict, inserting bulky side chains near the histidines may directly act on the imidazole rings, or they may push out the peptide chains, which in turn strain the imidazole rings. Implementing and testing these design principles will benefit from our combined approach integrating synthesis, experiment, and computational modeling.

2.4 Conclusions

Using 2D-IR spectroscopy to investigate the vibrational dynamics of a CO vibrational probe bound to the active site of a *de novo* copper metalloenzyme, we find unexpected nonequilibrium frequency evolution with a 2 ps time scale. This experimental observation suggests a coupling between the high-frequency CO vibration and a much lower-frequency motion. DFT studies of the model active site and QM/MM (ONIOM) calculations of the full peptide trimer point to the importance of electrostatics in mediating the coupling between the CO stretch and the Cu-C-O bending motions. Our results show that the multidimensional potential energy surface of a ligand bound to a metal active site is acutely sensitive to the geometry of the histidine side chains coordinating the copper atom. This conclusion was motivated by observations of a novel dynamical signature in 2D-IR spectroscopy, attributed to a nonequilibrium, vibrationally triggered structural distortion, manifested as a continuous dynamical spectral shift of both the v_{01} and v_{12} transition frequencies. Guided by our QM/MM calculations, we find using DFT to investigate the small molecule that the coordination of the histidine side chains to Cu determines the CuCO potential energy surface. The histidines derive some

of their polarity from the metal coordination, which enhances their directional coupling to the protein's electrostatics. Future work to modify the electrostatics through mutation or by the synthesis of asymmetric heterodimers will enable rational design of the reaction's free energy surface, which we will be able to monitor with 2D-IR spectroscopy of the CO probe while comparing to QM/MM calculations that have been shown here to be consistent with experiment. Thus, there is promise that our combination of 2D-IR spectroscopy and quantum chemical modeling will enable directed, rational design of novel metalloenzymes by incorporating both long range electrostatics and side chain modifications. When combined with measurements of the enzyme's turn over frequency, we anticipate the combined approach will be able to provide a complete structural and dynamical picture of the catalysis.

2.5 References

1. Yu, F.; Cangelosi, V. M.; Zastrow, M. L.; Tegoni, M.; Plegaria, J. S.; Tebo, A. G.; Mocny, C. S.; Ruckthong, L.; Qayyum, H.; Pecoraro, V. L., Protein Design: Toward Functional Metalloenzymes. *Chem. Rev.* **2014,** *114*, 3495-3578.

2. Zastrow, M. L.; Peacock, A. F. A.; Stuckey, J. A.; Pecoraro, V. L., Hydrolytic catalysis and structural stabilization in a designed metalloprotein. *Nat. Chem.* **2012,** *4*, 118-123.

3. Tegoni, M.; Yu, F. T.; Bersellini, M.; Penner-Hahn, J. E.; Pecoraro, V. L., Designing a functional type 2 copper center that has nitrite reductase activity within alpha-helical coiled coils. *Proc. Natl. Acad. Sci. U. S. A.* **2012,** *109*, 21234-21239.

4. Yu, F. T.; Penner-Hahn, J. E.; Pecoraro, V. L., De Novo-Designed Metallopeptides with Type 2 Copper Centers: Modulation of Reduction Potentials and Nitrite Reductase Activities. *J. Am. Chem. Soc.* **2013,** *135*, 18096-18107.

5. Warshel, A.; Sharma, P. K.; Kato, M.; Xiang, Y.; Liu, H.; Olsson, M. H. M., Electrostatic basis for enzyme catalysis. *Chem. Rev.* **2006,** *106*, 3210-3235.

6. Warshel, A., Energetics Of Enzyme Catalysis. *Proc. Natl. Acad. Sci. U. S. A.* **1978,** *75*, 5250-5254.

7. Brooks, C. L.; Karplus, M., Solvent Effects on Protein Motion and Protein Effects on Solvent Motion - Dynamics of the Active-Site Region of Lysozyme. *J. Mol. Biol.* **1989,** *208*, 159-181.

8. Karplus, M.; Kuriyan, J., Molecular dynamics and protein function. *Proc. Natl. Acad. Sci. U. S. A.* **2005,** *102*, 6679-6685.

9. Hanggi, P.; Talkner, P.; Borkovec, M., Reaction-rate theory: fifty years after Kramers. *Rev. Mod. Phys.* **1991,** *62*, 251-342.

10. Hynes, J. T., Chemical-Reaction Dynamics in Solution. *Annu. Rev. Phys. Chem.* **1985,** *36*, 573-597.

11. Berne, B. J.; Borkovec, M.; Straub, J. E., Classical and Modern Methods in Reaction-Rate Theory. *J. Phys. Chem.* **1988,** *92*, 3711-3725.

12. Zwanzig, R., Rate-Processes with Dynamic Disorder. *Acc. Chem. Res.* **1990,** *23*, 148-152.

13. Fried, S. D.; Bagchi, S.; Boxer, S. G., Extreme electric fields power catalysis in the active site of ketosteroid isomerase. *Science* **2014,** *346*, 1510-1514.

14. Shurki, A.; Warshel, A., Structure/function correlations of proteins using MM, QM/MM, and related approaches: Methods, concepts, pitfalls, and current progress. *Protein Simulations* **2003,** *66*, 249-313.

15. Solomon, E. I.; Szilagyi, R. K.; George, S. D.; Basumallick, L., Electronic structures of metal sites in proteins and models: Contributions to function in blue copper proteins. *Chem. Rev.* **2004,** *104*, 419-458.

16. Zwanzig, R., Dynamic Disorder - Passage through a Fluctuating Bottleneck. *J. Chem. Phys.* **1992,** *97*, 3587-3589.

17. Min, W.; English, B. P.; Luo, G. B.; Cherayil, B. J.; Kou, S. C.; Xie, X. S., Fluctuating enzymes: Lessons from single-molecule studies. *Acc. Chem. Res.* **2005,** *38*, 923-931.

18. Minton, A. P., The influence of macromolecular crowding and macromolecular confinement on biochemical reactions in physiological media. *J. Biol. Chem.* **2001,** *276*, 10577-10580.

19. Hamm, P.; Zanni, M. T., *Concepts and Methods of 2D Infrared Spectroscopy*. Cambridge University Press: New York, 2011.

20. Fager, L. Y.; Alben, J. O., Structure of Carbon-Monoxide Binding-Site of Hemocyanins Studied by Fourier-Transform Infrared Spectroscopy. *Biochemistry* **1972,** *11*, 4786-4792.

21. Treuffet, J.; Kubarych, K. J.; Lambry, J. C.; Pilet, E.; Masson, J. B.; Martin, J. L.; Vos, M. H.; Joffre, M.; Alexandrou, A., Direct observation of ligand transfer and bond

formation in cytochrome c oxidase by using mid-infrared chirped-pulse upconversion. *Proc. Natl. Acad. Sci. U. S. A.* **2007,** *104*, 15705-15710.

22. Lemon, D. D.; Calhoun, M. W.; Gennis, R. B.; Woodruff, W. H., The Gateway to the Active-Site of Heme Copper Oxidases. *Biochemistry* **1993,** *32*, 11953-11956.

23. Lim, M. H.; Hamm, P.; Hochstrasser, R. M., Protein fluctuations are sensed by stimulated infrared echoes of the vibrations of carbon monoxide and azide probes. *Proc. Natl. Acad. Sci. U. S. A.* **1998,** *95*, 15315-15320.

24. Lim, M.; Jackson, T. A.; Anfinrud, P. A., Binding of CO To Myoglobin from a Heme Pocket Docking Site to Form Nearly Linear Fe-C-O. *Science* **1995,** *269*, 962-966.

25. Ray, G. B.; Li, X. Y.; Ibers, J. A.; Sessler, J. L.; Spiro, T. G., How Far Can Proteins Bend The FeCO Unit - Distal Polar and Steric Effects in Heme-Proteins and Models. *J. Am. Chem. Soc.* **1994,** *116*, 162-176.

26. Li, T. S.; Quillin, M. L.; Phillips, G. N.; Olson, J. S., Structural Determinants of the Stretching Frequency of CO Bound to Myoglobin. *Biochemistry* **1994,** *33*, 1433-1446.

27. Spiro, T. G.; Wasbotten, I. H., CO as a vibrational probe of heme protein active sites. *J. Inorg. Biochem.* **2005,** *99*, 34-44.

28. Ghosh, D.; Pecoraro, V. L., Understanding metalloprotein folding using a de novo design strategy. *Inorg. Chem.* **2004,** *43*, 7902-7915.

29. Dill, K. A.; Bromberg, S.; Yue, K. Z.; Fiebig, K. M.; Yee, D. P.; Thomas, P. D.; Chan, H. S., Principles of Protein-Folding - a Perspective from Simple Exact Models. *Protein Sci.* **1995,** *4*, 561-602.

30. Berne, B. J.; Weeks, J. D.; Zhou, R. H., Dewetting and Hydrophobic Interaction in Physical and Biological Systems. *Annu. Rev. Phys. Chem.* **2009,** *60*, 85-103.

31. Agashe, V. R.; Shastry, M. C. R.; Udgaonkar, J. B., Initial Hydrophobic Collapse in the Folding of Barstar. *Nature* **1995,** *377*, 754-757.

32. Gutin, A. M.; Abkevich, V. I.; Shakhnovich, E. I., Is Burst Hydrophobic Collapse Necessary for Protein-Folding. *Biochemistry* **1995,** *34*, 3066-3076.

33. Dieckmann, G. R.; McRorie, D. K.; Tierney, D. L.; Utschig, L. M.; Singer, C. P.; OHalloran, T. V.; PennerHahn, J. E.; DeGrado, W. F.; Pecoraro, V. L., De novo design of mercury-binding two- and three-helical bundles. *J. Am. Chem. Soc.* **1997,** *119*, 6195-6196.

34. Dieckmann, G. R.; McRorie, D. K.; Lear, J. D.; Sharp, K. A.; DeGrado, W. F.; Pecoraro, V. L., The role of protonation and metal chelation preferences in defining the properties of mercury-binding coiled coils. *J. Mol. Biol.* **1998,** *280*, 897-912.

35. Chang, W. C.; White, P. D., *Fmoc Solid Phase Peptide Synthesis, A Practical Approach, Vol. 222*. Oxford University Press Inc.: New York, 2000.

36. Farrer, B. T.; Harris, N. P.; Balchus, K. E.; Pecoraro, V. L., Thermodynamic model for the stabilization of trigonal thiolato mercury(II) in designed three-stranded coiled coils. *Biochemistry* **2001,** *40*, 14696-14705.

37. Zastrow, M. L.; Pecoraro, V. L., Influence of Active Site Location on Catalytic Activity in de Novo-Designed Zinc Metalloenzymes. *J. Am. Chem. Soc.* **2013,** *135*, 5895-5903.

38. Baiz, C. R.; Mcrobbie, P. L.; Anna, J. M.; Geva, E.; Kubarych, K. J., Two-Dimensional Infrared Spectroscopy of Metal Carbonyls. *Acc. Chem. Res.* **2009,** *42*, 1395-1404.

39. Christen, D.; Griffiths, J. H.; Sheridan, J., The Microwave-Spectrum of Imidazole - Complete Structure and the Electron-Distribution from Nuclear-Quadrupole Coupling Tensors and Dipole-Moment Orientation. *Z. Naturforsch., A: Phys. Sci.* **1981,** *36*, 1378-1385.

40. Aqvist, J.; Luecke, H.; Quiocho, F. A.; Warshel, A., Dipoles Localized at Helix Termini of Proteins Stabilize Charges. *Proc. Natl. Acad. Sci. U. S. A.* **1991,** *88*, 2026-2030.

41. Kwak, K.; Rosenfeld, D.; Fayer, M., Taking apart the two-dimensional infrared vibrational echo spectra: More information and elimination of distortions. *J. Chem. Phys.* **2008,** *128*, 204505.

42. Lazonder, K.; Pshenichnikov, M.; Wiersma, D., Easy interpretation of optical two-dimensional correlation spectra. *Opt. Lett.* **2006,** *31*, 3354-3356.

43. Roberts, S.; Loparo, J.; Tokmakoff, A., Characterization of spectral diffusion from two-dimensional line shapes. *J. Chem. Phys.* **2006,** *125*, 084502.

44. Hybl, J.; Christophe, Y.; Jonas, D., Peak shapes in femtosecond 2D correlation spectroscopy. *Chem. Phys.* **2001,** *266*, 295-309.

45. King, J. T.; Arthur, E. J.; Brooks, C. L.; Kubarych, K. J., Crowding Induced Collective Hydration of Biological Macromolecules over Extended Distances. *J. Am. Chem. Soc.* **2014,** *136*, 188-194.

46. King, J. T.; Kubarych, K. J., Site-specific coupling of hydration water and protein flexibility studied in solution with ultrafast 2D-IR spectroscopy. *J. Am. Chem. Soc.* **2012,** *134*, 18705-12.

47. Bagchi, S.; Nebgen, B. T.; Loring, R. F.; Fayer, M. D., Dynamics of a Myoglobin Mutant Enzyme: 2D IR Vibrational Echo Experiments and Simulations. *J. Am. Chem. Soc.* **2010,** *132*, 18367-18376.

48. Dixon, N. A.; McQuarters, A. B.; Kraus, J. S.; Soffer, J. B.; Lehnert, N.; Schweitzer-Stenner, R.; Papish, E. T., Dramatic tuning of ligand donor properties in (Ttz)CuCO through remote binding of H+ (Ttz = hydrotris(triazolyl)borate). *Chem. Commun.* **2013,** *49*, 5571-5573.

49. Faeder, S.; Jonas, D., Two-dimensional electronic correlation and relaxation spectra: Theory and model calculations. *J. Phys. Chem. A* **1999,** *103*, 10489-10505.

50. Kwak, K.; Park, S.; Finkelstein, I.; Fayer, M., Frequency-frequency correlation functions and apodization in two-dimensional infrared vibrational echo spectroscopy: A new approach. *J. Chem. Phys.* **2007,** *127*, 124503.

51. Gaffney, K.; Davis, P.; Piletic, I.; Levinger, N.; Fayer, M., Hydrogen bond dissociation and reformation in methanol oligomers following hydroxyl stretch relaxation. *J. Phys. Chem. A* **2002,** *106*, 12012-12023.

52. Huse, N.; Bruner, B. D.; Cowan, M. L.; Dreyer, J.; Nibbering, E. T. J.; Miller, R. J. D.; Elsaesser, T., Anharmonic couplings underlying the ultrafast vibrational dynamics of hydrogen bonds in liquids. *Phys. Rev. Lett.* **2005,** *95*, 147402.

53. Samanta, A., Dynamic stokes shift and excitation wavelength dependent fluorescence of dipolar molecules in room temperature ionic liquids. *J. Phys. Chem. B* **2006,** *110*, 13704-13716.

54. Castner, E.; Maroncelli, M., Solvent dynamics derived from optical Kerr effect, dielectric dispersion, and time-resolved Stokes shift measurements: An empirical comparison. *J. Mol. Liq.* **1998,** *77*, 1-36.

55. Stratt, R.; Maroncelli, M., Nonreactive dynamics in solution: The emerging molecular view of solvation dynamics and vibrational relaxation. *J. Phys. Chem.* **1996,** *100*, 12981-12996.

56. Maroncelli, M., The Dynamics of Solvation in Polar Liquids. *J. Mol. Liq.* **1993,** *57*, 1-37.

57. Baiz, C. R.; Kubarych, K. J.; Geva, E.; Sibert, E. L., Local-Mode Approach to Modeling Multidimensional Infrared Spectra of Metal Carbonyls. *J. Phys. Chem. A* **2011,** *115*, 5354-5363.

58. Frisch, M. J.; Trucks, G. W.; Schlegel, H. B.; Scuseria, G. E.; Robb, M. A.; Cheeseman, J. R.; Scalmani, G.; Barone, V.; Mennucci, B.; Petersson, G. A.; Nakatsuji, H.; Caricato, M.; Li, X.; Hratchian, H. P.; Izmaylov, A. F.; Bloino, J.; Zheng, G.; Sonnenberg, J. L.; Hada, M.; Ehara, M.; Toyota, K.; Fukuda, R.; Hasegawa, J.; Ishida, M.; Nakajima, T.; Honda, Y.; Kitao, O.; Nakai, H.; Vreven, T.; Montgomery Jr., J. A.; Peralta, J. E.; Ogliaro, F.; Bearpark, M. J.; Heyd, J.; Brothers, E. N.; Kudin, K. N.; Staroverov, V. N.; Kobayashi, R.; Normand, J.; Raghavachari, K.; Rendell, A. P.; Burant, J. C.; Iyengar, S. S.; Tomasi, J.; Cossi, M.; Rega, N.; Millam, N. J.; Klene, M.; Knox, J. E.; Cross, J. B.; Bakken, V.; Adamo, C.; Jaramillo, J.; Gomperts, R.; Stratmann, R. E.; Yazyev, O.; Austin, A. J.; Cammi, R.; Pomelli, C.; Ochterski, J. W.; Martin, R. L.; Morokuma, K.; Zakrzewski, V. G.; Voth, G. A.; Salvador, P.; Dannenberg, J. J.; Dapprich, S.; Daniels, A. D.; Farkas, Ö.; Foresman, J. B.; Ortiz, J. V.; Cioslowski, J.; Fox, D. J. *Gaussian 09, Revision A.02*, Gaussian, Inc.: Wallingford, CT, USA, 2009.

59. Dapprich, S.; Komaromi, I.; Byun, K. S.; Morokuma, K.; Frisch, M. J., A new ONIOM implementation in Gaussian98. Part I. The calculation of energies, gradients, vibrational frequencies and electric field derivatives. *J. Mol. Struct. Theochem* **1999,** *461*, 1-21.

60. Vreven, T.; Morokuma, K.; Farkas, O.; Schlegel, H. B.; Frisch, M. J., Geometry optimization with QM/MM, ONIOM, and other combined methods. I. Microiterations and constraints. *J. Comput. Chem.* **2003,** *24*, 760-769.

61. Vreven, T.; Byun, K. S.; Komaromi, I.; Dapprich, S.; Montgomery, J. A.; Morokuma, K.; Frisch, M. J., Combining quantum mechanics methods with molecular mechanics methods in ONIOM. *J. Chem. Theory Comput.* **2006,** *2*, 815-826.

62. Finkelstein, I.; Goj, A.; McClain, B.; Massari, A.; Merchant, K.; Loring, R.; Fayer, M., Ultrafast dynamics of myoglobin without the distal histidine: Stimulated vibrational echo experiments and molecular dynamics simulations. *J. Phys. Chem. B* **2005,** *109*, 16959-16966.

63. McClain, B.; Finkelstein, I.; Fayer, M., Dynamics of hemoglobin in human erythrocytes and in solution: Influence of viscosity studied by ultrafast vibrational echo experiments. *J. Am. Chem. Soc.* **2004,** *126*, 15702-15710.

64. McClain, B.; Finkelstein, I.; Fayer, M., Vibrational echo experiments on red blood cells: Comparison of the dynamics of cytoplasmic and aqueous hemoglobin. *Chem. Phys. Lett.* **2004,** *392*, 324-329.

65. Merchant, K.; Noid, W.; Akiyama, R.; Finkelstein, I.; Goun, A.; McClain, B.; Loring, R.; Fayer, M., Myoglobin-CO substate structures and dynamics: Multidimensional vibrational echoes and molecular dynamics simulations. *J. Am. Chem. Soc.* **2003,** *125*, 13804-13818.

66. Merchant, K.; Thompson, D.; Xu, Q.; Williams, R.; Loring, R.; Fayer, M., Myoglobin-CO conformational substate dynamics: 2D vibrational echoes and MD simulations. *Biophys. J.* **2002,** *82*, 3277-3288.

67. Falvo, C.; Daniault, L.; Vieille, T.; Kemlin, V.; Lambry, J.-C.; Meier, C.; Vos, M. H.; Bonvalet, A.; Joffre, M., Ultrafast Dynamics of Carboxy-Hemoglobin: Two-Dimensional Infrared Spectroscopy Experiments and Simulations. *J. Phys. Chem. Lett.* **2015,** *6*, 2216-2222.

68. Choi, J.-H.; Kwak, K.-W.; Cho, M., Computational Infrared and Two-Dimensional Infrared Photon Echo Spectroscopy of Both Wild-Type and Double Mutant Myoglobin-CO Proteins. *J. Phys. Chem. B* **2013,** *117*, 15462-15478.

69. Ishikawa, H.; Kwak, K.; Chung, J.; Kim, S.; Fayer, M., Direct observation of fast protein conformational switching. *Proc. Natl. Acad. Sci. U. S. A.* **2008,** *105*, 8619-8624.

70. Auer, B. M.; Skinner, J. L., IR and Raman spectra of liquid water: Theory and interpretation. *J. Chem. Phys.* **2008,** *128*.

71. Hayashi, T.; Jansen, T. L.; Zhuang, W.; Mukamel, S., Collective solvent coordinates for the infrared spectrum of HOD in D2O based on an ab initio electrostatic map. *J. Phys. Chem. A* **2005,** *109*, 64-82.

72. Hayashi, T.; Zhuang, W.; Mukamel, S., Electrostatic DFT map for the complete vibrational amide band of NMA. *J. Phys. Chem. A* **2005,** *109*, 9747-9759.

73. Lin, Y. S.; Shorb, J. M.; Mukherjee, P.; Zanni, M. T.; Skinner, J. L., Empirical Amide I Vibrational Frequency Map: Application to 2D-IR Line Shapes for Isotope-Edited Membrane Peptide Bundles. *J. Phys. Chem. B* **2009,** *113*, 592-602.

74. Wang, L.; Middleton, C. T.; Zanni, M. T.; Skinner, J. L., Development and Validation of Transferable Amide I Vibrational Frequency Maps for Peptides. *J. Phys. Chem. B* **2011,** *115*, 3713-3724.

75. Zhuang, W.; Abramavicius, D.; Hayashi, T.; Mukamel, S., Simulation protocols for coherent femtosecond vibrational spectra of peptides. *J. Phys. Chem. B* **2006,** *110*, 3362-3374.

76. Falvo, C.; Meier, C., A fluctuating quantum model of the CO vibration in carboxyhemoglobin. *J. Chem. Phys.* **2011,** *134*.

77. Asbury, J.; Steinel, T.; Fayer, M., Vibrational echo correlation spectroscopy probes of hydrogen bond dynamics in water and methanol. *J. Lumin.* **2004,** *107*, 271-286.

78. Gaffney, K.; Piletic, I.; Fayer, M., Orientational relaxation and vibrational excitation transfer in methanol-carbon tetrachloride solutions. *J. Chem. Phys.* **2003,** *118*, 2270-2278.

79. Levinger, N.; Davis, P.; Fayer, M., Vibrational relaxation of the free terminal hydroxyl stretch in methanol oligomers: Indirect pathway to hydrogen bond breaking. *J. Chem. Phys.* **2001,** *115*, 9352-9360.

80. Piletic, I.; Gaffney, K.; Fayer, M., Structural dynamics of hydrogen bonded methanol oligomers: Vibrational transient hole burning studies of spectral diffusion. *J. Chem. Phys.* **2003,** *119*, 423-434.

81. Kwac, K.; Geva, E., A Mixed Quantum-Classical Molecular Dynamics Study of the Hydroxyl Stretch in Methanol/Carbon Tetrachloride Mixtures: Equilibrium Hydrogen-Bond Structure and Dynamics at the Ground State and the Infrared Absorption Spectrum. *J. Phys. Chem. B* **2011,** *115*, 9184-9194.

82. Kwac, K.; Geva, E., Mixed Quantum-Classical Molecular Dynamics Study of the Hydroxyl Stretch in Methanol/Carbon-Tetrachloride Mixtures II: Excited State Hydrogen Bonding Structure and Dynamics, Infrared Emission Spectrum, and Excited State Lifetime. *J. Phys. Chem. B* **2012,** *116*, 2856-2866.

83. Dwyer, J.; Dreyer, J.; Nibbering, E.; Elsaesser, T., Ultrafast dynamics of vibrational N-H stretching excitations in the 7-azaindole dimer. *Chem. Phys. Lett.* **2006,** *432*, 146-151.

84. Elsaesser, T.; Huse, N.; Dreyer, J.; Dwyer, J.; Heyne, K.; Nibbering, E., Ultrafast vibrational dynamics and anharmonic couplings of hydrogen-bonded dimers in solution. *Chem. Phys.* **2007,** *341*, 175-188.

85. Heyne, K.; Huse, N.; Dreyer, J.; Nibbering, E.; Elsaesser, T.; Mukamel, S., Coherent low-frequency motions of hydrogen bonded acetic acid dimers in the liquid phase. *J. Chem. Phys.* **2004,** *121*, 902-913.

86. Heyne, K.; Huse, N.; Nibbering, E.; Elsaesser, T., Ultrafast coherent nuclear motions of hydrogen bonded carboxylic acid dimers. *Chem. Phys. Lett.* **2003,** *369*, 591-596.

87. Heyne, K.; Huse, N.; Nibbering, E.; Elsaesser, T., Coherent vibrational dynamics of intermolecular hydrogen bonds in acetic acid dimers studied by ultrafast mid-infrared spectroscopy. *J. Phys.-Condes. Matter* **2003,** *15*, S129-S136.

88. Heyne, K.; Huse, N.; Nibbering, E.; Elsaesser, T., Ultrafast relaxation and anharmonic coupling of O-H stretching and bending excitations in cyclic acetic acid dimers. *Chem. Phys. Lett.* **2003,** *382*, 19-25.

89. Baker, N. A.; Sept, D.; Joseph, S.; Holst, M. J.; McCammon, J. A., Electrostatics of nanosystems: Application to microtubules and the ribosome. *Proc. Natl. Acad. Sci. U. S. A.* **2001,** *98*, 10037-10041.

90. Sundberg, R. J.; Martin, R. B., Interactions of Histidine and Other Imidazole Derivatives with Transition-Metal Ions in Chemical and Biological-Systems. *Chem. Rev.* **1974,** *74*, 471-517.

91. Tipmanee, V.; Blumberger, J., Kinetics of the Terminal Electron Transfer Step in Cytochrome c Oxidase. *J. Phys. Chem. B* **2012,** *116*, 1876-1883.

92. Schmiedekamp, A.; Nanda, V., Metal-activated histidine carbon donor hydrogen bonds contribute to metalloprotein folding and function. *J. Inorg. Biochem.* **2009,** *103*, 1054-1060.

93. Horowitz, S.; Trievel, R. C., Carbon-Oxygen Hydrogen Bonding in Biological Structure and Function. *J. Biol. Chem.* **2012,** *287*, 41576-41582.

94. Karlin, K. D.; Dahlstrom, P. L.; Dipierro, L. T.; Simon, R. A.; Zubieta, J., X-Ray Structure-Analysis of a Dicopper Complex of a New Binucleating Ligand Containing a Para-Xylyl Connecting Group - Large Cu...Cu Separation in [(CuCl2C18H20N3)2].2H2O. *J. Coord. Chem.* **1981,** *11*, 61-63.

95. Moore, J. N.; Hansen, P. A.; Hochstrasser, R. M., Iron Carbonyl Bond Geometries of Carboxymyoglobin and Carboxyhemoglobin in Solution Determined by Picosecond Time-Resolved Infrared Spectroscopy. *Proc. Natl. Acad. Sci. U. S. A.* **1988,** *85*, 5062-5066.

96. Spiro, T. G.; Kozlowski, P. M., Is the CO adduct of myoglobin bent, and does it matter? *Acc. Chem. Res.* **2001,** *34*, 137-144.

97. Spiro, T. G.; Kozlowski, P. M., Discordant results on FeCO deformability in heme proteins reconciled by density functional theory. *J. Am. Chem. Soc.* **1998,** *120*, 4524-4525.

98. Gordon, R. G., Correlation Functions for Molecular Motion. *Advances in Magnetic and Optical Resonance* **1968,** *3*, 1-42.

99. Morse, P. M., Diatomic molecules according to the wave mechanics. II. Vibrational levels. *Physical Review* **1929,** *34*, 57-64.

100. Sage, J. T.; Zhang, Y. B.; McGeehan, J.; Ravelli, R. B. G.; Weik, M.; van Thor, J. J., Infrared protein crystallography. *Biochimica Et Biophysica Acta-Proteins and Proteomics* **2011,** *1814*, 760-777.

101. Kraack, J. P.; Lotti, D.; Hamm, P., Ultrafast, Multidimensional Attenuated Total Reflectance Spectroscopy of Adsorbates at Metal Surfaces. *J. Phys. Chem. Lett.* **2014,** *5*, 2325-2329.

Chapter 3

Analysis of Another *de novo* Metalloenzyme with Improved Modeling

3.1 Introduction

Following the first report of the *de* novo metalloenzyme that served as the basis for the enzyme in the previous chapter,[1] considerable advances have been made to improve both the zinc[2] and copper[3, 4] enzymes based on the TRI scaffold. In addition, other approaches, such as using a homodimer of a helix-turn-helix structure[5] and short amyloid-forming peptides[6] have improved on the catalytic activity of the original zinc peptide by an order of magnitude. Despite these improvements, the artificial enzymes are still several times less active than carbonic anhydrase II based on the hydrolysis of *p*-nitrophenylacetate, which is not the natural substrate of the incredibly active enzyme. With respect to the biologically relevant hydration of CO_2, the zinc *de novo* enzymes still lag two orders of magnitude behind the natural enzyme.[1] Clearly there is a real possibility to enhance the engineered peptides, but the design space is large and we would like to develop a hybrid approach based on computation and experiment.

One way to accelerate design while building a physical basis for the enzyme's function is to establish a rapid and reliable way to model the whole macromolecule, with a focus on the active site. For example, it is not necessarily straightforward to predict the impact of some of the mutations made to the TRI peptides, such as moving the metal site[2] or changing the residues near the active site so the net charge on the enzyme is reduced.[4] The modeling method used for our first investigations into the TRI peptide family[7] can be improved, making the overall process both faster and more accurate by judiciously optimizing the generation of the starting structure for the QM/MM calculations. Our previous method of preparing the force-field minimized structure for the ONIOM minimization (and other calculations) was performed using a

force field that differed from that used for the rest of the calculations. This choice was made based solely on practicality. Bonds involving copper are not parameterized in many force fields, but they are contained in the Universal Force Field (UFF),[8] so UFF was used for the initial minimization. The inclusion of these parameters in UFF has made it useful for other QM/MM calculations including copper enzymes.[9-11] Using UFF for the initial minimization followed by the AMBER96 force field[12, 13] in the MM layer of the ONIOM calculation almost certainly introduces errors due to the mismatch of force fields. Degrees of freedom frozen in the ONIOM calculation reflect the UFF minimum, rather than the minimum appropriate for the AMBER parameters. Minimizing the structure using AMBER would require the atoms involving undefined parameters either to be frozen or to have values assigned to them.

Freezing the atoms that have undefined parameters is a crude but efficient way to start the MM minimization. Although freezing some atoms limits conformational sampling, the atoms that are frozen will be unrestrained in the ONIOM minimization. The DFT analogue used in the previous chapter has a geometry that, while not strained by the electrostatic or van der Waals forces of the peptide, will provide a good MD starting point, as those atoms will later be minimized more accurately in the ONIOM calculations. A better but more time consuming approach would be to iteratively minimize the QM and MM atoms, keeping certain atoms fixed in each step as proposed by Alexandrova et al.[14]

Alternatively, the potential energy for each unknown parameter could be calculated using DFT to stretch bonds, bend angles, and twist dihedrals to obtain the missing values for the force field. This information about how the energy of the system changes as atoms are moved can also be obtained from the Hessian, a matrix of force constants generated during DFT frequency calculations. A reliable method for calculating force field parameters from the Hessian was developed by Seminario[15] and has been used to quickly generate parameters for more exotic bonds, angles, and dihedrals by several groups.[16-22] While not completely accurate due to the assumption that the calculated parameters are unstrained,[23] the parameters generated using

Seminario's method provide a more flexible starting geometry for the QM/MM calculations. By combining the parameters obtained by DFT on the small-molecule analogue with the existing parameters of the AMBER96 force field, the coordinates obtained either starting with or modified from a crystal structure can be minimized using a molecular dynamics package such as GROMACS.[24] The resulting minimized structure should give more useful inputs for the next step – the ONIOM calculation – which relaxes all degrees of freedom, and where the force field used to obtain the minimized input is the same one used in the MM layer.

3.2 Materials and Methods

3.2.1 Sample Preparation

The peptide sample studied experimentally has the formula $[(TRIL2WL19AL23_{\delta M}H)_3Cu(I)(CO)]^+$ and was prepared in the same method as the peptide sample in Chapter 2, except the yield of vibrationally labeled peptide was increased by using a greater ratio of copper(I) solution with respect to the peptide concentration. The resulting labeled peptide concentration was ~2-3 mM. The sample cell used was also standard, consisting of two 25 mm x 3 mm calcium fluoride windows separated by a 100 μm Teflon spacer. Vacuum grease was placed around the edge of interior of the sample cell to reduce oxidation. The cell was not compressed as tightly as other, non-peptide, samples in order to maximize the usable area in the cell, resulting in a slightly longer path length than other samples.

3.2.2 2D-IR Details

The 2D-IR setup is the same as previously reported.[25-27] Spectra were collected at waiting times ranging from -0.2 to 2.0 ps in 0.1 ps steps, 2.25 to 5.0 ps in steps of 0.25 ps, 5.5 to 30 ps in steps of 0.5 ps, and 31 to 45 ps in 1 ps steps. Rephasing and nonrephasing spectra were collected, but only the rephasing spectra were analyzed to obtain anharmonicity measurements, as described in the Chapter 2.

3.2.3 Molecular Dynamics Setup

All molecular dynamics calculations were performed in GROMACS[24] 4.5.5 using the AMBER96[13] force field with the SPC/E[28] water model where necessary. The structures of the TRI peptides studied were based on the crystal structure of a similar CoilSer peptide (PDB code 3PBJ).[1] Simulations performed in water had a single chloride ion added to neutralize the charge on the system. Energy minimization was performed with the steepest descent algorithm, an initial step size of 0.01 nm, and stopped at a limit of 100,000 steps or once a maximum force of 10.0 kJ/mol/nm was reached. For molecular dynamics simulations, the system was first equilibrated using a canonical (NVT) simulation for 100 ps followed by an isothermal-isobaric (NPT) simulation for 100 ps, both with step sizes of 2 fs for 50,000 steps at a temperature of 300 K using the V-Rescale thermostat with a time constant of 0.1 ps. The NPT simulation was run with Parrinello-Rahman pressure coupling with a time constant of 2 ps at 1.0 bar. The dynamics simulation was run with a step size of 1 fs for 5 ns.

Atomic charges for the $(His)_3Cu(CO)^+$ unit were calculated using RESP[29] as implemented in Amber.[30] To obtain more accurate charges, the histidine groups were capped with formyl and amine groups. The structure $(HOC\text{-}His\text{-}NH_2)_3Cu(CO)^+$ was optimized in Gaussian 09 using the B3LYP functional and 6-311G(d,p) basis set. That optimized structure was then used for the standard RESP calculations.

3.2.4 DFT and ONIOM Setup

All DFT and ONIOM calculations were performed using the Gaussian 09 software suite.[31] DFT calculations used the B3LYP functional and 6-311G(d,p) basis set for all atoms. In geometry optimizations, symmetry was disabled and tight optimization criteria were imposed. In the ONIOM calculations, the B3LYP/6-311G(d,p) level of theory was used for the QM layer and the AMBER force field was used for the MM layer. The QM layer consisted of the copper atom, carbonyl, and all histidine or methyl-substituted histidine residues up to the C_β, with the C_α used as a link atom that is replaced by a hydrogen atom in the QM calculations. ONIOM calculations were performed using

electronic embedding and microiterations with a quadratic coupled algorithm. Similarly to the DFT calculations, the ONIOM geometry optimizations were performed with symmetry disabled and with tight optimization criteria. Atoms farther than 4 residues from the histidine residue were frozen to reduce computational time.

3.3 Results and Discussion

3.3.1 Simulated Movement of the Active Site

The first series of peptides simulated were based on moving the active site of the metalloenzyme closer to the N-terminus of the peptide.[2] Three different histidine locations were established by mutating residues 9, 16, and 23 from leucine so that a copper carbonyl could be introduced. These residues are each in the same location on the repeating heptad, so each carbonyl is expected to remain in the hydrophobic interior of each peptide trimer, as shown in Figure 3.1. A note on the syntax used hereafter: the least-substituted peptide is TRIW [sequence Ac-G WKALEEK $(LKALEEK)_3$ G-NH_2] and unless otherwise noted the histidine is substituted in the 23^{rd} residue, making the sequence of TRIW-H [Ac-G WKALEEK $(LKALEEK)_2$ **H**KALEEK G-NH_2]. The tryptophan in the second position is a UV probe that allows for the calculation of stock peptide solution concentration. In three of the structures shown in Figure 3.1 the isomer D-histidine was used in place of the natural L-histidine, as it is expected to bind the copper carbonyl in the opposite direction with the oxygen atom towards the C-terminus. This shift allows the carbonyl to be placed at essentially the same location (though with the carbon and oxygen atoms switched) using two different sites on the backbone, as seen in TRIW-H and TRIW-L16dH. The motivation to consider two peptides with carbonyls in the same location was originally intended to gauge whether the vibrational excitation-driven carbonyl tilting was due to a Stark effect. Based on the considerations laid out in Chapter 2, we do not attribute a significant role to the Stark effect, but the two structural analogues should still give insight into how important the carbonyl and histidine locations are independently.

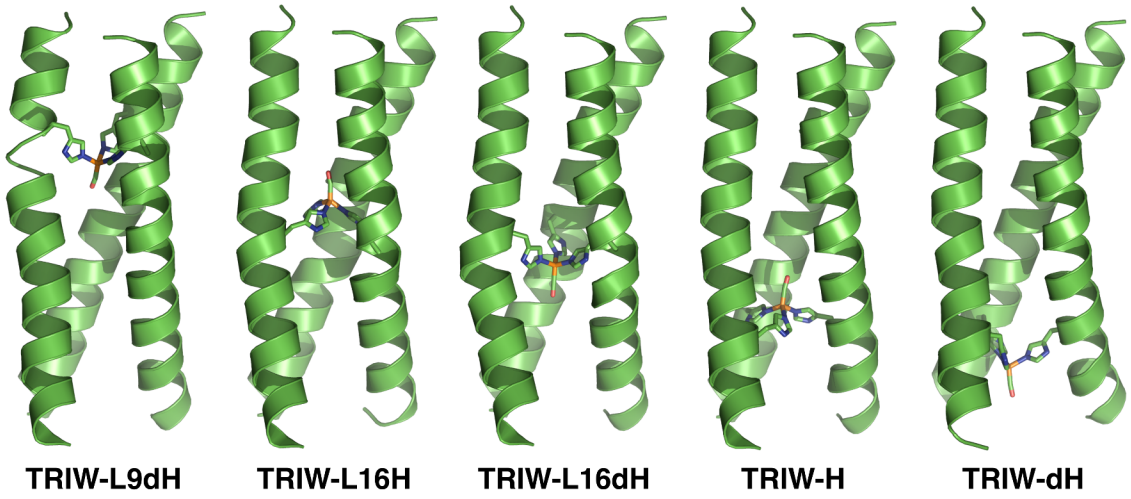

Figure 3.1 ONIOM-minimized Structures of $(TRI)_3Cu(I)(CO)$ for five TRI sequences. In order from left to right, the histidine site was placed at the 9th, 16th, 16th, 23rd, and 23rd residue. The isomer D-histidine (dH) is expected to bind CO pointing towards the C-terminus, as shown in the structures of TRIW-L9dH, TRIW-L16dH, and TRIW-dH.

Table 3.1 Summary of methods used to minimize system prior to ONIOM calculations

Minimization Shorthand	Starting Structure	Active Site Treatment	MM Force Field Used
UFF	Crystal Structure (3PBJ)	UFF	UFF
Frozen	Crystal Structure (3PBJ)	Frozen in DFT configuration	AMBER96
AMBER	MD Simulation	Parameters from Hessian	AMBER96

The structures shown in Figure 3.1 were first minimized in GROMACS using the AMBER96 force field, but keeping the copper carbonyl and histidine side chains frozen (shorthand "Frozen" in Table 3.1) because we had not yet calculated their parameters. This structure was then further minimized using ONIOM, the results of which are discussed below. All of the structures in Figure 3.1 are fairly similar, especially with respect to the helices, but there are small differences between several of the structures due to moving the histidine site. For example, in the TRIW-L9dH mutant, the leftmost helix is distorted enough that it is not recognized as helical near the metal site. Also, in TRIW-L16dH mutant the cylindrical coils bulge out slightly. The helices are suspected to remain symmetric even when the active site is relocated, as the circular dichroism

spectra for TRIL23H, TRIL9CL23H, TRIL9HL23C, and TRIL9CL19H are similar, with a characteristic double well at 208 and 222 nm, indicating the presence of a coiled coil.[1, 2] The structures from the frozen minimization reflect this configuration better and are more symmetric than the structure obtained by first minimizing with UFF, as shown in Figure 3.2, where the UFF-minimized structure (in green) has several regions that are not helical near the active site. The AMBER minimized structure of TRIW-H has an ONIOM-calculated energy that is 3933 kJ/mol lower than the UFF structure, highlighting the importance of a good starting structure.

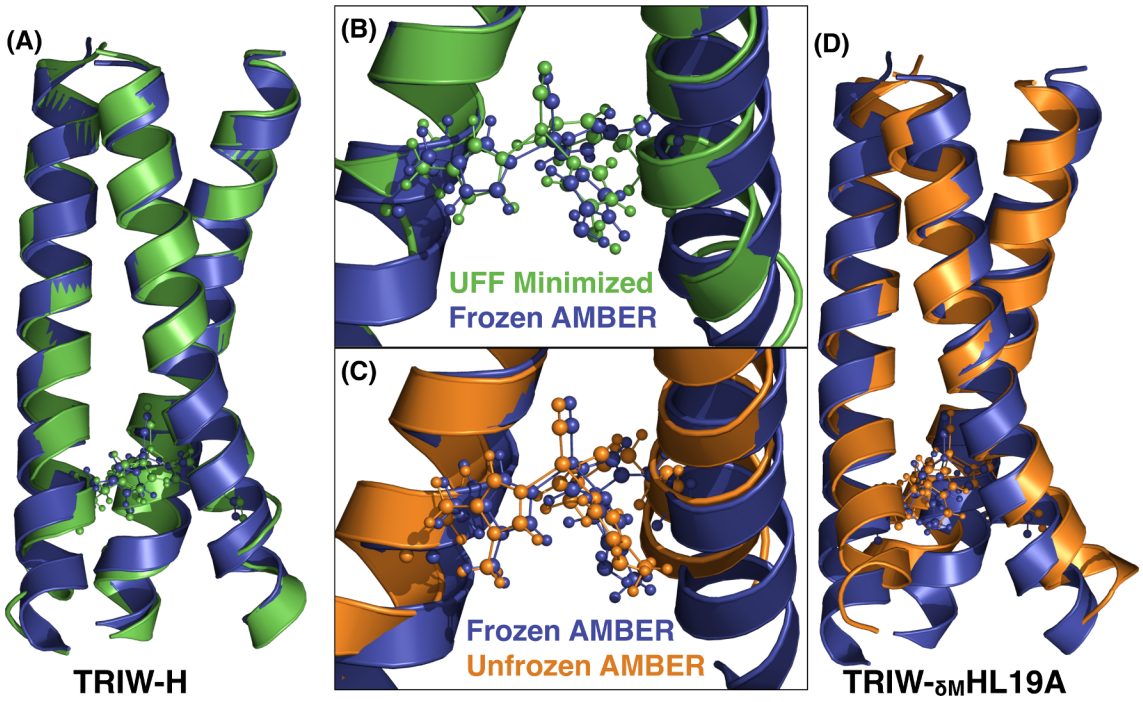

Figure 3.2 Structures of two different peptides using three different methods of minimizing the structure with MM prior to ONIOM calculations, which are set up identically in all three cases. (A) shows the TRIW-H peptide and compares the structures obtained starting with a UFF-minimized structure (green) and AMBER-minimized with the active site frozen (blue). (B) Is the same structure as (A) but zoomed in on the copper site. (C) shows the active site of TRIW-$_{\delta M}$HL19A when starting with an AMBER-minimized structure with the active site frozen (blue) or unfrozen with added parameters (orange). (D) shows the greater structure of the same peptide as (C).

After the MM minimization was completed, the system was optimized using the ONIOM method detailed in the methods section. The C-O distance of the carbonyl was then stretched to 110% of the optimized bond length to simulate vibrational excitation,

whereupon the rest of the system was re-optimized using ONIOM. The results of these calculations are shown in Table 3.2. The three mutants with D-histidine have dihedral angles greater than the L-histidine mutants because the carbonyl is pointing in the opposite direction. Comparing the two different TRIW-H results, the structure that was first minimized with AMBER had a nearly two-fold larger change in Cu-C-O bond angle upon vibrational excitation than the original UFF structure, despite a smaller average ground vibrational state dihedral angle. This finding is surprising, since we would expect the smaller (61° versus 73°) dihedral angle to correlate with a reduced excited-state tilt. The histidine rings do bind to the copper at a slightly different angle, as seen in Figure 3.2B, which could lead to a similar effect as the twisting of the dihedral angle, as it results in a change in the electron density between the atoms. A future investigation will systematically vary only a single imidazole ring's dihedral angle to characterize the impact of structural heterogeneity.

Table 3.2 Calculated values of several different peptides in the TRI family. The histidine is the 23rd residue unless otherwise noted. The isomer D-histidine is represented by dH. Histidine residues methylated at the N_δ or N_ε are noted by δM and εM, respectively. The MM minimization is the method used to generate the starting ONIOM geometry as detailed in

Table 3.1. The calculated CO frequencies are unscaled.

Peptide Sequence	MM Min.	Ground θ_{CuCO} (Deg.)	Excited θ_{CuCO} (Deg.)	$\Delta\theta_{CuCO}$ (Deg.)	Ground $\theta_{Dihedral}$	Calculated ν_{CO} (cm^{-1})
TRIW-H	UFF	171.4	164.8	6.58	73.0	2107.3
TRIW-H	Frozen	170.7	158.1	12.61	61.3	2121.4
TRIW-dH	Frozen	173.6	163.7	9.92	150.8	2125.8
TRIW-L16H	Frozen	167.9	161.5	6.34	75.6	2116.3
TRIW-L16dH	Frozen	175.0	165.4	9.55	137.3	2144.8
TRIW-L9dH	Frozen	168.9	162.5	6.40	153.6	2139.6
TRIW-HL19A	Frozen	174.3	162.6	11.76	59.2	2126.9
TRIW-$_{\delta M}$H	Frozen	175.6	170.3	5.34	66.4	2131.9
TRIW-$_{\delta M}$HL19A	Frozen	174.0	166.6	7.42	65.2	2131.7
TRIW-$_{\delta M}$HL19A	AMBER	176.1	164.0	12.07	59.4	2142.7
TRIW-$_{\varepsilon M}$H	AMBER	174.1	166.3	7.78	42.7	2142.4

Comparing the two sets of shifted active sites where the carbonyls are in approximately the same location, it appears that the carbonyl tilts more when the histidine orientation places the carbonyl between the 16 and 23 positions (TRIW-H and TRIW-L16dH) than when placed between the 16 and 9 positions (TRIW-L16H and TRIW-L9dH). The calculated Cu-C-O angle change is slightly less for TRIW-L16dH (9.6°) than TRIW-H (12.6°), but both are greater than TRIW-L16H (6.3°) and TRIW-L9dH (6.4°). The calculated frequencies are also greater for carbonyls above the 23 position by about 5 cm^{-1}, although both of the D-histidine peptides have a frequency about 20 cm^{-1} greater than the comparable L-histidine residue with CO in the same location. This difference could be due to a Stark shift, but additional calculations explicitly considering the electrostatics of the complex interior would be needed to determine the origin more reliably. Positioning the active site closer to the N-terminus has been shown experimentally to lower the catalytic activity of a similar zinc peptide,[2] although in the experiment it was moved to the 19 position and not by a full heptad as done in these calculations. The different location in the heptad could lead to a change in how the histidines bind copper, as the distance to the metal from the backbone will be different for this new location on the heptad. For example, the histidine residues may favor bonding through the N_ε instead of the N_δ seen in the crystal structure of the CoilSer peptide.[1] The different atoms in histidine are labeled in Figure 3.3 with the nomenclature used throughout this chapter.

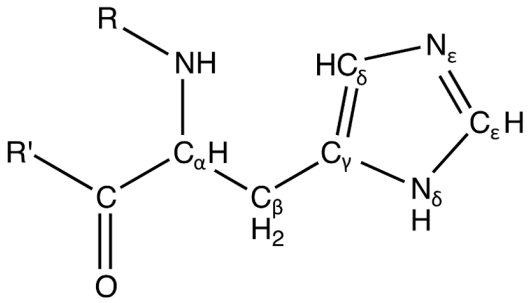

Figure 3.3 Structure of histidine with carbon and nitrogen positions labeled with Greek letters. At the pH used, either N_δ or N_ε is expected to be protonated. The histidine will bind copper through the non-protonated nitrogen.

The TRIW-dH peptide is interesting because the carbonyl would likely be solvent-exposed. The potential energy surface shows fairly similar properties to the TRIW-L16dH peptide in terms of angle change and ground state Cu-C-O angle, but the dihedral angle and frequency are significantly different. Interestingly, the frequency of the TRIW-dH peptide is the lowest of the D-histidine residues and is relatively close to the CO frequency of TRIW-H, differing by 4.4 cm^{-1} instead of the 28 cm^{-1} difference seen between the two L16H peptides. In future calculations, the solvent can be included in the MM layer of the ONIOM calculation so that hydrogen bonding could potentially be seen, assuming there is water near the carbonyl.

3.3.2 Simulated Changes to Nearby Residues

The most obvious change to the peptide would be to alter residues near the active site. Reducing the charge around the copper site was found to improve the nitrite reductase activity of the copper *de novo* metalloenzyme,[4] but an even greater improvement was seen using a non-natural histidine residue where the N_δ has a methyl group attached instead of a hydrogen atom.[32] Methylating one of the nitrogen atoms in histidine forces the copper to bind to the other nitrogen in the imidazole ring and also changes the electron density on the histidine. Another change near the active site that increases the catalytic performance is to replacing the leucine residue directly above the active site on the interior of the peptide with the considerably smaller alanine residue. This substitution of a nearby bulky group for a smaller one has been shown to influence the shape of the metal binding site in a similar metalloenzyme.[33, 34] The consequences of methylating the histidine residues and changing the larger leucine groups to alanine residues was studied by modeling TRIW-$_{\delta M}$H, TRIW-$_{\delta M}$HL19A, TRIW-HL19A, and TRIW-$_{\varepsilon M}$H, where the δM and εM refer to the N_δ or N_ε in histidine being methylated, respectively (see Figure 3.3). The ONIOM-optimized structures of the three methylated peptides are shown in Figure 3.4.

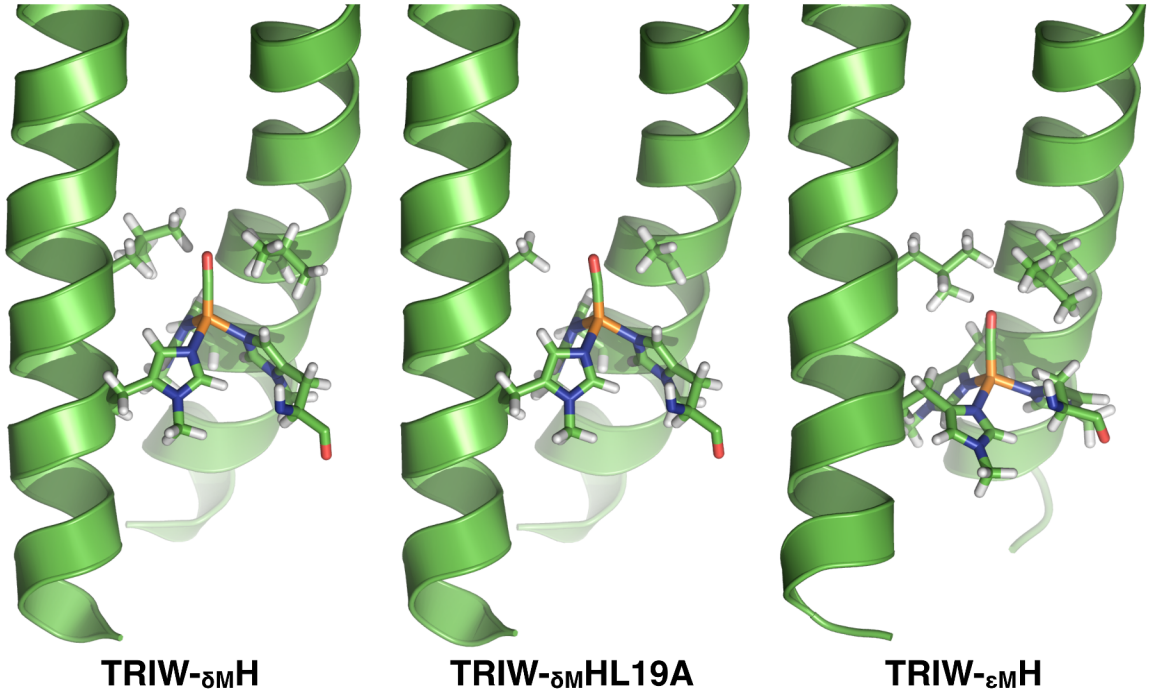

Figure 3.4 Optimized structure of several peptides showing methylated histidine residues and the residue in the 19th position. The two structures with the N_δ methylated have the copper bound higher in the cavity while the peptide with the N_ε methylated binds copper through the N_δ and has a smaller dihedral angle. The L19A substitution results in a less crowded pocket above the metal site.

The starting structures of TRIW-$_{\delta M}$H, TRIW- $_{\delta M}$HL19A, and TRIW-HL19A were generated using the same frozen AMBER method described in the previous section. Minimizing the structure of TRIW-$_{\varepsilon M}$H was not feasible with this method, as the histidine residues are bonded to the copper atom through the N_δ instead of the N_ε used in the other peptides in this work and the crystal structure they are based on (PDB code 3PBJ).[1] This perturbation to the active site is larger than the other modifications made to the peptide where the active site was relocated. When moving the active site, the histidine residues should remain bonded in much the same way, as only the number of heptads before and after the active site are changing. Changing the copper-binding nitrogen atom results in a change in the position of the C_β (Figure 3.4), which would not be observed if the atom is frozen. To sample the active site reorganization, any force field parameters not defined in AMBER were generated using the method described by Seminario.[15] The Hessian used was from the DFT-optimized structure to calculate atomic charges. Using these newly generated parameters, a 5 ns molecular dynamics simulation

was run without any atoms frozen, as described in the methods section. The lowest energy structure from the simulation after the first nanosecond was selected and minimized without solvent to use as the starting point for the ONIOM calculations. The structure obtained from this fully parameterized method for TRIW-$_{\varepsilon M}$H is shown in Figure 3.4.

The structure for TRIW-$_{\delta M}$HL19A, the peptide with the highest observed nitrite reduction rate constant,[32] was also minimized using the fully-parameterized, unfrozen AMBER method as TRIW-$_{\varepsilon M}$H. The structures obtained using this newer method and the frozen AMBER minimization are compared in Figure 3.2C and D, with the frozen method shown in blue and the structure minimized starting with the newer method in orange. The fully AMBER minimized structure has an ONIOM extrapolated energy that is 616 kJ/mol lower than the frozen AMBER method, again showing considerable improvement from the better starting structure. The active site is largely unchanged between the two methods, with only a 6° difference in mean dihedral angle and 2° difference in CuCO bond angle. There are larger structural differences between the two methods, especially towards the C-terminus (bottom of Figure 3.2D) where the structure minimized from the MD simulation is less helical. The structural change is due to the bulkier methyl-histidine causing a slight uncoiling of the coiled-coil structure and stabilized by positively charged lysine residues hydrogen-bonding with nearby negatively charged glutamic acid residues (i.e. the formation of salt bridges). This uncoiling was only observed in the structure where the conformational space was searched by performing an MD simulation.

Comparing the ONIOM-calculated frequencies in Table 3.2 for this second group of peptides, a few features stand out. The L19A substitution appears to cause almost no change in the active site. The ground state CuCO angle is straighter by 4° in TRIW-HL19A compared to TRIW-H, but the same angle is 1.6° more bent when the N_δ is methylated. The CuCO angle changes after excitation are even more similar, changing by 2° and 1°, respectively, and the average dihedral angles only differ by 1-2° as well. There is a more noticeable difference between the peptides with natural histidine and those with N_δ-

methyl-histidine, though. Notably, the CuCO angle change is about half as large for the methylated active site, which would mean that a smaller angle change, and with it a smaller frequency shift would be expected for the methylated histidine. The smaller change in angle could also mean a faster anharmonicity decay in the 2D-IR spectra, and a small magnitude change in the apparent anharmonicity. These predictions have been tested experimentally, as will be discussed in the following section.

Fewer comparisons can be made between the sequences optimized using the full AMBER MD minimization, as only two have been calculated with that approach – TRIW-$_{\delta M}$HL19A and TRIW-$_{\varepsilon M}$H. The two different methods of minimizing TRIW-$_{\delta M}$HL19A yield few similarities from the ONIOM calculations. Indeed, the AMBER minimized results resemble the TRIW-HL19A with similar angle changes, mean dihedral angles, and ground state CuCO bond angles. Without a full AMBER optimized structure of TRIW-H or TRIW-$_{\delta M}$H, it is difficult to make more conclusive observations at this time. The structures of TRIW-H, TRIW-$_{\delta M}$H, and TRIW-HL19A should also be compared using the full AMBER minimization followed by ONIOM calculations scheme. This allows the contributions from the L19A mutation and methylation to be separated. Comparing the ONIOM results for the structures that have been calculated using this method, TRIW-$_{\varepsilon M}$H with those of TRIW-$_{\delta M}$HL19A is interesting, as both have almost identical harmonic frequencies but the dihedral angle of TRIW-$_{\varepsilon M}$H is the lowest calculated. This difference in dihedral angle is understandable, as a different nitrogen atom is bound to the copper, causing it to bond at a slightly different angle. This difference can be seen in Figure 3.4, where it is also shown that the copper is closer to the C-terminus by 3 Å when the histidine binds through the N_{δ}.

3.3.3 2D-IR Shows a Smaller Anharmonicity Decay in Better Catalyst

All of the modeling done to this point has been helpful in trying to predict properties of the enzyme structure, but being able to relate the predicted angle change to a different anharmonicity decay – either a change in the amplitude or the time scale – would tie the simulations more directly to physical observables. Deciding which peptide

to study with 2D-IR was important, as a distinct difference in the anharmonicity decay would be the most helpful. Comparing the series of simulations performed using the frozen AMBER method, the peptide that shows the largest difference in Cu-C-O angle change from TRIW-H is TRIW-$_{\delta M}$H. However, TRIW-$_{\delta M}$HL19A shows an improved nitrite reductase activity and still has a distinct difference in predicted angle change, so it was selected. Ultimately we would like to be able to link experimental observations, structural dynamics, and the computations to actual enzyme function, so it is sensible to investigate the peptide sequence that exhibits a pronounced change in function.

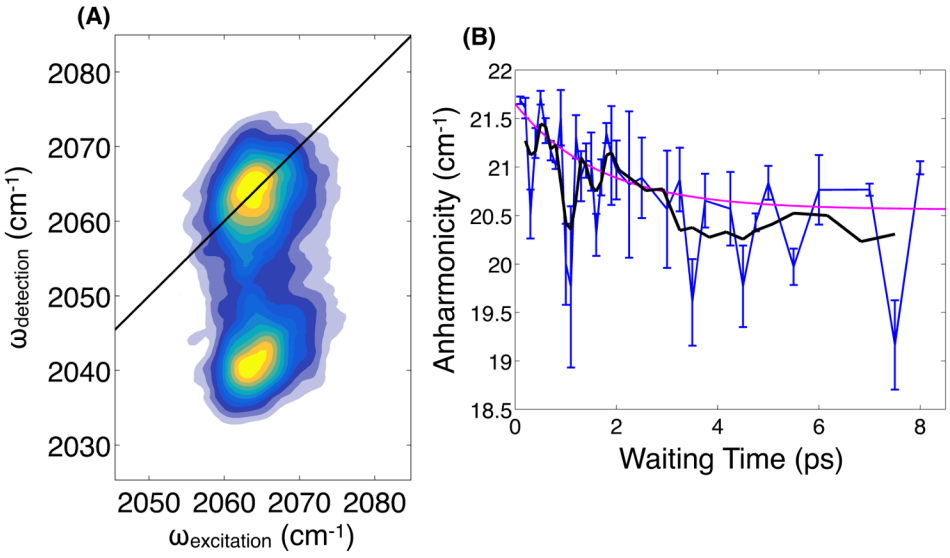

Figure 3.5 2D-IR results from [(TRIW-$_{\delta M}$HL19A)$_3$Cu(I)(CO)]$^+$ (A) Absolute value rephasing spectrum from a waiting time of 0.6 ps. The spectra looks similar to that obtained using TRIW-H. (B) Apparent anharmonicity decay fit to an offset exponential with a decay time of 1.5 ps and amplitude decay of 1.1 cm^{-1}. The decay is on the same timescale as TRIW-H, but with a smaller amplitude. The 3-point moving average is shown in black.

The 2D-IR absolute value rephasing spectrum of the TRIW-$_{\delta M}$HL19A copper carbonyl at a waiting time of 0.6 ps is shown in Figure 3.5A. The spectrum generally looks similar to that of TRIW-H studied previously, showing two well-resolved peaks separated by the anharmonicity of the CO stretching mode. Fitting slices along the detection axis to two Gaussian functions to estimate the anharmonicity for each spectrum yields the apparent anharmonicity as a function of waiting time (Figure 3.5B). The anharmonicity exponentially decays from 21.7 cm^{-1} to 20.6 cm^{-1} with a decay time

constant of 1.5 ps ± 1.7 ps. This decay has markedly smaller amplitude than the TRIW-H peptide from Chapter 2, and is entirely consistent with the predictions based on the QM/MM calculations described above. The similarity of relaxation time scale is consistent with the common origin of the low-frequency bending motion identified in the previous study with natural histidine and the leucine side chain.

Although the frequency shift dynamics of TRIW-$_{\delta M}$HL19A appear to have more noise than the TRIW-H decay previously reported, the uncertainty of each calculated anharmonicity value is about the same – ranging from about 0.2 to 1.0 cm^{-1}, as shown by the error bars. The smaller decay amplitude leads to an increased uncertainty in the error time, despite sampling the first 2 ps of waiting time more finely for TRIW-$_{\delta M}$HL19A (each waiting time was separated by 0.1 ps) than for TRIW-H (0.25 ps). A moving average was calculated with a three-point window, shown in Figure 3.5B in black. The averaged points show a decay from 21.4 cm^{-1} to 20.2 cm^{-1} with a decay time of 2.9 ± 3.0 ps. The decay time resolution is not improved by averaging the points, but the same decay amplitude is found. For future experiments, it would likely be beneficial to collect spectra at an even finer sampling rate or average multiple spectra collected at the same waiting time. It is straightforward to re-collect this data and will be done before publication of these results, but we are confident that the smaller anharmonicity change is significant.

3.4 Conclusions

Two series of copper carbonyl peptides were studied using an improved method of minimizing the structure prior to QM/MM calculations. In the first series, the location of both the histidine residues bonded to the copper atom and the carbonyl were moved to several different regions of the interior of the peptide. The only consistent change observed by relocating the active site is that the Cu-C-O angle changes less after excitation in all of the moved peptides than the original TRIW-H. The second series of peptides had modifications to the residues that bind copper or near the copper site. The peptide with the best nitrite reductase activity, TRIW-$_{\delta M}$HL19A, where the N_δ is

methylated and the leucine group above the metal site is replaced with a smaller alanine residue, was predicted to have one of the smallest Cu-C-O angle changes after being vibrationally excited. 2D-IR spectroscopy showed that the anharmonicity of the carbonyl mode decays on about the same time scale as TRIW-H, but the magnitude of the frequency shift is smaller than the original peptide, as predicted.

3.5 Acknowledgements

Karl Koebke synthesized the labeled peptide and prepared the samples.

3.6 References

1. Zastrow, M. L.; Peacock, A. F. A.; Stuckey, J. A.; Pecoraro, V. L., Hydrolytic catalysis and structural stabilization in a designed metalloprotein. *Nat. Chem.* **2012,** *4*, 118-123.

2. Zastrow, M. L.; Pecoraro, V. L., Influence of Active Site Location on Catalytic Activity in de Novo-Designed Zinc Metalloenzymes. *J. Am. Chem. Soc.* **2013,** *135*, 5895-5903.

3. Tegoni, M.; Yu, F. T.; Bersellini, M.; Penner-Hahn, J. E.; Pecoraro, V. L., Designing a functional type 2 copper center that has nitrite reductase activity within alpha-helical coiled coils. *Proc. Natl. Acad. Sci. U. S. A.* **2012,** *109*, 21234-21239.

4. Yu, F. T.; Penner-Hahn, J. E.; Pecoraro, V. L., De Novo-Designed Metallopeptides with Type 2 Copper Centers: Modulation of Reduction Potentials and Nitrite Reductase Activities. *J. Am. Chem. Soc.* **2013,** *135*, 18096-18107.

5. Der, B. S.; Edwards, D. R.; Kuhlman, B., Catalysis by a De Novo Zinc-Mediated Protein Interface: Implications for Natural Enzyme Evolution and Rational Enzyme Engineering. *Biochemistry* **2012,** *51*, 3933-3940.

6. Rufo, C. M.; Moroz, Y. S.; Moroz, O. V.; Stohr, J.; Smith, T. A.; Hu, X. Z.; DeGrado, W. F.; Korendovych, I. V., Short peptides self-assemble to produce catalytic amyloids. *Nat. Chem.* **2014,** *6*, 303-309.

7. Ross, M. R.; White, A. M.; Yu, F. T.; King, J. T.; Pecoraro, V. L.; Kubarych, K. J., Histidine Orientation Modulates the Structure and Dynamics of a de Novo Metalloenzyme Active Site. *J. Am. Chem. Soc.* **2015,** *137*, 10164-10176.

8. Rappe, A. K.; Casewit, C. J.; Colwell, K. S.; Goddard, W. A.; Skiff, W. M., UFF, a Full Periodic-Table Force-Field for Molecular Mechanics and Molecular-Dynamics Simulations. *J. Am. Chem. Soc.* **1992,** *114*, 10024-10035.

9. Izquierdo, R.; Rodriguez, L. J.; Anez, R.; Sierraalta, A., Direct catalytic decomposition of NO with Cu-ZSM-5: A DFT-ONIOM study. *Journal of Molecular Catalysis a-Chemical* **2011,** *348*, 55-62.

10. Rajapandian, V.; Hakkim, V.; Subramanian, V., ONIOM Calculation on Azurin: Effect of Metal Ion Substitutions. *J. Phys. Chem. A* **2009,** *113*, 8615-8625.

11. Garcia, J. I.; Jimenez-Oses, G.; Martinez-Merino, V.; Mayoral, J. A.; Pires, E.; Villalba, I., QM/MM modeling of enantioselective pybox-ruthenium- and box-copper-catalyzed cyclopropanation reactions: Scope, performance, and applications to ligand design. *Chemistry-a European Journal* **2007,** *13*, 4064-4073.

12. Cornell, W. D.; Cieplak, P.; Bayly, C. I.; Gould, I. R.; Merz, K. M.; Ferguson, D. M.; Spellmeyer, D. C.; Fox, T.; Caldwell, J. W.; Kollman, P. A., A Second Generation Force Field for the Simulation of Proteins, Nucleic Acids, and Organic Molecules. *J. Am. Chem. Soc.* **1995,** *117*, 5179-5197.

13. Kollman, P. A., Advances and continuing challenges in achieving realistic and predictive simulations of the properties of organic and biological molecules. *Acc. Chem. Res.* **1996,** *29*, 461-469.

14. Nechay, M. R.; Valdez, C. E.; Alexandrova, A. N., Computational Treatment of Metalloproteins. *J. Phys. Chem. B* **2015,** *119*, 5945-5956.

15. Seminario, J. M., Calculation of intramolecular force fields from second-derivative tensors. *Int. J. Quantum Chem.* **1996,** *60*, 1271-1277.

16. Wise, O.; Coskuner, O., New force field parameters for metalloproteins I: Divalent copper ion centers including three histidine residues and an oxygen-ligated amino acid residue. *J. Comput. Chem.* **2014,** *35*, 1278-1289.

17. Reyes, L. H.; Seminario, J. M., Determination of precise harmonic force constants for alanine polypeptides. *Journal of Molecular Structure-Theochem* **2007,** *818*, 125-129.

18. Peters, M. B.; Yang, Y.; Wang, B.; Fusti-Molnar, L.; Weaver, M. N.; Merz, K. M., Structural Survey of Zinc-Containing Proteins and Development of the Zinc AMBER Force Field (ZAFF). *J. Chem. Theory Comput.* **2010,** *6*, 2935-2947.

19. Tipmanee, V.; Blumberger, J., Kinetics of the Terminal Electron Transfer Step in Cytochrome c Oxidase. *J. Phys. Chem. B* **2012,** *116*, 1876-1883.

20. Wojcik, A.; Broclawik, E.; Siegbahn, P. E. M.; Borowski, T., Mechanism of Benzylic Hydroxylation by 4-Hydroxymandelate Synthase. A Computational Study. *Biochemistry* **2012,** *51*, 9570-9580.

21. Wesolowski, R. P.; Furmaniak, S.; Terzyk, A. P.; Gauden, P. A., Simulating the effect of carbon nanotube curvature on adsorption of polycyclic aromatic hydrocarbons. *Adsorption-Journal of the International Adsorption Society* **2011,** *17*, 1-4.

22. Malde, A. K.; Zuo, L.; Breeze, M.; Stroet, M.; Poger, D.; Nair, P. C.; Oostenbrink, C.; Mark, A. E., An Automated Force Field Topology Builder (ATB) and Repository: Version 1.0. *J. Chem. Theory Comput.* **2011,** *7*, 4026-4037.

23. Hu, L. H.; Ryde, U., Comparison of Methods to Obtain Force-Field Parameters for Metal Sites. *J. Chem. Theory Comput.* **2011,** *7*, 2452-2463.

24. Hess, B.; Kutzner, C.; van der Spoel, D.; Lindahl, E., GROMACS 4: Algorithms for highly efficient, load-balanced, and scalable molecular simulation. *J. Chem. Theory Comput.* **2008,** *4*, 435-447.

25. Nee, M. J.; McCanne, R.; Kubarych, K. J.; Joffre, M., Two-dimensional infrared spectroscopy detected by chirped pulse upconversion. *Opt. Lett.* **2007,** *32*, 713-5.

26. Nee, M. J.; Baiz, C. R.; Anna, J. M.; McCanne, R.; Kubarych, K. J., Multilevel vibrational coherence transfer and wavepacket dynamics probed with multidimensional IR spectroscopy. *J. Chem. Phys.* **2008,** *129*, 084503.

27. Baiz, C. R.; Mcrobbie, P. L.; Anna, J. M.; Geva, E.; Kubarych, K. J., Two-Dimensional Infrared Spectroscopy of Metal Carbonyls. *Acc. Chem. Res.* **2009,** *42*, 1395-1404.

28. Berendsen, H. J. C.; Grigera, J. R.; Straatsma, T. P., The Missing Term in Effective Pair Potentials. *J. Phys. Chem.* **1987,** *91*, 6269-6271.

29. Bayly, C. I.; Cieplak, P.; Cornell, W. D.; Kollman, P. A., A Well-Behaved Electrostatic Potential Based Method Using Charge Restraints for Deriving Atomic Charges - the Resp Model. *J. Phys. Chem.* **1993,** *97*, 10269-10280.

30. Case, D. A.; Darden, T. A.; III, T. E. C.; Simmerling, C. L.; Wang, J.; Duke, R. E.; Luo, R.; Walker, R. C.; Zhang, W.; Merz, K. M.; Roberts, B.; Hayik, S.; Roitberg, A.; Seabra, G.; Swails, J.; Goetz, A. W.; Kolossvary, I.; Wong, K. F.; Paesani, F.; Vanicek, J.; Wolf, R. M.; Liu, J.; Wu, X.; Brozell, S. R.; Steinbrecher, T.; Gohlke, H.; Cai, Q.; Ye, X.; Wang, J.; Hsieh, M.-J.; Cui, G.; Roe, D. R.; Mathews, D. H.; Seetin, M. G.; Ferrer, R. S.-.; Sagui, C.; Babin, V.; Luchko, T.; Gusarov, S.; Kovalenko, A.; Kollman, P. A. *AMBER 12*, University of California, San Francisco, 2012.

31. Frisch, M. J.; Trucks, G. W.; Schlegel, H. B.; Scuseria, G. E.; Robb, M. A.; Cheeseman, J. R.; Scalmani, G.; Barone, V.; Mennucci, B.; Petersson, G. A.; Nakatsuji, H.; Caricato, M.; Li, X.; Hratchian, H. P.; Izmaylov, A. F.; Bloino, J.; Zheng, G.; Sonnenberg, J. L.; Hada, M.; Ehara, M.; Toyota, K.; Fukuda, R.;

Hasegawa, J.; Ishida, M.; Nakajima, T.; Honda, Y.; Kitao, O.; Nakai, H.; Vreven, T.; Montgomery Jr., J. A.; Peralta, J. E.; Ogliaro, F.; Bearpark, M. J.; Heyd, J.; Brothers, E. N.; Kudin, K. N.; Staroverov, V. N.; Kobayashi, R.; Normand, J.; Raghavachari, K.; Rendell, A. P.; Burant, J. C.; Iyengar, S. S.; Tomasi, J.; Cossi, M.; Rega, N.; Millam, N. J.; Klene, M.; Knox, J. E.; Cross, J. B.; Bakken, V.; Adamo, C.; Jaramillo, J.; Gomperts, R.; Stratmann, R. E.; Yazyev, O.; Austin, A. J.; Cammi, R.; Pomelli, C.; Ochterski, J. W.; Martin, R. L.; Morokuma, K.; Zakrzewski, V. G.; Voth, G. A.; Salvador, P.; Dannenberg, J. J.; Dapprich, S.; Daniels, A. D.; Farkas, Ö.; Foresman, J. B.; Ortiz, J. V.; Cioslowski, J.; Fox, D. J. *Gaussian 09, Revision A.02*, Gaussian, Inc.: Wallingford, CT, USA, 2009.

32. Yu, F. De novo designed metallopeptides with a type 2 copper center: a structural and functional model for copper nitrite reductase. University of Michigan, 2014.

33. Lee, K. H.; Matzapetakis, M.; Mitra, S.; Neil, E.; Marsh, G.; Pecoraro, V. L., Control of metal coordination number in de novo designed peptides through subtle sequence modifications. *J. Am. Chem. Soc.* **2004,** *126*, 9178-9179.

34. Lee, K. H.; Cabello, C.; Hemmingsen, L.; Marsh, E. N. G.; Pecoraro, V. L., Using nonnatural amino acids to control metal-coordination number in three-stranded coiled coils. *Angewandte Chemie-International Edition* **2006,** *45*, 2864-2868.

Chapter 4

Influence of the Hofmeister Effect on a Confined Probe

4.1 Introduction

The Hofmeister series is a ranking of ions based on their ability to increase or decrease the solubility of proteins in aqueous solution.[1-3] Despite the great interest in the series and large amount of investigation into these ions, the exact origin of the Hofmeister effect is unknown. The traditional explanation is that kosmotropes strengthen hydrophobic interactions in the protein and increase their folded stability, reducing their solubility, while chaotropes reduce hydrophobic interactions, increasing the solubility of the macromolecule. It was originally thought that the ions modified the hydrogen-bonding network of water surrounding the protein, making kosmotropes water so-called "structure makers" and chaotropes water "structure breakers". The effect these salts have on the structure of water throughout solution has been disputed by recent spectroscopic investigations that show the salts have little influence beyond the first or second solvation shell and no effect on bulk water.[2, 4-6] Cho et al. have recently discovered that the different extrema of the Hofmeister series aggregate differently at high concentrations – the kosmotropes form crystal-like clusters while chaotropes tend to form a network of ions intertwined with the water.[7-10]

The formation of ionic networks or clusters is only noticeable at high concentrations – the lowest studied by Cho et al. was 0.92 M, but the disruption of the hydrogen-bonding network may be present at lower concentrations.[7] One way to explore this formation of ionic aggregates would be to monitor the ultrafast dynamics of a vibrational probe in the aqueous solution, where the change in the water's hydrogen-bonding could be detected by a change in the spectral diffusion of the probe. This vibrational probe could be a labeled side-chain of a protein, where differences between

bulk and interfacial water have been observed previously,[11] or one of the Hofmeister series ions itself. The thiocyanate anion is an excellent choice for the probe because a number of salts with other Hofmeister series cations are readily available, allowing us to detect how the water surrounding the thiocyanate changes when a different cation is used. The Hofmeister effect is generally stronger for anions than cations, but there should still be a noticeable trend, especially if comparing strong chaotropes and strong kosmotropes. The general Hofmeister series for cations is $NH_4^+ > K^+ > Na^+ > Li^+ > Mg^{2+} > Ca^{2+}$ with ammonium the strongest kosmotrope and calcium the strongest chaotrope.[12, 13]

Another advantage of using the thiocyanate ion as a probe of the ultrafast water dynamics is that it will form a complex with hydrophobic cavities in aqueous solution, such as a cyclodextrin or a curved amphiphile.[14] More chaotropic anions bind more strongly to these concave structures, increasing their solubility, exactly as would be predicted for proteins.[14] Cyclodextrins are cyclically connected glucose residues that form a tube or barrel-like shape that can promote host-guest complexes with small molecules or ions giving them a wide variety of applications from drug delivery to household cleaning products.[15, 16] The smallest of these, α-cyclodextrin (α-CD) which is composed of six glucose units with a hydrophobic cavity with a diameter of about 5 Å and a depth of about 7 Å. The cavity is comparable in size to the thiocyanate anion and only one ion would be expected to bind to the cavity at a time, as shown in Figure 4.1.[17] The thiocyanate/α-CD complex has a cation-dependent binding, but is highest for NaSCN with a value of 27 M^{-1}, meaning that in a 50 mM mixture of sodium thiocyanate and α-CD, roughly 43% of the thiocyanate anions will be complexed with the cyclodextrin.[17]

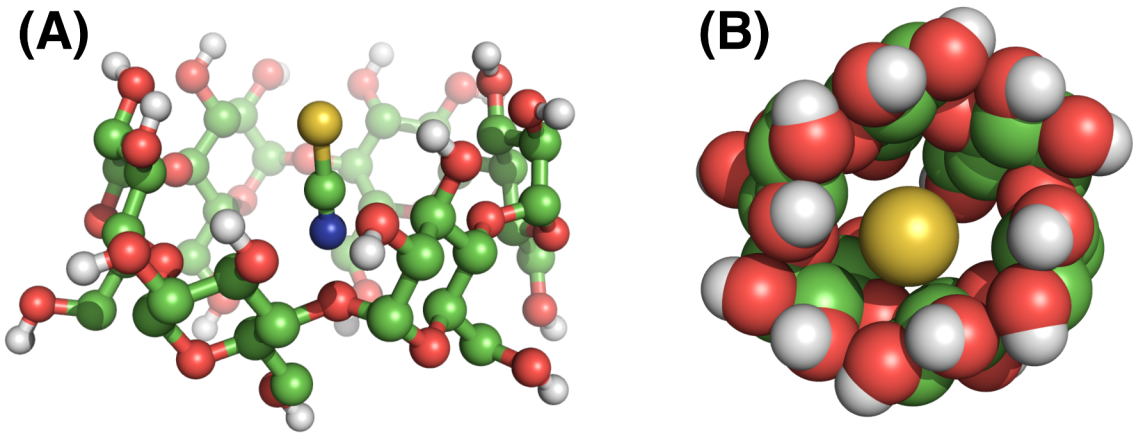

Figure 4.1 Complex formed between thiocyanate anion and α-cyclodextrin. (*A*) Shows the length of SCN relative to the depth of the cyclodextrin cavity using the ball-and-stick representation. (*B*) The same structure, but with space-filling model from the top to show most of the cavity is filled by the thiocyanate. 2D-IR data seems to show that the CN bond is shielded from the solvent, as shown.

Using α-cyclodextrin to bind a vibrational probe in a known location could provide insight into the Hofmeister effect. If the chaotropic thiocyanate salts form an ionic network and the kosmotropic salts form ionic clusters, the cyclodextrin could interrupt the formation of these ionic aggregates even at low concentrations. Cyclodextrins are open at both ends, meaning the ionic networks could continue to form even at high cyclodextrin concentration by chaining the cyclodextrins together similar to how polyethylene glycol and other polymers have been observed in cyclodextrins.[18-21] Due to the restraints of the cavity size, any thiocyanate confined to the cyclodextrin would be unable to join an ionic cluster, disrupting the structure that forms in the absence of cyclodextrin.

4.2 Methods

4.2.1 Materials

All thiocyanate salts were purchased from Sigma-Aldrich and used without further purification. α-cyclodextrin was purchased from TCI and also used without further purification. D_2O was purchased from Merk.

4.2.2 Sample Preparation

All solutions were prepared with 50 mM thiocyanate salt in D_2O, except for $Ca(SCN)_2$ solutions, which were 25 mM to keep the thiocyanate ion concentration constant. Any α-cyclodextrin solutions were also 50 mM so that a 1:1 mixture of α-cyclodextrin and thiocyanate was present. The concentrations for LiSCN and NBu_4SCN may not be exactly 50 mM because LiSCN forms a hydride without a fixed number of water molecules, making it difficult to accurately measure solely based on weight while NBu_4SCN partially phase-separates from water. To make up for this, solutions were diluted or had additional salt added until the FTIR spectra had a similar SCN stretching band (near 2060 cm^{-1}) intensity as 50 mM NaSCN. The 250 µL samples were placed in a sample cell consisting of two 25 mm x 3 mm calcium fluoride windows separated by a 100 µm Teflon spacer.

4.2.3 2D-IR Details

The 2D-IR experimental setup has been described elsewhere previously.[22-24] Spectra of solutions with only thiocyanate salts were collected with waiting times ranging from -0.2 to 5.0 ps in steps of 0.1 ps, 5.25 ps to 10.0 ps in steps of 0.25 ps, and 10.5 to 15.0 ps in steps of 0.5 ps. Spectra of solutions containing α-cyclodextrin were collected with waiting times of -0.2 to 5.0 ps in steps of 0.1 ps, 5.25 to 8.0 ps in steps of 0.25 ps, 8.5 to 12.0 ps in steps of 0.5 ps, and 13 to 30 ps in 1 ps steps to account for the longer frequency fluctuation correlation function (FFCF) decay time. The FFCF was calculated using the inhomogeneity index method:[25]

$$C(t) = \sin\left[\frac{\pi}{2}\left(\frac{A_R - A_{NR}}{A_R + A_{NR}}\right)\right]$$

where A_R and A_{NR} are the moduli of the rephasing and nonrephasing signals, respectively, integrated over the spectral range of interest at each waiting time. The resulting points are fit to an offset exponential or biexponential decay to extract the spectral diffusion timescale. The offsets are adjusted so that the correlation function of sodium thiocyanate in D_2O decays to a value of zero.

4.3 Results and Discussion

4.3.1 FTIR Results

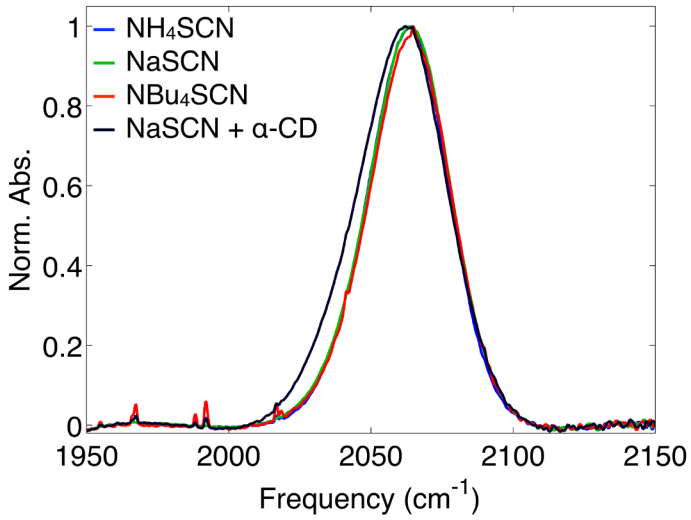

Figure 4.2 Normalized FTIR spectra of the CN stretching mode of three different thiocyanate salts, showing they are all identical. Adding α-cyclodextrin to NaSCN (shown in black) causes the central frequency to redshift from 2064 cm^{-1} to about 2060 cm^{-1} while the width of the band increases.

The Fourier Transform Infrared (FTIR) spectra of all of the thiocyanate salts are very similar, as seen in Figure 4.2. The spectra shown are normalized to the highest absorbance (near 2060 cm^{-1}) to clearly illustrate the similarities in the lineshapes. The addition of α-cyclodextrin causes a noticeable redshift in the frequency, from 2064 cm^{-1} to 2060 cm^{-1}, through a broadening of the peak, as shown in Figure 4.2. However, since the blue edge of the band is unaffected, the spectrum is most likely not simply shifted, but instead a new species is favored. This increased amplitude at lower frequencies is likely due to a decrease in the amount of hydrogen bonding,[26, 27] which is largely expected to occur on the nitrogen atom of the thiocyanate ion.[26, 28] The decrease in hydrogen bonding could be due to either the nitrogen atom being separated from the solvent in the middle of the hydrophobic cyclodextrin or due to the decreased surface area of the complex. It should be noted that all thiocyanate salts studied – NH_4SCN, KSCN, NaSCN, LiSCN, $Ca(SCN)_2$, and NBu_4SCN all showed similar shifts with the addition of α-cyclodextrin.

4.3.2 2D-IR Shows Slightly Cation-Dependent Dynamics: Insight into Binding

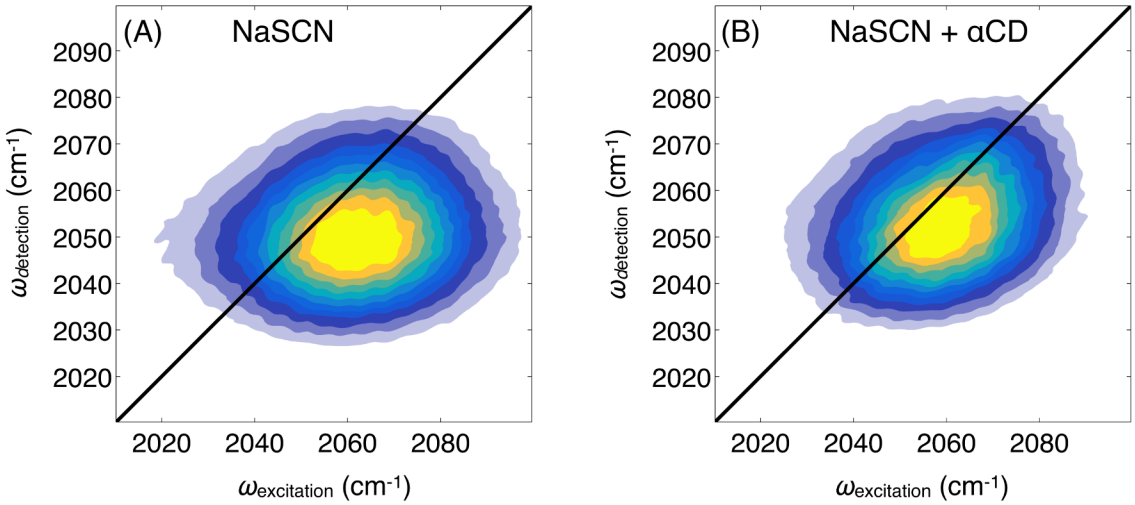

Figure 4.3 Absolute value 2D-IR rephasing spectra of NaSCN (*A*) and NaSCN with α-cyclodextrin (*B*) at a waiting time of 0.5 ps. The spectrum with cyclodextrin has a more narrow homogeneous linewidth due to the increased time to sample available environments.

The 2D-IR spectra of the thiocyanate salts also look similar to each other. The absolute-value rephasing spectrum of sodium thiocyanate shown in Figure 4.3 is representative of all of the salts studied, where the spectrum is already quite homogeneously broadened, indicating the frequencies are interchanging quickly due to the low barrier between environments. The addition of α-cyclodextrin causes an increase in the inhomogeneous broadening because of the added environmental complexity – primarily bound in the cyclodextrin – that cannot be sampled in the 500 fs between excitation and detection for the given spectrum. This is more clearly seen in the FFCFs, shown in Figure 4.4 where the correlation function decays more slowly for sodium thiocyanate with α-cyclodextrin than without.

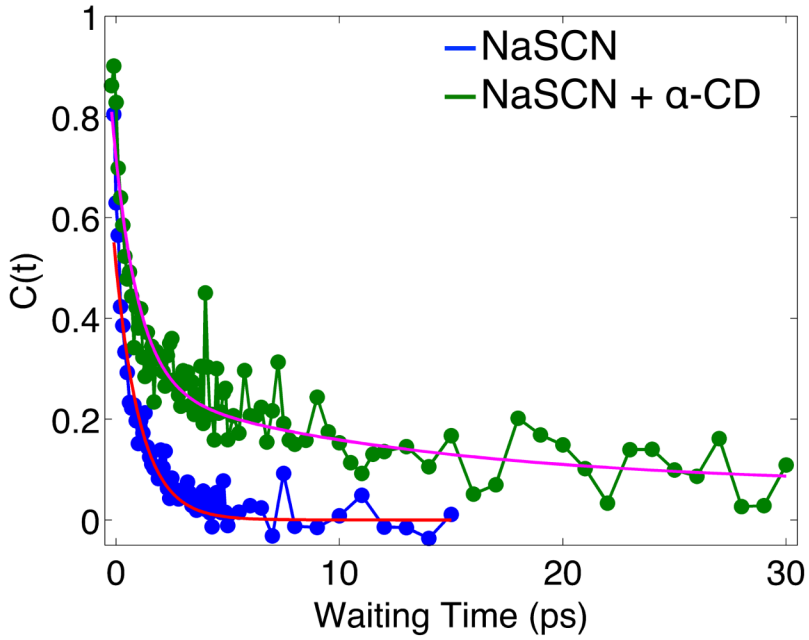

Figure 4.4 FFCF of NaSCN in D_2O (blue dots) fit to an exponential decay (red line) and NaSCN with α-cyclodextrin (green dots) fit to an offset biexponential decay (magenta line) with the faster decay constant fixed at the same value as NaSCN. The thiocyanate

From the FFCFs shown in Figure 4.4 it is clear that the addition of α-cyclodextrin slows the decay of the correlation function, but the fast decay time seen in the absence of thiocyanate is still present. The presence of the fast decay is likely due to not all of the thiocyanate forming a complex with the cyclodextrin, as only 43% of the thiocyanate anions are expected to be bound,[17] leaving a comparable number of the thiocyanate ions in solution unchanged from the cyclodextrin-free solution unless some kind of ionic aggregation occurs. To account for this mixture of bound and unbound thiocyanate ions, the FFCF of the solution containing both a thiocyanate salt and α-cyclodextrin was fit to an offset biexponential decay, where the faster decay time (around 1 ps) was fixed at the same value found in the solution without cyclodextrin. The offsets of the FFCFs studied were adjusted so that the NaSCN in D_2O correlation function decayed to zero. NaSCN had the lowest offset of all the thiocyanate salts, but the others decayed to a value within 0.02, so the choice of NaSCN does not appear to be significant and any other thiocyanate could also have been used.

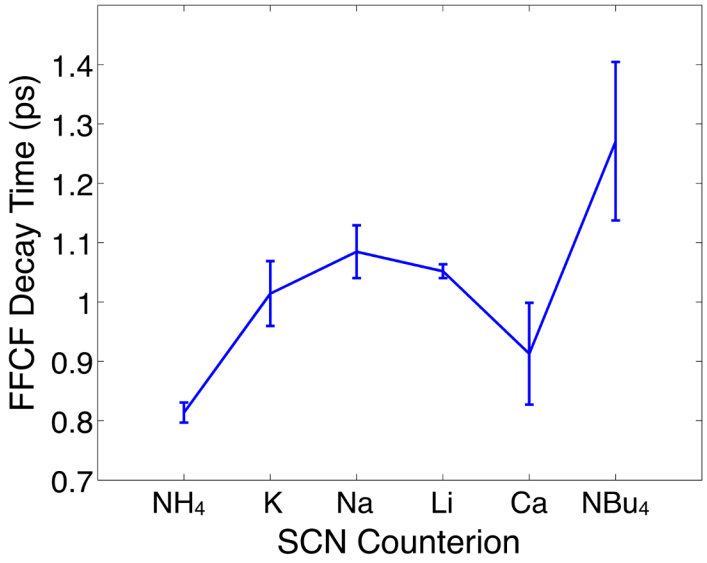

Figure 4.5 The FFCF decay time of the thiocyanate CN stretching mode is dependent on the cation where kosmotropes show the fastest dynamics and chaotropes the slowest. Error bars are the 95% confidence interval from an offset exponential decay.

The easily noticeable trend in the FFCFs of thiocyanate salts in D_2O (without α-cyclodextrin) is that the decay time is generally longer for chaotropes, with the exception being $Ca(SCN)_2$, as shown in Figure 4.5. This may be because the amount of calcium ions present in solution is half that of the other cations because it was the only cation studied with a +2 charge, so for every calcium ion added two thiocyanate ions were introduced to the solution. It would be possible to add a different calcium salt to increase the cation concentration, but that would also introduce another anion, which could interact with the water structure near the thiocyanate anion differently, altering the FFCF. So discounting $Ca(SCN)_2$ for now, it appears that the kosmotropic cations cause the thiocyanate to sample its environments more quickly, which could be due to the water reorienting faster in the presence of the kosmotropes and slower in the presence of chaotropes. This trend had been observed previously in the dielectric relaxation of water molecules in the presence of 1 M salt solutions, where water reorients more quickly in the presence of ammonium and potassium, but more slowly with sodium and the other cations, especially tetrabutylammonium.[29-31] It is interesting to note that Kaatze also noticed a faster reorientation time for divalent cations, such as Ca^{2+}, but did not have a full understanding of why that would be.[31, 32]

The order of the cations in Figure 4.5 is generally agreed upon for NH_4^+ through Ca^{2+}, but the placement of NBu_4^+ is less certain. Most rankings only compare the alkali and alkaline earth cations with several other common cations, such as ammonium and guanadiumium.[1, 12, 33-35] However, few studies have compared tetraalkylammonium salts to these standard cations. The few that have looked at these cations, have generally placed tetrabutylammonium among the most chaotropic of the ions, so it seems reasonable to place it on the far chaotropic end of the spectrum.[13, 36]

Table 4.1 Fit parameters from the FFCF of thiocyanate salts with α-cyclodextrin in D_2O. All the correlation functions were fit to an offset biexponential with the fast decay time fixed at the value obtained from fitting the FFCF of just the thiocyanate salt in D_2O. The third column is the ratio of the amplitude of the slow decay to the fast decay to see if a binding constant could be extracted from the FFCF.

Thiocyanate Salt (with α-cyclodextrin)	Slow FFCF Decay (ps)	Offset	Slow/Fast Amp. Ratio
NH_4SCN	12.75 ± 4.51	0.056 ± 0.033	0.798 ± 0.143
KSCN	5.26 ± 0.64	0.140 ± 0.004	0.881 ± 0.122
NaSCN	13.13 ± 6.89	0.067 ± 0.036	0.432 ± 0.078
LiSCN	5.70 ± 0.49	0.102 ± 0.002	0.438 ± 0.030
$Ca(SCN)_2$	13.24 ± 1.19	-0.010 ± 0.012	1.658 ± 0.133
NBu_4SCN	11.31 ± 1.68	0.103 ± 0.011	1.036 ± 0.106

It does not appear that there are any clear trends from the FFCFs of solutions containing both a thiocyanate salt and α-cyclodextrin, as seen by the offset biexponential fit parameters listed in Table 4.1. The addition of 50 mM α-cyclodextrin increases the amount of scatter in the 2D-IR signal, making it difficult to obtain clear spectra and thus reducing the confidence in the fits of the resulting correlation functions. In the case of KSCN and LiSCN, the slower part of the FFCF decays relatively quickly (~5 ps), resulting in a well-defined offset with a 95% confidence range of <0.01. In cases where the decay time is less resolved, the offset also has a larger amount of error, such as in ammonium thiocyanate and sodium thiocyanate, where the uncertainty of the slow decay is several picoseconds and the offset uncertainty is the highest of the thiocyanate salts. $Ca(SCN)_2$ is an outlier here as well, with the slow decay being the

longest of any observed, but with an uncertainty of 1.2 ps and an offset of essentially zero. Previous 2D-IR studies[37, 38] on concentrated divalent cations in solution with thiocyanate have shown that another ion $MNCS^+$ (where M^{2+} is the divalent cation) forms at higher concentrations of the cation. While it is unlikely that this ion is forming at low concentrations, as the frequency of this ion is higher than thiocyanate, it is possible that the calcium ion remains closer to the thiocyanate than other cations. This may displace water molecules that would normally slow the anion's entrance and exit from the cyclodextrin cavity, so that this environment sampling now occurs within the 30 ps window studied, removing the offset seen in other cations, although it seems unlikely that the calcium ion would remain in such close proximity to the thiocyanate.

The ratio of the slow decay amplitude to the fast decay amplitude from the biexponential FFCF was calculated to try to estimate how many thiocyanate ions were confined to the cyclodextrin (giving the slow decay) or free in solution (fast decay). The results are shown in Table 4.1, but there is no clear trend present. For two known[17] binding constants, NaSCN (27.1 M^{-1}) and KSCN (21.2 M^{-1}), the expected ratios of bound to unbound thiocyanate are 0.767 and 0.645, respectively, neither of which is close to the measured values of 0.432 and 0.881. This error is likely due to the amount of noise in the FFCF but could also arise from the unknown weighting of the different contributions to the FFCF.

One takeaway from the 2D-IR data of solutions with α-cyclodextrin is that the FFCF decay time attributed to the thiocyanate confined to the cavity of the cyclodextrin is longer than that of the free thiocyanate ion. This seems straightforward, as it will take more time for the thiocyanate to move to a different environment and for water to make or break hydrogen bonds in this constrained environment. However, the solven-accessible surface area of the probe is also reduced which has been previously[39] been seen as a reason for spectral diffusion to occur more quickly. Because the decay time is slower, the nitrogen of the thiocyanate ion is likely not exposed to the solvent, as the carbonyl groups were in the cyclopentadienyl chromium tricarbonyl with β-cyclodextrin.

This implies that the thiocyanate is bound to the α-cyclodextrin as shown in Figure 4.1, with the sulfur solven-exposed and the nitrogen in the cavity.

4.4 Conclusions

A series of thiocyanate salts were studied in neat D_2O as well as in complex with α-cyclodextrin. The initial goal was to identify a trend in the ultrafast dynamics of the thiocyanate ion using 2D-IR spectroscopy, but the FFCFs from solutions containing both the thiocyanate and cyclodextrin were too noisy to discern a meaningful trend. For the solutions containing only thiocyanate, the dynamics reported by the thiocyanate CN stretching mode were faster in the presence of more kosmotropic ions, such as NH_4^+ and K^+ and slower in the presence of more chaotropic ions like NBu_4^+. A similar trend was previously reported using dielectric relaxation spectroscopy to study the water in concentrated salt solutions.[29-32] The 2D-IR results suggest that the thiocyanate anion binds to the cyclodextrin cavity with the nitrogen pointing inwards, leaving the sulfur atom solvent-exposed. This was determined from the spectral diffusion timescale, which is longer for the complexed thiocyanate, as opposed to another vibrational probe-cyclodextrin complex[39] where the solvent-exposed probe had a faster spectral diffusion time than in bulk solvent.

This system could still provide insights into the Hofmeister effect, especially if the insights by Cho et al. regarding ionic networks and clusters are indeed linked to the effect.[7-10] It is uncertain if trends will be observable at the concentration levels used in these experiments, as most of the other investigations into the Hofmeister series have been closer to 1 M than the 50 mM used here. In fact, some studies with low salt concentration (~300 mM) have seen an "inverse Hofmeister series" where the trend seen is the opposite of the trend at higher concentrations.[40, 41] One way to use higher concentrations of salt while using the same concentration of probe would be to use a different salt with the same cation, but an anion that does not have a vibrational mode close in frequency to thiocyanate, such as chloride. That way, the concentration could be increased and since Cl^- is not extremely chaotropic or kosmotropic, it likely would

have less of an influence on the ionic aggregation. Then the thiocyanate anions could still participate in the aggregation and report on the dynamics, even at relatively low concentrations.

4.5 References

1. Kunz, W.; Henle, J.; Ninham, B. W., 'Zur Lehre von der Wirkung der Salze' (about the science of the effect of salts): Franz Hofmeister's historical papers. *Curr. Opin. Colloid Interface Sci.* **2004,** *9*, 19-37.

2. Zhang, Y. J.; Cremer, P. S., Interactions between macromolecules and ions: the Hofmeister series. *Curr. Opin. Chem. Biol.* **2006,** *10*, 658-663.

3. Hofmeister, F., Zur Lehre von der Wirkung der Salze (About the science of the effect of salts). *Arch. Exp. Pathol. Pharmakol.* **1888,** *24*, 247-260.

4. Omta, A. W.; Kropman, M. F.; Woutersen, S.; Bakker, H. J., Negligible effect of ions on the hydrogen-bond structure in liquid water. *Science* **2003,** *301*, 347-349.

5. Kropman, M. F.; Bakker, H. J., Effect of ions on the vibrational relaxation of liquid water. *J. Am. Chem. Soc.* **2004,** *126*, 9135-9141.

6. Kropman, M. F.; Bakker, H. J., Vibrational relaxation of liquid water in ionic solvation shells. *Chem. Phys. Lett.* **2003,** *370*, 741-746.

7. Kim, S.; Kim, H.; Choi, J. H.; Cho, M., Ion aggregation in high salt solutions: Ion network versus ion cluster. *J. Chem. Phys.* **2014,** *141*.

8. Choi, J. H.; Cho, M., Ion aggregation in high salt solutions. II. Spectral graph analysis of water hydrogen-bonding network and ion aggregate structures. *J. Chem. Phys.* **2014,** *141*.

9. Choi, J. H.; Kim, H.; Kim, S.; Lim, S.; Chon, B.; Cho, M., Ion aggregation in high salt solutions. III. Computational vibrational spectroscopy of HDO in aqueous salt solutions. *J. Chem. Phys.* **2015,** *142*.

10. Choi, J. H.; Cho, M., Ion aggregation in high salt solutions. IV. Graph-theoretical analyses of ion aggregate structure and water hydrogen bonding network. *J. Chem. Phys.* **2015,** *143*.

11. King, J. T.; Arthur, E. J.; Brooks, C. L.; Kubarych, K. J., Site-Specific Hydration Dynamics of Globular Proteins and the Role of Constrained Water in Solvent Exchange with Amphiphilic Cosolvents. *J. Phys. Chem. B* **2012,** *116*, 5604-5611.

12. Nihonyanagi, S.; Yamaguchi, S.; Tahara, T., Counterion Effect on Interfacial Water at Charged Interfaces and Its Relevance to the Hofmeister Series. *J. Am. Chem. Soc.* **2014,** *136*, 6155-6158.

13. VonHippel, P. H.; Wong, K. Y., Neutral Salts - Generality of Their Effects on Stability of Macromolecular Conformations. *Science* **1964,** *145*, 577-580.

14. Gibb, C. L. D.; Gibb, B. C., Anion Binding to Hydrophobic Concavity Is Central to the Salting-in Effects of Hofmeister Chaotropes. *J. Am. Chem. Soc.* **2011,** *133*, 7344-7347.

15. Szejtli, J., Introduction and general overview of cyclodextrin chemistry. *Chem. Rev.* **1998,** *98*, 1743-1753.

16. Goschl, M.; Crouzy, S.; Chapron, Y., Molecular dynamics study of an α-cyclodextrin-phosphatidylinositol inclusion complex. *European Biophysics Journal with Biophysics Letters* **1996,** *24*, 300-310.

17. Spencer, J. N.; He, Q.; Ke, X. M.; Wu, Z. Q.; Fetter, E., Complexation of inorganic anions and small organic molecules with alpha-cyclodextrin in water. *J. Solution Chem.* **1998,** *27*, 1009-1019.

18. Udachin, K. A.; Wilson, L. D.; Ripmeester, J. A., Solid polyrotaxanes of polyethylene glycol and cyclodextrins: The single crystal X-ray structure of PEG-beta-cyclodextrin. *J. Am. Chem. Soc.* **2000,** *122*, 12375-12376.

19. Lo Nostro, P.; Lopes, J. R.; Cardelli, C., Formation of cyclodextrin-based polypseudorotaxanes: Solvent effect and kinetic study. *Langmuir* **2001,** *17*, 4610-4615.

20. Harada, A.; Kamachi, M., Complex-Formation between Poly(Ethylene Glycol) and Alpha-Cyclodextrin. *Macromolecules* **1990,** *23*, 2821-2823.

21. Harada, A.; Takashima, Y.; Yamaguchi, H., Cyclodextrin-based supramolecular polymers. *Chem. Soc. Rev.* **2009,** *38*, 875-882.

22. Nee, M. J.; McCanne, R.; Kubarych, K. J.; Joffre, M., Two-dimensional infrared spectroscopy detected by chirped pulse upconversion. *Opt. Lett.* **2007,** *32*, 713-5.

23. Nee, M. J.; Baiz, C. R.; Anna, J. M.; McCanne, R.; Kubarych, K. J., Multilevel vibrational coherence transfer and wavepacket dynamics probed with multidimensional IR spectroscopy. *J. Chem. Phys.* **2008,** *129*, 084503.

24. Baiz, C. R.; Mcrobbie, P. L.; Anna, J. M.; Geva, E.; Kubarych, K. J., Two-Dimensional Infrared Spectroscopy of Metal Carbonyls. *Acc. Chem. Res.* **2009,** *42*, 1395-1404.

25. Roberts, S.; Loparo, J.; Tokmakoff, A., Characterization of spectral diffusion from two-dimensional line shapes. *J. Chem. Phys.* **2006,** *125*, 084502.

26. Schultz, P. W.; Leroi, G. E.; Popov, A. I., Solvation of SCN- and SeCN- anions in hydrogen-bonding solvents. *J. Am. Chem. Soc.* **1996,** *118*, 10617-10625.

27. Bacelon, P.; Corset, J.; Deloze, C., Anion Solvation .2. Solvation of Thiocyanate and Halide Anions in Mixtures of Protic and Aprotic-Solvents. *J. Solution Chem.* **1983,** *12*, 13-22.

28. Li, M.; Owrutsky, J.; Sarisky, M.; Culver, J. P.; Yodh, A.; Hochstrasser, R. M., Vibrational and Rotational Relaxation-Times of Solvated Molecular-Ions. *J. Chem. Phys.* **1993,** *98*, 5499-5507.

29. Giese, K.; Kaatze, U.; Pottel, R., Permittivity and Dielectric and Proton Magnetic Relaxation of Aqueous Solutions of Alkali Halides. *J. Phys. Chem.* **1970,** *74*, 3718-3725.

30. Wen, W. Y.; Kaatze, U., Aqueous-Solutions of Azoniaspiroalkane Halides .3. Dielectric-Relaxation. *J. Phys. Chem.* **1977,** *81*, 177-181.

31. Marcus, Y., Effect of Ions on the Structure of Water: Structure Making and Breaking. *Chem. Rev.* **2009,** *109*, 1346-1370.

32. Kaatze, U., Dielectric Effects in Aqueous-Solutions of 1-1, 2-1, and 3-1 Valent Electrolytes - Kinetic Depolarization, Saturation, and Solvent Relaxation. *Zeitschrift Fur Physikalische Chemie-Wiesbaden* **1983,** *135*, 51-75.

33. Nucci, N. V.; Vanderkooi, J. M., Effects of salts of the Hofmeister series on the hydrogen bond network of water. *J. Mol. Liq.* **2008,** *143*, 160-170.

34. Holm, R.; Schonbeck, C.; Somprasirt, P.; Westh, P.; Mu, H. L., A study of salt effects on the complexation between beta-cyclodextrins and bile salts based on the Hofmeister series. *J. Inclusion Phenom. Macrocyclic Chem.* **2014,** *80*, 243-251.

35. Yang, Z., Hofmeister effects: an explanation for the impact of ionic liquids on biocatalysis. *J. Biotechnol.* **2009,** *144*, 12-22.

36. Constantinescu, D.; Weingartner, H.; Herrmann, C., Protein denaturation by ionic liquids and the Hofmeister series: A case study of aqueous solutions of ribonuclease A. *Angewandte Chemie-International Edition* **2007,** *46*, 8887-8889.

37. Sun, Z.; Zhang, W. K.; Ji, M. B.; Hartsock, R.; Gaffney, K. J., Contact Ion Pair Formation between Hard Acids and Soft Bases in Aqueous Solutions Observed with 2DIR Spectroscopy. *J. Phys. Chem. B* **2013,** *117*, 15306-15312.

38. Park, S.; Ji, M. B.; Gaffney, K. J., Ligand Exchange Dynamics in Aqueous Solution Studied with 2DIR Spectroscopy. *J. Phys. Chem. B* **2010,** *114*, 6693-6702.

39. Osborne, D. G.; King, J. T.; Dunbar, J. A.; White, A. M.; Kubarych, K. J., Ultrafast 2DIR Probe of a Host-Guest Inclusion Complex: Structural and Dynamical Constraints of Nanoconfinement. *J. Chem. Phys.* **2013,** *138*, 144501.

40. Zhang, Y. J.; Cremer, P. S., The inverse and direct Hofmeister series for lysozyme. *Proc. Natl. Acad. Sci. U. S. A.* **2009,** *106*, 15249-15253.

41. Bostrom, M.; Tavares, F. W.; Finet, S.; Skouri-Panet, F.; Tardieu, A.; Ninham, B. W., Why forces between proteins follow different Hofmeister series for pH above and below pI. *Biophys. Chem.* **2005,** *117*, 217-224.

Chapter 5

Structural Impact of a Contact Ion Pair on a Functionalized Crown Ether

5.1 Introduction

Investigating a system with charged species and a vibrational probe can be complicated due to the large amount of unknown information about how the charges are arranged, as shown in the preceding chapters. In the case of the peptide, the motion of charged side chains and the electric field from the α-helical dipole alignment create an electrostatic environment that is difficult to model. When using an anion in aqueous solution as the vibrational probe, as done with the thiocyanate with cyclodextrin experiments, the anion and cation are separately solvated, so the relative distance of the two varies, complicating the analysis of the electrostatics. Another situation, where the anion and cation are always a knowable distance from the probe could ease the interpretation of the results.

One well-studied system that has a vibrational probe where the ions of a salt are a knowable distance from each other is sodium thiocyanate in tetrahydrofuran (THF), where the sodium cation and thiocyanate anion essentially only form contact ion pairs, even at low concentrations.[1-4] The THF is not polar enough to overcome the attractive force between the two ions and solvate them separately, leading to contact ion pairs and even dimers at higher concentrations, as determined by infrared and ultrasonic spectroscopy.[1] The contact ion pairs and the dimer have different thiocyanate CN stretching frequencies, so they can be studied separately using 2D-IR, meaning the dynamics of the two environments can be monitored individually, as well as potentially seeing energy transfer or coupling between the two if it is present. Energy transfer between different clusters of thiocyanate salts has been investigated previously,[5, 6] but

at very high concentrations in aqueous solutions, to estimate the size of the ionic clusters.[7]

Another system that has been studied involving alkali metal salts in THF is the complex formed between crown ethers and the cation from the salt.[8-10] Specifically, the crown ethers 15-crown-5 and 18-crown-6 show a great affinity for sodium and potassium ions in many different solvents, with the oxygen atoms in the ether coordinating to the cation. The binding constant of Na^+ to each of these crown ethers has been determined to be at least 10^4 M^{-1} in THF.[11] The binding constant was measured more accurately in methanol, where the 15-crown-5 has a slightly lower binging constant (log *K* = 3.24) compared to the 18-crown-6 (log *K* = 4.35), with both cases indicating that the vast majority of the cations in solution will be complexed with the crown ether.[12] This affinity allows crown ethers, especially when attached to a reporting molecule of some kind, to act as detectors of cations in solution and has made them popular molecules to modify with different labels.[13-15]

One example of a crown ether detector is (η^6-benzocrown ether)$Cr(CO)_3$, where the reporting group is the metal carbonyl that is connected to the crown ether by a linking aromatic group. Benzocrown ethers have similar cation binding constants as unsubstituted crown ethers,[11] but allow the change in electron density from coordinating the cation to be extended to the metal carbonyl system which results in a blueshifting of the carbonyl stretching modes.[16] This is because the loss in electron density on the crown ether oxygen atoms also withdraws electron density from the carbonyl π^* orbitals, causing the bonds to shorten and the frequencies to blueshift. The chromium tricarbonyl system is useful because the carbonyl stretching frequencies are located in a fairly uncrowded part of the infrared spectrum and absorb strongly, so they can be detected even at low concentrations (on the order of mM) and the carbonyl frequencies will shift with a similar cation concentration because of the high bonding constant.

By combining the two systems – sodium thiocyanate contact ion pairs in THF and cation-coordinating benzocrown ether chromium tricarbonyl, the sodium ion from

sodium thiocyanate is expected to coordinate with the crown ether and because the solvent is THF, the thiocyanate anion is expected to remain in contact, giving two vibrational probes in close spatial and spectral proximity. This could potentially lead to coupling of the thiocyanate CN stretching and the symmetric CO stretching mode, which have frequencies around 2060 and 1960 cm^{-1}, respectively.

5.2 Methods

5.2.1 Materials

Tetrahydrofuran (THF) and sodium thiocyanate were purchased from Sigma-Aldrich and used without further purification. The THF used contained 250 ppm butylated hydroxytoluene (BHT) to inhibit peroxide formation. Sodium tetraphenylborate was purchased from Alfa Aesar and was also used without further purification.

5.2.2 Synthesis of Benzocrown Ether Chromium Tricarbonyl

Benzo-18-Crown-6 Ether Chromium Tricarbonyl (BCECT) was synthesized using the method established by Mahaffey and Pauson.[17] A solution of 937 mg benzo-18-crown-6 and 662 mg chromium hexacarbonyl was prepared using 80 mL of a 9:1 volumetric mixture of dibutyl ether:THF. The mixture was heated to boiling under a nitrogen atmosphere and stirred at 140 °C for 20 hours using a condensing column to retain the solvent. The now yellow solution was then cooled to room temperature and the product was crystalized using a rotary evaporator, leaving a yellow-green solid. The solid was purified using a silica column with a 2:1 mixture of diethyl ether and hexanes as the mobile phase, leaving a yellow band at the top of the column. This band was then flushed out using methanol, and the resulting solution was rotary evaporated yielding BCECT, a yellow solid, as confirmed by the distinct FTIR peaks at 1960 cm^{-1} and 1878 cm^{-1}, corresponding to the symmetric and asymmetric stretching modes of the carbonyls.

5.2.3 Sample Preparation

In order to easily prepare many different mixtures of BCECT and sodium salts, three stock solutions in THF were prepared: 50 mM BCECT, 150 mM sodium thiocyanate, and 100 mM sodium tetraphenylborate. The proper volumes of NaSCN and BCECT solution were combined and diluted with THF to yield 1:2, 1:1, 3:2, 4:1, and 8:1 mixtures with a constant BCECT concentration of 10 mM. A solution of 1:1 $NaBPh_4$ and BCECT was prepared as well as a solution of only BCECT in THF. These solutions also had a BCECT concentration of 10 mM. The 250 µL samples were placed in a sample cell consisting of two 25 mm x 3 mm calcium fluoride windows separated by a 100 µm Teflon spacer.

5.2.4 FTIR Measurements

FTIR spectra were collected using the sample preparation described above on a JASCO FT/IR-4100 spectrometer. The spectra were baseline corrected by subtracting a 4^{th}-order polynomial and then normalized to the absorbance of the symmetric carbonyl band in BCECT at around 1960 cm^{-1}.

5.2.5 2D-IR Details

The 2D-IR experimental setup has been described elsewhere previously.[18-20] Spectra were collected with a waiting time ranging from -0.2 to 1.0 ps in steps of 0.1 ps, 1.25 to 10 ps in steps of 0.25 ps, and 10.5 to 30 ps in steps of 0.5 ps. The Frequency Fluctuation Correlation Function (FFCF) was calculated using the inhomogeneity index method:[21]

$$C(t) = \sin\left[\frac{\pi}{2}\left(\frac{A_R - A_{NR}}{A_R + A_{NR}}\right)\right]$$

where A_R and A_{NR} are the moduli of the rephasing and nonrephasing signals, respectively, integrated over the spectral range of interest at each waiting time. The resulting points are fit to an offset exponential decay to extract the spectral diffusion timescale. The resulting offsets are adjusted so that the correlation function with the lowest offset decays to a value of zero.

5.2.6 Electronic Structure Calculations Setup

All Density Functional Theory (DFT) calculations were performed in the Gaussian 09 software suite[22] using the B3LYP functional. The 6-31+G(d) basis set was used for all atoms except for chromium, which was modeled using the LANL2DZ effective core potential and basis set. Calculations performed in a self-consistent reaction field were done using a polarizable continuum model with the default properties of tetrahydrofuran.

5.3 Results and Discussion

5.3.1 FTIR Results

The labeled crown ether and sodium thiocyanate were first studied using Fourier Transform Infrared (FTIR) spectroscopy to compare the samples and concentrations used to those previously reported. Figure 5.1 shows the normalized spectra of the carbonyl and thiocyanate stretching modes of several different mixtures of Benzo-18-Crown-6 Ether Chromium Tricarbonyl (BCECT) and sodium thiocyanate. All samples had a BCECT concentration of 10 mM and the NaSCN concentration varied from 0 mM to 80 mM. The spectra were all normalized to the absorbance of the symmetric CO stretch of BCECT around 1960 cm^{-1}. The absorbance of the asymmetric CO stretch (centered around 1878 cm^{-1}) remained fairly constant, although the width increases until the concentration of NaSCN reaches 15 mM at which point additional sodium thiocyanate does not affect the peak width. This may indicate that the asymmetric CO band is an indicator of how much NaSCN is coordinated to the crown ether, as the high binding constant means almost all of the sodium ions should be coordinated to the crown ether and so assuming a 1:1 complex, additional NaSCN shouldn't affect the CO backbonding, as the additional ion pairs are solvated separately from the BCECT.

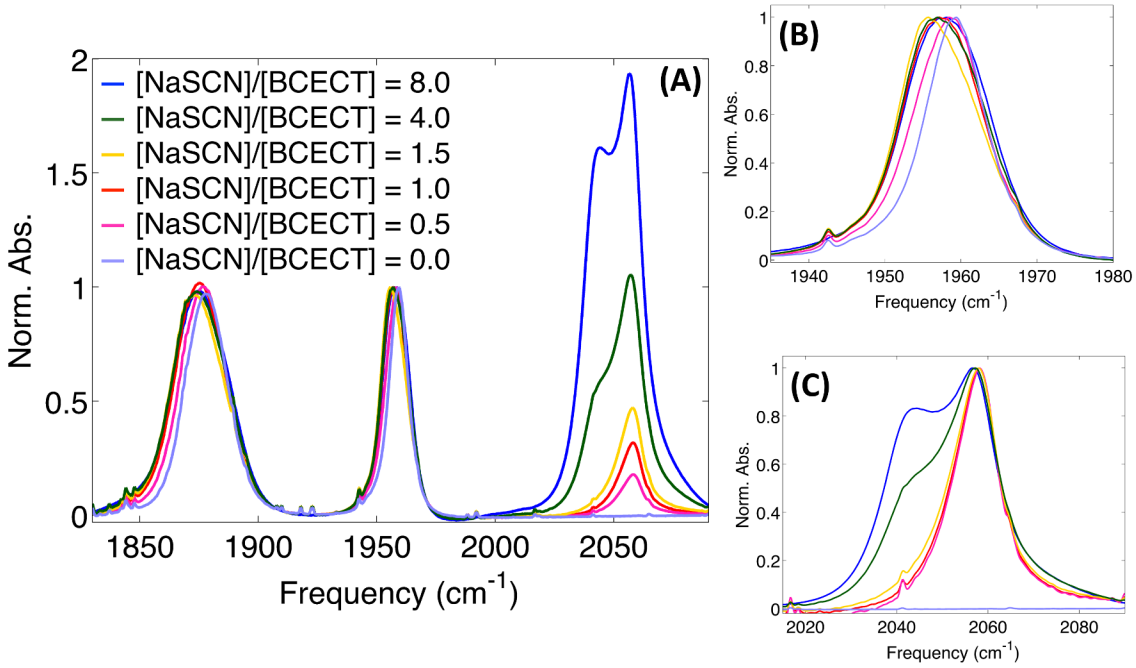

Figure 5.1 FTIR spectra of carbonyl and thiocyanate frequencies of BCECT and NaSCN in THF normalized to the symmetric CO stretching mode near 1960 cm^{-1}. The molar ratio of NaSCN to BCECT used is shown in blue (8.0), green (4.0), yellow (1.5), red (1.0), pink (0.5), and purple (0.0). The symmetric CO stretching mode redshifts with increasing NaSCN concentration, as shown in (*B*). (*C*) shows the NaSCN band normalized to the contact ion pair peak near 2060 cm^{-1}. The peak near 2040 cm^{-1} that grows in is assigned to NaSCN dimers.

The asymmetric band in a similar chromium tricarbonyl molecule was previously observed[23] to broaden in more polar solvents, as the different environments split the degeneracy of the two different asymmetric CO stretching modes in the band. The band was even observed to separate into two distinct peaks in a small unilamellar vesicle, likely due to a nearby ion. For BCECT, all of the nearby ions will be contact ion pairs, so the effective charge that reaches the carbonyls is less than an unpaired ion. This further supports the 1:1 complex, as the difference between 1.5:1 and 8:1 NaSCN:BCECT is minimal, suggesting there is no change in the electron density in the crown ether and no nearby ions to split the degenerate peaks.

Another feature of the FTIR spectra, as shown in Figure 5.1B, is that the symmetric CO mode redshifts as the relative concentration of sodium thiocyanate is increased. This shift is in the opposite direction as the frequency shift observed in the complex formed between benzo-15-crown-5 ether chromium tricarbonyl and sodium

perchlorate in methanol.[16] The reason for the difference in the shift is that sodium perchlorate is not expected to form many contact ion pairs in methanol,[4] so the majority of the complexed sodium cations will be unpaired, resulting in a greater withdrawal of electron density from the aromatic group, reducing the amount of π-backbonding and blueshifting the carbonyl frequencies. Instead, the presence of a thiocyanate anion with the cation causes the frequency to redshift, as supported by quantum chemical calculations that will be discussed further below. To confirm that the blueshifting of the carbonyl bands was due to solvent-separated ion pairs and not a unique feature of the benzo-15-crown-5 chromium tricarbonyl, a solution of 10 mM BCECT and 10 mM sodium tetraphenylborate in THF was prepared and its FTIR spectrum is shown in Figure 5.2. The FTIR spectra show that the carbonyl modes blueshift in the presence of the solvent-separated ion pairs, and the asymmetric band is broader than the solution with just BCECT.

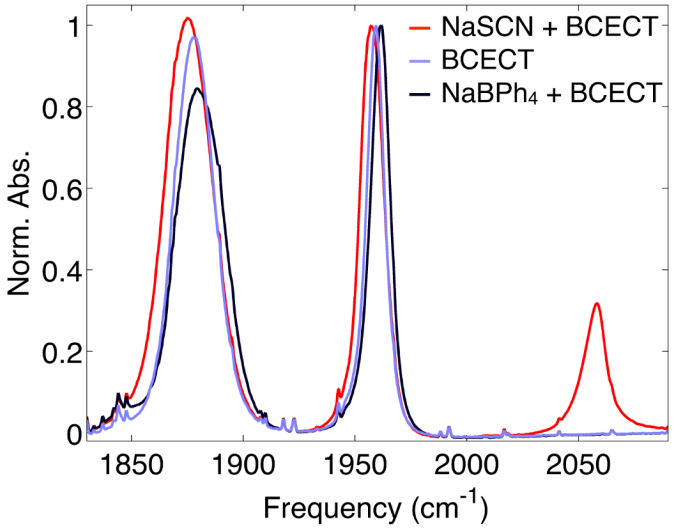

Figure 5.2 FTIR spectra of the carbonyl and thiocyanate bands of BCECT and two different sodium salts, normalized to the symmetric carbonyl peak around 1960 cm^{-1}. 10 mM BCECT in THF is shown in purple, a 1:1 mixture of BCECT and NaSCN is shown in red and a 1:1 mixture of BCECT and $NaBPh_4$ is shown in black. The carbonyl bands redshift when NaSCN is added and blueshift when $NaBPh_4$ is added.

Another striking change in the FTIR spectra is that the shape of the thiocyanate band (near 2060 cm^{-1}) changes greatly as the NaSCN:BCECT ratio increases from 1.5:1 to 4:1 as shown in Figure 5.1C. The reason for this change is that as the thiocyanate

concentration increases, the ions form larger groups than just contact ion pairs. The peak at 2057 cm^{-1} is assigned to thiocyanate in a contact ion pair, while the peak at 2043 cm^{-1} is assigned to a sodium thiocyanate dimer by Saar and Petrucci.[1] The relative intensity of the two bands is different with BCECT than the previously reported spectra, with more intensity associated with contact ion pairs than the dimers. This has been interpreted as the presence of the crown ether interrupting the formation of dimers.[24] However, sodium thiocyanate will begin to dimerize when the concentration exceeds that of the crown ether by at least 4:1, as seen in Figure 5.1C. An additional peak from sodium thiocyanate in THF is expected at 1973 cm^{-1}, attributed to a thiocyanate ion in contact with two sodium cations,[1] but typically only appears at high concentrations and is much weaker than the other two, which could explain the shoulder on the blue side of the SCN band seen in the 4:1 and 8:1 mixtures.

5.3.2 2D-IR Spectra

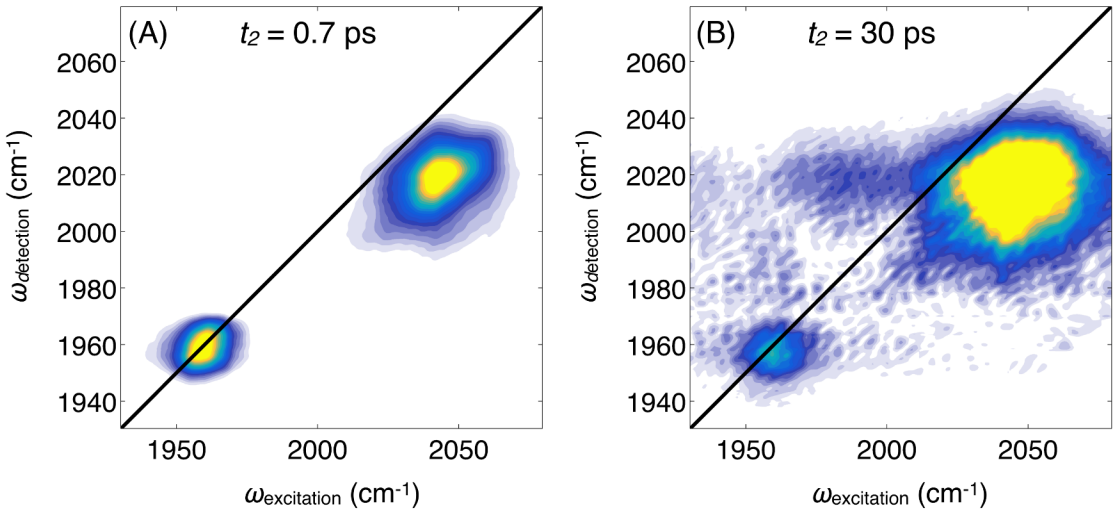

Figure 5.3 2D-IR spectra of 10 mM BCECT and 80 mM NaSCN in THF, with the symmetric carbonyl mode of BCECT at 1960 cm^{-1} and the excited state absorption band of NaSCN at an excitation frequency of 2050 cm^{-1} just below the diagonal. (*A*) shows the spectrum at an early waiting time, t_2 = 0.7 ps when the two bands have similar intensity. (*B*) shows the spectrum at a later waiting time, t_2 = 30 ps where the SCN band is much more intense, indicating that SCN has a longer vibrational lifetime. No cross-peaks are present, indicating that energy is not exchanged between the two modes.

The linear infrared spectra provide a good deal of information about the system, but little is known about the dynamics, where the system could be undergoing changes

on the ultrafast timescale. It has been previously observed that while the linear infrared spectrum of a probe may appear similar or even identical, the ultrafast dynamics can be vastly different.[25, 26] The initial goal of this system was to monitor both the carbonyl and thiocyanate modes, but as seen in Figure 5.3, the detection bandwidth of the 2D-IR setup is not broad enough to resolve both the symmetric mode of the carbonyls and the thiocyanate band. The excited state absorption band from the thiocyanate modes is visible because it inherently has a lower frequency than the diagonal band, which is composed of the signal corresponding to the ground state bleach and stimulated emission pathways.[27] Despite only being able to see one diagonal peak in the 2D-IR spectra, the symmetric carbonyl mode should provide insight into the dynamics of the system as other piano-stool complexes have been used previously.[23, 28, 29]

5.3.3 Spectral Diffusion Gives Insight to the Complex

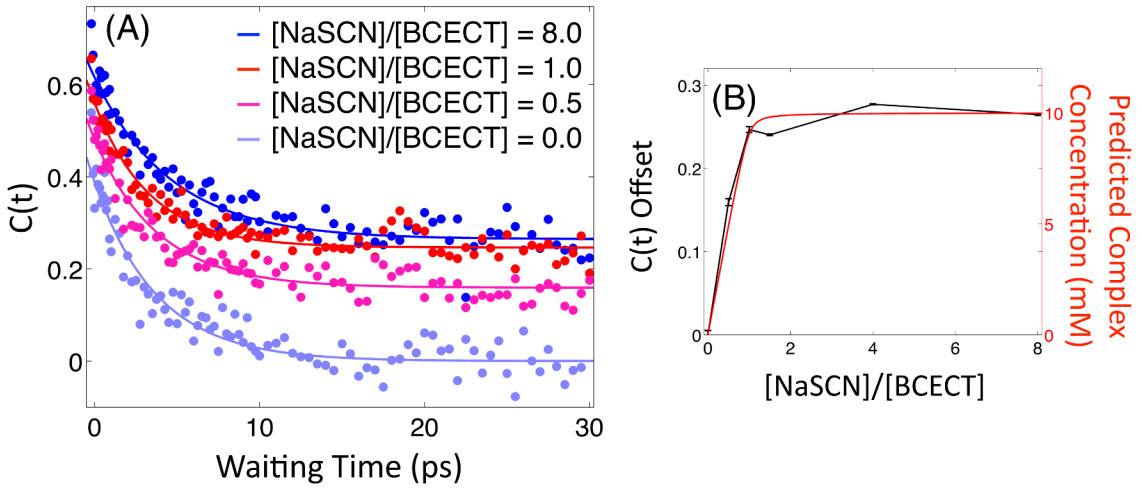

Figure 5.4 (*A*) FFCF of symmetric CO mode for four different mixtures of NaSCN and BCECT. The offset increases as the concentration of NaSCN increases. (*B*) The offset from the FFCF fits correlate well with the expected complex concentration given an binding constant of 10^4 M^{-1}.

The FFCF can be used to sense how quickly a probe samples the distribution of environments that produce the varying frequencies and has been used to provide insight into the dynamics of a wide variety of systems from labeled proteins[30-32] to catalysts.[33-35] The FFCF was measured for the symmetric CO mode of BCECT and shown in Figure 5.4A for several different mixtures of BCECT and NaSCN. The striking difference

between the 4 different FFCF shown is that the offset increases with increased sodium thiocyanate concentration. The increase saturates at slightly above a 1:1 mixture as shown by the small increase in offset between 1:1 and 8:1, where there is a large excess of NaSCN. This offset indicates that there is some dynamical process(es) that occur on timescales slower than the experimentally accessible window limited by the finite (12 ps) vibrational lifetime of the probe. The precise origin of the long-time dynamics cannot be determined from the FFCF alone, but based on the structural considerations discussed above, a likely explanation would involve the complexation of NaSCN to BCECT. Indeed, the change in offset is well correlated with the expected concentration of complex formed assuming an equilibrium constant of 10^4 M^{-1}, as shown in Figure 5.4B.

The correlation of the offset with the formation of BCECT/NaSCN complex makes it easy to speculate about the origin of the offset—either because of the coordination of the sodium cation to the crown ether or the presence of the thiocyanate ion due to contact ion pair formation. To investigate the origin of the offset, sodium tetraphenylborate was again used to separate the contribution of the sodium cation and the thiocyanate anion by providing a source of solvent-separated sodium that will coordinate to the crown ether separately from the bulky tetraphenylborate anion. The FFCF of a 1:1 mixture of BCECT and $NaBPh_4$ is shown in Figure 5.5 in black, where the offset (0.09) is a little higher than the offset of pure BCECT in THF (0.0), but still considerably lower than a 1:1 mixture of BCECT and NaSCN (0.25). This seems to show that the majority of the long-time dynamics is due to the presence of the thiocyanate anion and not the coordination of the sodium cation to the crown ether.

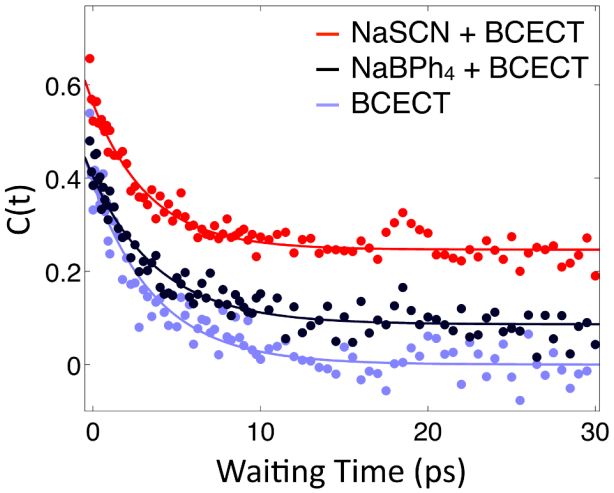

Figure 5.5 FFCF of symmetric CO mode of BCECT with $NaBPh_4$ in comparison to a sample of just BCECT and with NaSCN, showing that while there is a small increase in offset from the sodium coordinating to the crown ether, the majority comes from the thiocyanate anion.

Table 5.1 FFCF decay time for solutions with varying concentration ratios of NaSCN and BCECT.

[NaSCN]/[BCECT]	C(t) Decay Time (ps)
0.0	3.78 ± 0.39
0.5	3.82 ± 0.38
1.0	3.34 ± 0.32
1.5	4.99 ± 0.15
4.0	3.76 ± 0.12
8.0	4.65 ± 0.13

It is interesting to note that the addition of sodium thiocyanate or sodium tetraphenylborate has very little effect on the spectral diffusion timescale of the symmetric carbonyl mode of BCECT. All of the FFCFs for BCECT and NaSCN have a decay time between 3 and 5 ps with no apparent trend with increasing salt concentration as shown in Table 5.1. The solution with BCECT and $NaBPh_4$ has a FFCF decay time of 3.96 ± 0.33 ps, which is in the same range as the NaSCN solutions. Although it is difficult to say too much about the system from this, it seems to indicate that the introduction of excess salt does not change the environment of the carbonyl, so the dimers or additional contact ion pairs are likely forming far from the BCECT in solution. Also, the

increase in offset does not affect the spectral diffusion timescale, so the new environment being created by the addition of NaSCN is sampled at about the same rate as that of just BCECT in THF.

5.3.4 Investigating the System with DFT

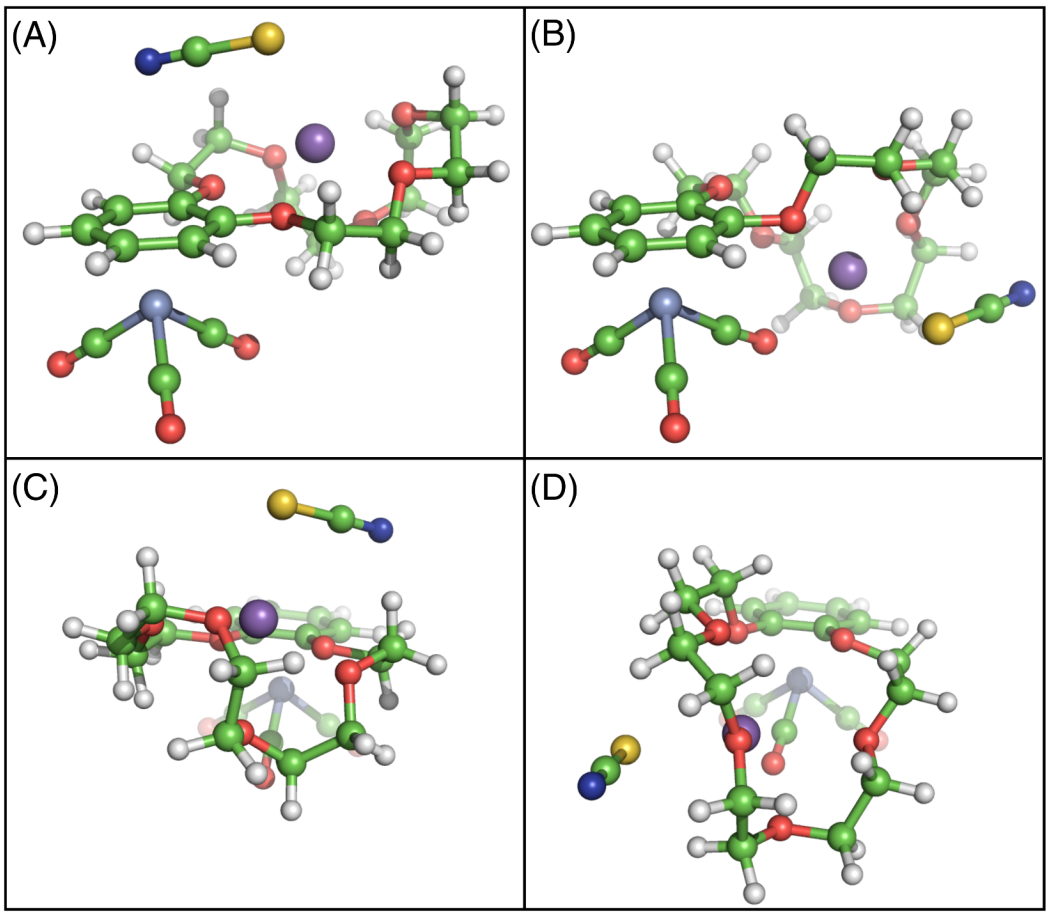

Figure 5.6 DFT optimized geometries for the BCECT and NaSCN complex with the thiocyanate located (A) and (C) above, or on the opposite side of the crown ether than the carbonyls and (B) and (D) below, or on the same side of the crown ether as the carbonyls. The two structures are both expected to be present due to the small energy difference between the two.

DFT calculations were used to model the system and better understand the origin of the FFCF offset using the B3LYP/6-31+G(d) level of theory on all atoms except for chromium, which was represented with the LANL2DZ basis set and effective core potential using the Gaussian 09 software suite.[22] These quantum chemical calculations allow geometries, frequencies, and energies to be calculated based on the electronic structure of a molecule or ion. The crystal structure of the complex between benzo-15-

crown-5 chromium tricarbonyl and sodium thiocyanate has been determined[16] and has the thiocyanate anion located "above" the crown ether, or on the opposite side as the metal and carbonyls. A similar structure was optimized for BCECT and is shown in Figure 5.6A, as well as a structure where the thiocyanate is "below" the crown ether – on the same side as the carbonyls as shown in Figure 5.6B. These structures have similar energies – only a difference of 5.13 kJ/mol, where the structure with thiocyanate above the crown ether is lower in energy. Assuming a Boltzmann distribution, this means that about 13% of the complexes would have the thiocyanate below the crown ether. The energy difference between these two states may be even lower in solution, as placing the complex in a THF solvent cavity and optimizing the two geometries gives an energy difference of 2.56 kJ/mol, but the conformation with the thiocyanate below the crown ether has the lower energy. Either way, it looks like a combination of the two conformations will be present at room temperature, which could cause the offset in the FFCF.

Table 5.2 Calculated BCECT and NaSCN Frequencies (cm^{-1}, unscaled)

Molecule	$\nu^{asym\ 1}$(CO)	$\nu^{asym\ 2}$(CO)	ν^{sym}(CO)	ν^{CN} (SCN)
BCECT	1982	1987	2045	-
BCECT + Na^+	1897	2015	2060	-
BCECT + NaSCN above	1952	1979	2035	2157
BCECT + NaSCN below	1969	1999	2051	2157

A harmonic frequency calculation was performed for both BCECT/NaSCN complex structures as well as BCECT with a sodium cation coordinated to the crown ether and BCECT by itself. The unscaled frequencies are listed in Table 5.2 and show the trends observed in the FTIR spectra – the carbonyl frequencies generally blueshift when complexed with an unpaired sodium cation and the carbonyl frequencies generally redshift when a thiocyanate anion is included in the calculation. When an unpaired sodium cation is complexed, the lowest frequency asymmetric mode redshifts, but the total splitting of the asymmetric mode (98 cm^{-1}) is much larger than experimentally

observed, so the redshifting is likely the result of an unrealistically unshielded positive charge from the sodium. For the BCECT/NaSCN complex with the thiocyanate below the crown ether, the higher frequency asymmetric CO mode and symmetric CO mode are both blueshifted from the frequencies of BCECT, although the average of the asymmetric CO modes is redshifted by 0.2 cm^{-1}. These frequency shifts could be reduced in the real system where solvent molecules would likely be shielding the carbonyls from the charges on the sodium and thiocyanate ions.

The sizeable difference in symmetric CO frequency between having the thiocyanate anion above or below the crown ether could be the source of the FFCF offset, as the thiocyanate would take longer to travel from one side of the crown ether to the other than the vibrational lifetime of the BCECT, which is about 12 ps. The distance between the thiocyanate anions when superimposing the two complex structures is about 10 Å. The time for a thiocyanate anion to travel this distance in THF can be calculated using the Stokes-Einstein equation with a radius of 1.5 Å for SCN^-, yielding a time of about 100 ps, which is an order of magnitude longer than the vibrational lifetime of the probe, so this motion would not be observable in 2D-IR.

5.4 Conclusions

A combination of spectroscopic and computational efforts revealed new details about a combination of two well-studied systems. The FFCF of the symmetric CO band in BCECT was observed to have an increasing offset as more sodium thiocyanate was added, roughly at the same rate as the formation of the complex. The offset indicates that there are frequency environments in the band that are not accessible on the timescale of the probe's vibrational lifetime. Modeling the system with DFT revealed that two different structures, one with the thiocyanate anion on the opposite side of the crown ether as the carbonyls and another with it on the same side, were similar in energy, but gave different carbonyl frequencies. Because of the low energy difference between the conformations, both are expected to be present in solution, but the time

required for the thiocyanate to travel from one side of the crown ether to the other is an order of magnitude longer than the vibrational lifetime of the carbonyl.

5.5 Acknowledgements

Tyler Elias synthesized and purified the BCECT as well as performed some of the DFT calculations.

5.6 References

1. Saar, D.; Petrucci, S., Infrared and Ultrasonic Spectra of Sodium Thiocyanate and Lithium Thiocyanate in Tetrahydrofuran. *J. Phys. Chem.* **1986,** *90*, 3326-3330.

2. Firman, P.; Xu, M.; Eyring, E. M.; Petrucci, S., Thermodynamics of Dimerization of Nascn in Some Acyclic Polyethers Studied by Infrared-Spectroscopy. *J. Phys. Chem.* **1992,** *96*, 8631-8639.

3. Chabanel, M.; Wang, Z., Vibrational Study of Ionic Association in Aprotic-Solvents .6. Dimerization of Lithium, Sodium, and Potassium Isothiocyanate Ion-Pairs in Tetrahydrofuran and in 1,3-Dioxolane. *J. Phys. Chem.* **1984,** *88*, 1441-1445.

4. Erlich, R. H.; Popov, A. I., Spectroscopic Studies of Ionic Solvation .10. Study of Solvation of Sodium Ions in Nonaqueous Solvents by Na-23 Nuclear Magnetic Resonance. *J. Am. Chem. Soc.* **1971,** *93*, 5620-5623.

5. Bian, H. T.; Chen, H. L.; Li, J. B.; Wen, X. W.; Zheng, J. R., Nonresonant and Resonant Mode-Specific Intermolecular Vibrational Energy Transfers in Electrolyte Aqueous Solutions. *J. Phys. Chem. A* **2011,** *115*, 11657-11664.

6. Bian, H. T.; Li, J. B.; Zhang, Q.; Chen, H. L.; Zhuang, W.; Gao, Y. Q.; Zheng, J. R., Ion Segregation in Aqueous Solutions. *J. Phys. Chem. B* **2012,** *116*, 14426-14432.

7. Bian, H. T.; Wen, X. W.; Li, J. B.; Chen, H. L.; Han, S. Z.; Sun, X. Q.; Song, J. A.; Zhuang, W.; Zheng, J. R., Ion clustering in aqueous solutions probed with vibrational energy transfer. *Proc. Natl. Acad. Sci. U. S. A.* **2011,** *108*, 4737-4742.

8. Szczygiel, P.; Shamsipur, M.; Hallenga, K.; Popov, A. I., NMR-Study of the Exchange Kinetics of the Sodium-Ion with Some 18-Crowns in Tetrahydrofuran Solutions. *J. Phys. Chem.* **1987,** *91*, 1252-1255.

9. Xu, M. Z.; Eyring, E. M.; Petrucci, S., Molecular-Dynamics and Infrared-Spectra of Nascn Dissolved in the Solvent Macrocycle 15-Crown-5 and Polyethylene Oxide Dimethyl Ether-250. *J. Phys. Chem.* **1995,** *99*, 14589-14596.

10. Kamitori, S.; Hirotsu, K.; Higuchi, T., Crystal and Molecular-Structures of Double Macrocyclic Inclusion Complexes Composed of Cyclodextrins, Crown Ethers, and Cations. *J. Am. Chem. Soc.* **1987,** *109*, 2409-2414.

11. Lin, J. D.; Popov, A. I., Nuclear Magnetic-Resonance Studies of Some Sodium-Ion Complexes with Crown Ethers and [2]Cryptands in Various Solvents. *J. Am. Chem. Soc.* **1981,** *103*, 3773-3777.

12. Gokel, G. W.; Goli, D. M.; Minganti, C.; Echegoyen, L., Clarification of the Hole-Size Cation-Diameter Relationship in Crown Ethers and a New Method for Determining Calcium Cation Homogeneous Equilibrium Binding Constants. *J. Am. Chem. Soc.* **1983,** *105*, 6786-6788.

13. Amor, A. B. H.; Top, S.; Meganem, F.; Jaouen, G., Selective functionalization of crown ethers via arene chromium tricarbonyl complexes. *J. Organomet. Chem.* **2005,** *690*, 847-856.

14. Geldbach, T. J.; Brown, M. R. H.; Scopelliti, R.; Dyson, P. J., Ruthenium-benzocrownether complexes: Synthesis, structures, catalysis and immobilisation in ionic liquids. *J. Organomet. Chem.* **2005,** *690*, 5055-5065.

15. Pannell, K. H.; Hambrick, D. C.; Lewandos, G. S., Dibenzo-18-Crown-6-Tricarbonylchromium Compounds - Synthesis and Substituent Derived Reversal of Ion Extraction Selectivity. *J. Organomet. Chem.* **1975,** *99*, C21-C23.

16. Anson, C. E.; Creaser, C. S.; Stephenson, G. R., [(η(6)-Benzocrown ether)Cr(CO)(3)] Complexes as FTIR-readable Molecular Sensors for Alkali Metal Cations. *J. Chem. Soc., Chem. Commun.* **1994**, 2175-2176.

17. Mahaffy, C. A. L.; Pauson, P. L., (η-6-Arene)Tricarbonylchromium Complexes. *Inorg. Synth.* **1990,** *28*, 136-147.

18. Nee, M. J.; McCanne, R.; Kubarych, K. J.; Joffre, M., Two-dimensional infrared spectroscopy detected by chirped pulse upconversion. *Opt. Lett.* **2007,** *32*, 713-5.

19. Nee, M. J.; Baiz, C. R.; Anna, J. M.; McCanne, R.; Kubarych, K. J., Multilevel vibrational coherence transfer and wavepacket dynamics probed with multidimensional IR spectroscopy. *J. Chem. Phys.* **2008,** *129*, 084503.

20. Baiz, C. R.; Mcrobbie, P. L.; Anna, J. M.; Geva, E.; Kubarych, K. J., Two-Dimensional Infrared Spectroscopy of Metal Carbonyls. *Acc. Chem. Res.* **2009,** *42*, 1395-1404.

21. Roberts, S.; Loparo, J.; Tokmakoff, A., Characterization of spectral diffusion from two-dimensional line shapes. *J. Chem. Phys.* **2006,** *125*, 084502.

22. Frisch, M. J.; Trucks, G. W.; Schlegel, H. B.; Scuseria, G. E.; Robb, M. A.; Cheeseman, J. R.; Scalmani, G.; Barone, V.; Mennucci, B.; Petersson, G. A.; Nakatsuji, H.; Caricato, M.; Li, X.; Hratchian, H. P.; Izmaylov, A. F.; Bloino, J.; Zheng, G.; Sonnenberg, J. L.; Hada, M.; Ehara, M.; Toyota, K.; Fukuda, R.; Hasegawa, J.; Ishida, M.; Nakajima, T.; Honda, Y.; Kitao, O.; Nakai, H.; Vreven, T.; Montgomery Jr., J. A.; Peralta, J. E.; Ogliaro, F.; Bearpark, M. J.; Heyd, J.; Brothers, E. N.; Kudin, K. N.; Staroverov, V. N.; Kobayashi, R.; Normand, J.; Raghavachari, K.; Rendell, A. P.; Burant, J. C.; Iyengar, S. S.; Tomasi, J.; Cossi, M.; Rega, N.; Millam, N. J.; Klene, M.; Knox, J. E.; Cross, J. B.; Bakken, V.; Adamo, C.; Jaramillo, J.; Gomperts, R.; Stratmann, R. E.; Yazyev, O.; Austin, A. J.; Cammi, R.; Pomelli, C.; Ochterski, J. W.; Martin, R. L.; Morokuma, K.; Zakrzewski, V. G.; Voth, G. A.; Salvador, P.; Dannenberg, J. J.; Dapprich, S.; Daniels, A. D.; Farkas, Ö.; Foresman, J. B.; Ortiz, J. V.; Cioslowski, J.; Fox, D. J. *Gaussian 09, Revision A.02*, Gaussian, Inc.: Wallingford, CT, USA, 2009.

23. Osborne, D. G.; Dunbar, J. A.; Lapping, J. G.; White, A. M.; Kubarych, K. J., Site-Specific Measurements of Lipid Membrane Interfacial Water Dynamics with Multidimensional Infrared Spectroscopy. *J. Phys. Chem. B* **2013,** *117*, 15407-15414.

24. Xu, M. Z.; Eyring, E. M.; Petrucci, S., Infrared and Microwave Dielectric Spectra of Macrocycle Electrolyte Complexes - Nascn+18c6 in Thf. *J. Phys. Chem.* **1986,** *90*, 6125-6129.

25. King, J. T.; Ross, M. R.; Kubarych, K. J., Ultrafast alpha-Like Relaxation of a Fragile Glass-Forming Liquid Measured Using Two-Dimensional Infrared Spectroscopy. *Phys. Rev. Lett.* **2012,** *108*, 157401.

26. King, J. T.; Baiz, C. R.; Kubarych, K. J., Solvent-Dependent Spectral Diffusion in a Hydrogen Bonded "Vibrational Aggregate". *J. Phys. Chem. A* **2010,** *114*, 10590-10604.

27. Ogilvie, J. P.; Kubarych, K. J., Multidimensional Electronic and Vibrational Spectroscopy: An Ultrafast Probe of Molecular Relaxation and Reaction Dynamics. *Advances in Atomic, Molecular, and Optical Physics, Vol 57* **2009,** *57*, 249-321.

28. Nilsen, I. A.; Osborne, D. G.; White, A. M.; Anna, J. M.; Kubarych, K. J., Monitoring equilibrium reaction dynamics of a nearly barrierless molecular rotor using ultrafast vibrational echoes. *J. Chem. Phys.* **2014,** *141*.

29. Osborne, D. G.; King, J. T.; Dunbar, J. A.; White, A. M.; Kubarych, K. J., Ultrafast 2DIR Probe of a Host-Guest Inclusion Complex: Structural and Dynamical Constraints of Nanoconfinement. *J. Chem. Phys.* **2013,** *138*, 144501.

30. Bloem, R.; Koziol, K.; Waldauer, S. A.; Buchli, B.; Walser, R.; Samatanga, B.; Jelesarov, I.; Hamm, P., Ligand Binding Studied by 2D IR Spectroscopy Using the Azidohomoalanine Label. *J. Phys. Chem. B* **2012,** *116*, 13705-13712.

31. Woys, A. M.; Mukherjee, S. S.; Skoff, D. R.; Moran, S. D.; Zanni, M. T., A Strongly Absorbing Class of Non-Natural Labels for Probing Protein Electrostatics and Solvation with FTIR and 2D IR Spectroscopies. *J. Phys. Chem. B* **2013,** *117*, 5009-5018.

32. King, J. T.; Arthur, E. J.; Brooks, C. L.; Kubarych, K. J., Site-Specific Hydration Dynamics of Globular Proteins and the Role of Constrained Water in Solvent Exchange with Amphiphilic Cosolvents. *J. Phys. Chem. B* **2012,** *116*, 5604-5611.

33. Rosenfeld, D. E.; Gengeliczki, Z.; Smith, B. J.; Stack, T. D.; Fayer, M. D., Structural dynamics of a catalytic monolayer probed by ultrafast 2D IR vibrational echoes. *Science* **2011,** *334*, 634-9.

34. Bandaria, J. N.; Dutta, S.; Nydegger, M. W.; Rock, W.; Kohen, A.; Cheatum, C. M., Characterizing the dynamics of functionally relevant complexes of formate dehydrogenase. *Proc. Natl. Acad. Sci. U. S. A.* **2010,** *107*, 17974-17979.

35. Kiefer, L. M.; Kubarych, K. J., Solvent-Dependent Dynamics of a Series of Rhenium Photoactivated Catalysts Measured with Ultrafast 2DIR. *J. Phys. Chem. A* **2015,** *119*, 959-965.

Chapter 6

Conclusions and Future Directions

6.1 Introduction

The debate over the role of structural dynamics on the reactivity of enzymes is ongoing and unlikely to end soon, with evidence continuing to be produced both supporting[1-5] and refuting[6-10] the idea that vibrational motion is important to enzyme catalysis. This debate is not over the larger, slower dynamics where substrate binding causes conformational change in a protein, such as the opening and closing of the active site, but the coupling of ultrafast motion to the reaction coordinate, especially the transition state.[1, 6] Regardless of which side is correct, the argument highlights that, despite the numerous advances made, we lack a complete understanding of what makes enzymes such powerful catalysts. A better understanding of enzyme catalysis can be reached through a combination of experimental and computational study, where protein design can be led by computational modeling and unexpected experimental results will necessitate refinement of the model and a more complete picture of the catalysis.[11]

Electrostatics are known to be a dominant factor in enzyme function,[12] so the ability to reliably modify and detect changes in the electrostatic environment of a protein is needed to precisely pinpoint the electrostatic contribution to catalysis. *De novo* metalloenzymes provide an excellent opportunity to test our ability to modify the electrostatic environment and may be labeled with vibrational probes to detect these modifications. Vibrational probes give insight not only into the *de novo* peptide, but also other systems such as the Hofmeister series and complexation of cations to crown ethers. Computational models can provide insights into the structure of these smaller systems and lead to more efficient sampling of the design space for new enzymes.

6.2 *de novo* Peptides

In Chapter 2, a vibrationally labeled *de novo* metalloenzyme was studied using 2D-IR, yielding spectra with well-resolved anharmonicity. This anharmonicity appears to be waiting time dependent, but the anharmonicity change is actually the coalescence of the two 2D-IR bands due to nonequilibrium dynamics, suggesting a coupling of the carbonyl stretching mode with lower frequency degrees of freedom. The system was investigated using DFT, but no hidden coordinate was found until a more sophisticated modeling technique, ONIOM, was used. These QM/MM calculations revealed the Cu-C-O bending mode to be coupled to the CO stretching mode, but the coupling is only evident when including the electrostatic contributions from the enzyme. The coupling of the two modes was found to be linked to the dihedral angle of the histidine side-chains bound to the copper atom, which twist in response to the macromolecule's electric filed, such as that provided by the α-helical coiled-coil motif of the enzyme.

In Chapter 3, the *de novo* design space was explored computationally by modeling two series of mutants. In the first series, we tested the influence of having the carbonyl bond aligned opposite in direction to the original calculations (towards the C-terminus) by replacing L-histidine with D-histidine. Additionally, the active site was relocated to different heptads to investigate the influence of the larger scale scaffold. In the second series, mutations to the active site and nearby residues were considered by replacing natural histidine with methylated histidine side chains, and the leucine residue near the carbonyl was replaced with the significantly smaller alanine. Methods for obtaining a better minimized starting structure for the ONIOM calculations were implemented, including the calculation of force field parameters previously not included for the copper. From the resulting ONIOM calculations, a peptide was selected to be studied using 2D-IR based on the expected anharmonicity change. The peptide was chosen because it exhibits one of the largest predicted differences in the coupling between the CO stretching and Cu-C-O bending modes and has the highest nitrite reductase activity of any peptide in either series.[13] The 2D-IR spectra showed a smaller amplitude decay for this new peptide, as predicted by the calculations.

This project has really only scratched the surface of what can be studied both experimentally and computationally. The first step should be to minimize all of the structures discussed in Chapter 3 using the calculated copper parameters. This will provide a more meaningful comparison for predicted Cu-C-O angle changes, and with them apparent anharmonicity decay from the experimental data. Additionally, now that MD simulations can easily be run using the calculated parameters, the structures from several snapshots during the simulation can be minimized and compared with ONIOM. If the different structures have a large range of CO frequencies, it would explain the large inhomogeneous linewidth of the 2D-IR spectrum.

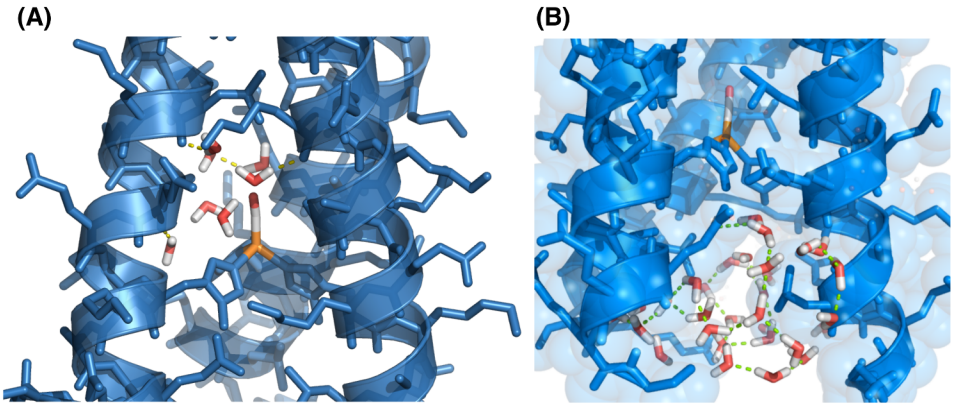

Figure 6.1 Snapshots from MD simulations showing the presence of water (A) within 5 Å of the metal carbonyl and (B) at the bottom of the hydrophobic cavity.

Another point of consideration for the simulations is that up to this point, any water has been removed prior to MM minimization, resulting in a large number of salt bridges. Oppositely charged lysine and glutamic acid residues that are normally solvated are attracted to each other and in the absence of water will form these salt bridges. The water could easily be retained and included in the ONIOM MM layer, potentially leading to a structure more similar to the crystal structure 3PBJ, where fewer salt bridges are observed than the current ONIOM structures. The water could prove quite interesting in peptides with the L19A mutation, as a preliminary MD simulation shows the cavity above the carbonyl less crowded, as expected, but also more open to the solvent (Figure 6.1A). When solvating a structure without a carbonyl, initially a water molecule was placed in the open cavity, but was found to exit early in the MD simulation. Other water

molecules were seen entering and exiting the cavity as well. The MD simulations should provide insight into how solvent exposed the metal sites actually are, as well as insights to restrained water below the cavity (Figure 6.1B), where the carbonyl from TRIW-dH is expected to bind.

The next clear experimental step (after re-collecting the noisy TRIW-$_{\delta M}$HL19A data) is to study a peptide expected to show a larger anharmonicity decay than TRIW-H. The peptide choice should be supported by calculations first, as was done for the peptide in Chapter 3. Coupling between the CO stretching mode and Cu-C-O bending mode was observed in a DFT analogue of (imidazole)$_3$Cu(CO)$^+$ where the imidazole nitrogen not bound to copper was deprotonated. This protonation state would only physically occur at high pH values, but seems to show that increased electron density on the histidine side chain may enhance the coupling of two modes. Also, as a smaller anharmonicity change is seen when the nitrogen is bonded to a methyl group, which is electron donating, it would be interesting to see the effect of an electron-withdrawing group. For example, a halogen or nitrile group could be used, although this may not be feasible experimentally as synthesis routes to fluorinated or chlorinated histidine have not been investigated.

The long-term goal of this project should be to attempt modeling the reaction pathway of either CO_2 hydration using zinc as the metal or nitrite reduction keeping the metal a copper atom. A similar kind of QM/MM calculation will be necessary, but a more accurate technique may be needed. For example, Warshel et al. recommend *ab initio* QM/MM with reliable sampling.[11] Once the reaction pathway is better understood, it should be possible to make similar claims about predicted enzyme activity as are now being made about the apparent anharmonicity decay from 2D-IR.

6.3 Hofmeister Series and Cyclodextrin

Chapter 4 investigated another biologically relevant system with electrostatic interactions, the Hofmeister series, by monitoring the spectral diffusion of several thiocyanate salts in neat D_2O and with α-cyclodextrin. In neat D_2O the spectral diffusion

time constant of the thiocyanate CN stretching mode mostly followed the Hofmeister series, with NH_4^+ producing the fastest FFCF decay time, Na^+ an intermediate, and NBu_4^+ showing the slowest dynamics. The exception to the trend, Ca^{2+} was previously observed[14] to show a similar acceleration in water dynamics, but for reasons that are not fully understood. When α-CD is added to the solution, a host-guest complex is formed with the thiocyanate anion, resulting in a biexponential decay of the FFCF with an additional slow-decaying component. This change in the FFCF indicates that the nitrogen of SCN^- is solvent separated by the α-CD with the sulfur end of SCN^- solvent exposed.

The next step taken with this project should be to reduce the amount of scatter from the samples with α-CD to obtain more accurate decay times for the slower portion of the FFCF. This enhancement of signal-to-noise can be accomplished either through the "phase wobblers" described by Hamm et al.[15] that are ready to be implemented in our lab or the method of synchronously modulating the local oscillator and k_3 proposed by Massari et al.[16] Even if the scatter is eliminated, it is possible that no trend will exist for the SCN/α-CD decay times, as the salt concentrations used (50 mM) are much lower than the normal concentrations used to study the Hofmeister series (< 1 M). This difference in concentration could be overcome by adding another salt with the same cation and an anion that does not have a vibrational mode near thiocyanate and that is not extremely chaotropic or kosmotropic, such as chloride.

Alternatively, low concentrations could continue to be used and an "inverse Hofmeister series" could be investigated.[17-19] This inverse series was not observed in neat D_2O, but it could be that the trend has more to do with involvement with the protein than the water, in which case a trend could be observed with α-CD and SCN in solution. Whether the concentration is increased or not, the SCN/α-CD complex seems like an ideal system to study using the rapidly acquired spectral diffusion (RASD) method,[20] as there is only one mode present and the offset doesn't seem to contain any useful information. This would allow the decay time of the FFCF to be calculated in a fraction of the time with many more waiting time points collected.

6.4 Crown Ether and Sodium Thiocyanate

Another confined thiocyanate complex was studied in Chapter 5, in this case the contact ion pairs formed by sodium thiocyanate in THF were confined to a crown ether labeled with a metal carbonyl. The oxygen atoms on the crown ether donate electron density to the complexed sodium cation in the absence of thiocyanate and the resulting electron density loss is propagated to the vibrational probe, resulting in a blue shift in the carbonyl mode frequencies. When thiocyanate is present in solution the frequency redshifts, a trend that is reproduced in DFT calculations. 2D-IR spectra do not show any energy transfer between the thiocyanate and carbonyl modes. The FFCF offset for the symmetric CO stretching mode increases with increasing relative concentration of thiocyanate in solution, indicating dynamics that occur on time scales slower than the probe's vibrational lifetime of a few 10s of picoseconds. DFT calculations show two different conformations of the thiocyanate, above and below the crown ether, that give slightly different frequencies that are the likely the cause of the apparent static inhomogeneity.

This project is the closest to complete, as there are only a couple more details that need to be addressed. First, the FFCF of the SCN band should be calculated to compare with BCECTs. It seems intuitive that a similar offset would be expected as the addition of the crown ether creates additional microenvironments for the thiocyanate that will not be sampled on the timescale of the vibrational lifetime. However, because the only part of the SCN band present in the 2D spectrum is the 1-2 transition, it must first be shown that the 0-1 and 1-2 transitions show the same dynamics. This can be done using data collected on thiocyanate in THF with the frequencies tuned high enough to observe all of the SCN bands and not just the 1-2 transition.

6.5 References

1. Hay, S.; Scrutton, N. S., Good vibrations in enzyme-catalysed reactions. *Nat. Chem.* **2012,** *4*, 161-168.

2. Bhabha, G.; Lee, J.; Ekiert, D. C.; Gam, J.; Wilson, I. A.; Dyson, H. J.; Benkovic, S. J.; Wright, P. E., A Dynamic Knockout Reveals That Conformational Fluctuations Influence the Chemical Step of Enzyme Catalysis. *Science* **2011,** *332*, 234-238.

3. Henzler-Wildman, K.; Kern, D., Dynamic personalities of proteins. *Nature* **2007,** *450*, 964-972.

4. Johannissen, L. O.; Hay, S.; Scrutton, N. S., Nuclear quantum tunnelling in enzymatic reactions - an enzymologist's perspective. *Phys. Chem. Chem. Phys.* **2015,** *17*, 30775-30782.

5. Singh, P.; Abeysinghe, T.; Kohen, A., Linking Protein Motion to Enzyme Catalysis. *Molecules* **2015,** *20*, 1192-1209.

6. Tunon, I.; Laage, D.; Hynes, J. T., Are there dynamical effects in enzyme catalysis? Some thoughts concerning the enzymatic chemical step. *Arch. Biochem. Biophys.* **2015,** *582*, 42-55.

7. Glowacki, D. R.; Harvey, J. N.; Mulholland, A. J., Taking Ockham's razor to enzyme dynamics and catalysis. *Nat. Chem.* **2012,** *4*, 169-176.

8. Adamczyk, A. J.; Cao, J.; Kamerlin, S. C. L.; Warshel, A., Catalysis by dihydrofolate reductase and other enzymes arises from electrostatic preorganization, not conformational motions. *Proc. Natl. Acad. Sci. U. S. A.* **2011,** *108*, 14115-14120.

9. Thorpe, I. F.; Brooks, C. L., Barriers to hydride transfer in wild type and mutant dihydrofolate reductase from E-coli. *J. Phys. Chem. B* **2003,** *107*, 14042-14051.

10. Kamerlin, S. C. L.; Warshel, A., At the dawn of the 21st century: Is dynamics the missing link for understanding enzyme catalysis? *Proteins-Structure Function and Bioinformatics* **2010,** *78*, 1339-1375.

11. Frushicheva, M. P.; Mills, M. J. L.; Schopf, P.; Singh, M. K.; Prasad, R. B.; Warshel, A., Computer aided enzyme design and catalytic concepts. *Curr. Opin. Chem. Biol.* **2014,** *21*, 56-62.

12. Warshel, A.; Sharma, P. K.; Kato, M.; Xiang, Y.; Liu, H.; Olsson, M. H. M., Electrostatic basis for enzyme catalysis. *Chem. Rev.* **2006,** *106*, 3210-3235.

13. Yu, F. De novo designed metallopeptides with a type 2 copper center: a structural and functional model for copper nitrite reductase. University of Michigan, 2014.

14. Marcus, Y., Effect of Ions on the Structure of Water: Structure Making and Breaking. *Chem. Rev.* **2009,** *109*, 1346-1370.

15. Bloem, R.; Garrett-Roe, S.; Strzalka, H.; Hamm, P.; Donaldson, P., Enhancing signal detection and completely eliminating scattering using quasi-phase-cycling in 2D IR experiments. *OPTICS EXPRESS* **2010,** *18*, 27067-27078.

16. Spector, I. C.; Olson, C. M.; Huber, C. J.; Massari, A. M., Simple fully reflective method of scatter reduction in 2D-IR spectroscopy. *Opt. Lett.* **2015,** *40*, 1850-1852.

17. Zhang, Y. J.; Cremer, P. S., The inverse and direct Hofmeister series for lysozyme. *Proc. Natl. Acad. Sci. U. S. A.* **2009,** *106*, 15249-15253.

18. Bostrom, M.; Tavares, F. W.; Finet, S.; Skouri-Panet, F.; Tardieu, A.; Ninham, B. W., Why forces between proteins follow different Hofmeister series for pH above and below pI. *Biophys. Chem.* **2005,** *117*, 217-224.

19. Taratuta, V. G.; Holschbach, A.; Thurston, G. M.; Blankschtein, D.; Benedek, G. B., Liquid-Liquid Phase Separation of Aqueous Lysozyme Solutions - Effects of pH and Salt Identity. *J. Phys. Chem.* **1990,** *94*, 2140-2144.

20. Osborne, D. G.; Kubarych, K. J., Rapid and accurate measurement of the frequency-frequency correlation function. *J. Phys. Chem. A* **2013,** *117*, 5891-8.

Appendix

Additional Details About the *de novo* Metalloenzyme

A.1 Band position dynamics in a different peptide sequence

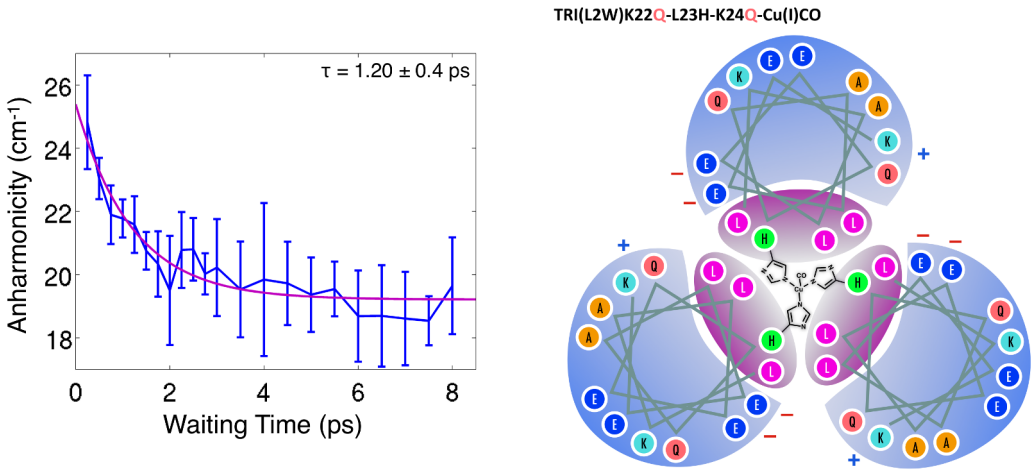

Figure A.1 Apparent anharmonicity decay (*left*) of the mutant TRIL2WK22QL23HK24Q (*right*). While the decay rate and amplitude are different than observed for the peptide described in the main text, the band coalescence is clearly present in both cases. Differences may be due to the change in local electrostatics due to the preponderance of negative charges .

Another *de novo* metalloenzyme was studied using 2D-IR spectroscopy in addition to the **TRI**L2WL23H that was the focus of the main discussion. The apo-peptide of this additional peptide has the sequence **TRI**L2WK22QL23HK24Q, which is similar to the peptide considered in the main text, except the positively charged lysine residues on either side of the histidine site where the copper ion binds are replaced with neutral glutamine residues. This change reduces the charge on the tripeptide metal carbonyl system from +1 to -5, as two positive charges are neutralized in each of the three coils. This metalloenzyme also displays a time dependent merging of the two bands, as shown in Figure A.1. The decay is faster than in the **TRI**L2WL23H enzyme (1.20 ± 0.4 ps) and changes by a larger amount (6.18 ± 1.2 cm^{-1}), but the presence of nonequilibrium

spectral dynamics in both peptides studied shows that it is not an exclusive feature of one mutation and implies that it is due to the more global structure of the peptide and not interaction with nearby charged residues. Moreover, given the attribution of the stretch-bend coupling to the histidine coordination, it would appear that modifying the charges on the external face of the peptide does not abolish the coupling. Rather, it may even be the case that the altered charge increases the coupling, resulting in a larger dynamical frequency shift.

A.2 Iron monocarbonyl complex shows no band merging dynamics

We wanted to discern if the band merging was a property of all transition metal mono-carbonyls, as we had not studied any before and this signature has not been reported previously. A small molecule iron carbonyl, $[Fe^{II}(CO)(N4Py)](ClO_4)_2$, provided by Kodanko *et al.*[1] was studied as it has a single carbonyl on a metal center coordinated to multiple nitrogen atoms, similar to the TRI-family peptide. The molecule is also similar to the myoglobin and hemoglobin carbonyls previously studied by other groups,[2, 3] but has a higher CO stretching frequency, 2009 cm^{-1}, that is closer to the copper carbonyl presented in the main text than the iron-containing proteins. The anharmonicity of the iron carbonyl is similar to the copper carbonyl, 21 cm^{-1}, but does not show the same band coalescence seen in the metalloenzyme, as seen in Figure A.2C-F.

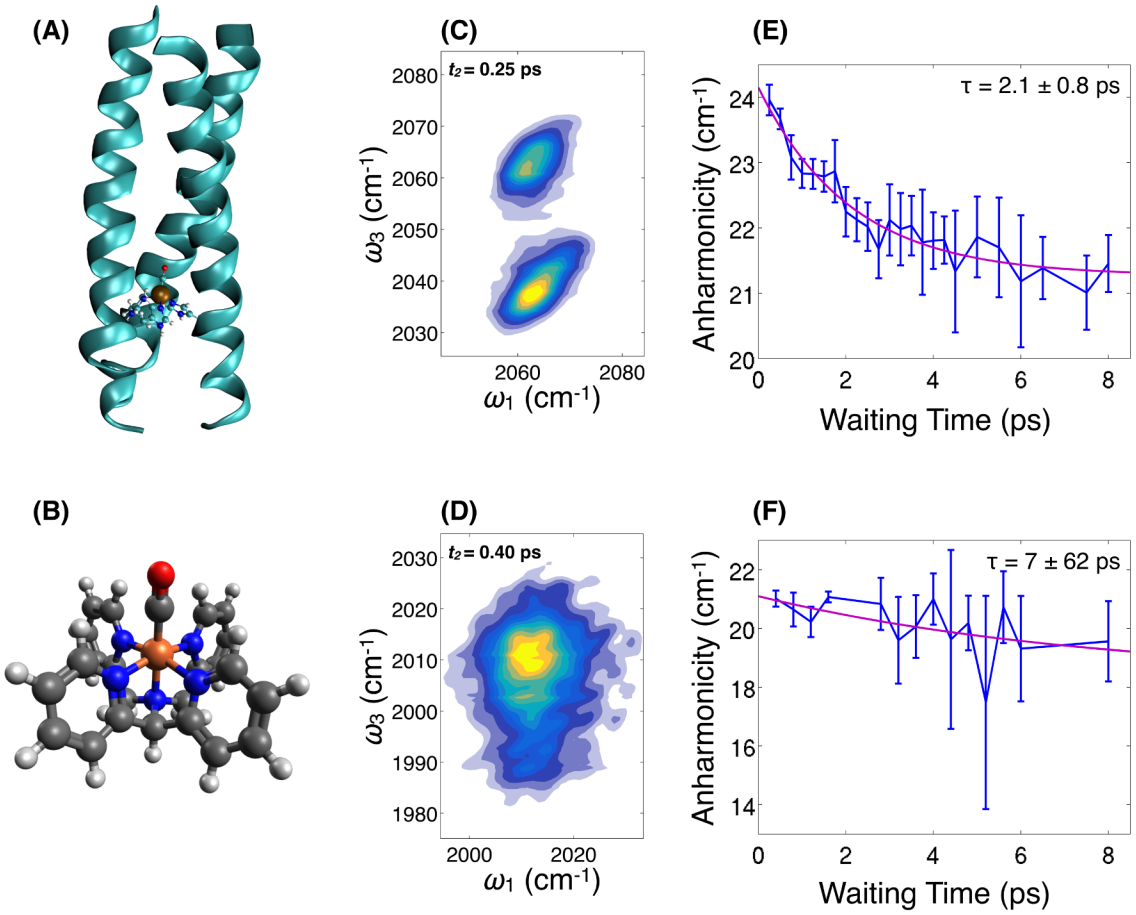

Figure A.2 (*A*) Structure of the copper peptide Cu(I)(TRIL2WL23H)$_3$(CO)$^+$ discussed previously. (*B*) Structure of the Fe(II)(N4Py)(CO)$^{2+}$ small monocarbonyl used for comparison. (*C*) 2D-IR spectrum of the copper peptide at a waiting time of 0.25 ps. (*D*) 2D-IR spectrum of the iron complex at a waiting time of 0.40 ps. The carbonyl has a similar anharmonicity, but the peak is more homogeneously broadened, indicating more solvent interaction and making the anharmonicity more difficult to determine. (*E*) Apparent anharmonicity decay of the copper carbonyl, for reference. There is clearly a change in the splitting of the two bands. (*F*) Apparent change in anharmonicity of the iron carbonyl. The anharmonicity does not change by a measurable amount as shown by the uncertainty in the decay time of the offset exponential.

When comparing the 2D-IR spectra of the copper peptide and the iron carbonyl, one of the clearest differences is that the lineshape of the iron complex is much more homogeneously broadened, which is attributed to the iron carbonyl being more solvent exposed than the copper carbonyl, which is in the hydrophobic interior of the coiled-coil structure. Although this homogeneous broadening lowers the resolution of the diagonal and off-diagonal peaks in the 2D-IR spectrum, it is still possible to determine the distance between the two bands, as shown in Figure A.2F. In this small iron complex the

carbonyl bands do not appreciably merge, as shown by the poor fitting exponential with a decay time uncertainty that is an order of magnitude larger than the decay time.

We note here that recent work by Hunt *et al*. has found evidence for nonequilibrium frequency dynamics in the heme site of catalase using the NO bound ligand as a vibrational probe.[4] In those studies, they observed frequency modulations as a function of the time delay in a IR/IR pump probe transient absorption spectroscopy. In addition to the frequency modulations, they also reported dynamics of the apparent anharmonicity. The results were interpreted in terms of a coupling to a water-mediate intermolecular interaction via a low-frequency motion, similar to the present case (though we see no oscillations). The identity of the low-frequency motion was not established, but presumably some approach similar to that taken here would be able to elucidate the detailed coupling and mechanism.

A.3 APBS and electric field calculations

The geometries used in the APBS calculations[5] were obtained from optimizing the geometry of the $(TRIL2WL23H)_3Cu(I)(CO)^+$ metalloenzyme using the same ONIOM scheme described earlier (B3LYP/6-311G(d,p):AMBER) with electronic embedding enabled. For each calculation, the Cu-C-O bond angle was frozen and the CO bond length was frozen at the ground (1.145 Å) or vibrationally excited length (1.260 Å) and the rest of the geometry was allowed to relax.

The electric field along the CO bond was analyzed using APBS by rotating the optimized coordinates to align the carbonyl with the z-axis. This produced a grid of electrostatic potential values and no interpolation was needed to determine electrostatic potential values along the carbonyl bond vector. Most of the charges used were the same as the default charges used in AMBER for standard amino acids.[6] The atoms included in the QM layer of the ONIOM calculation had charges assigned as generated by Gaussian according to the Merz-Singh-Kollman scheme for reproducing electrostatic potential.[7-9] Because the QM layer did not include the whole histidine residue, the total charge generated this way is not equal to 1.0, but is reasonably close,

1.64. Most of the radii were obtained using the PDB2PQR utility, but radii were not generated for the NH_2 groups, the metal carbonyl, or the hydrogen atoms in the methyl group of the acetyl caps. [10, 11] The radii used are listed in Table A.1.

Table A.1 Atomic radii used for atoms not generated by PDB2PQR

Residue Name	Atom	Radius (Å)
NH_2	N	1.824
	H	0.600
Acetyl	H	0.600
Metal Carbonyl	Cu	2.000
	C	1.908
	O	1.661

These radii are the same as radii generated in other residues, with the exception of the copper atom, which was estimated to be 2 Å. This seems reasonable because the copper has a partial positive charge, so while it is larger than the second-period elements it will not be as large as an uncharged copper atom. Separate PQR files were generated for each optimized structure. There were 40 in total, one for each angle from 160 to 179 degrees, inclusive, in steps of one degree for both the ground and excited state. The geometry was centered on the carbon in the metal carbonyl and the CO bond was aligned with the z-axis as described above. Both the coarse and fine grids had dimensions of 50.0 by 45.0 by 75.0 Å to include the entire peptide in the grid. The output electrostatic potential was a grid of 97 by 97 by 1601 points to give a resolution of 0.52 Å in the X dimension, 0.46 Å in the Y dimension, and 0.05 Å in the Z dimension. The increased resolution was necessary along the Z dimension to monitor changes in the electrostatic potential and accurately calculate the electric field.

The electrostatic potential output by APBS is in units of k_BT/e_c where k_B is the Boltzmann constant, T is the temperature, and e_c is the charge on an electron. All calculations were run at the default temperature of 298.15 K, so the resulting electrostatic potential was converted to mV and is shown in Figure A.3A. The

electrostatic potential is clearly dominated by the carbon and oxygen atoms of the carbonyl. The same calculations were performed with the charges on the CO set to zero to make a clearer electrostatic potential, shown in Figure A.3B. While indeed much cleaner, there still was a large influence from the nearby copper atom that affected the electrostatic potential, so the copper charge was also set to zero for the remaining calculations. The electrostatic potential shown in Figure A.3C is thus the result of only the atoms in the apo-peptide and not the metal carbonyl. The ground and vibrationally excited states have similar but different electrostatic potentials and should reveal a difference in the electric field present at the carbonyl site.

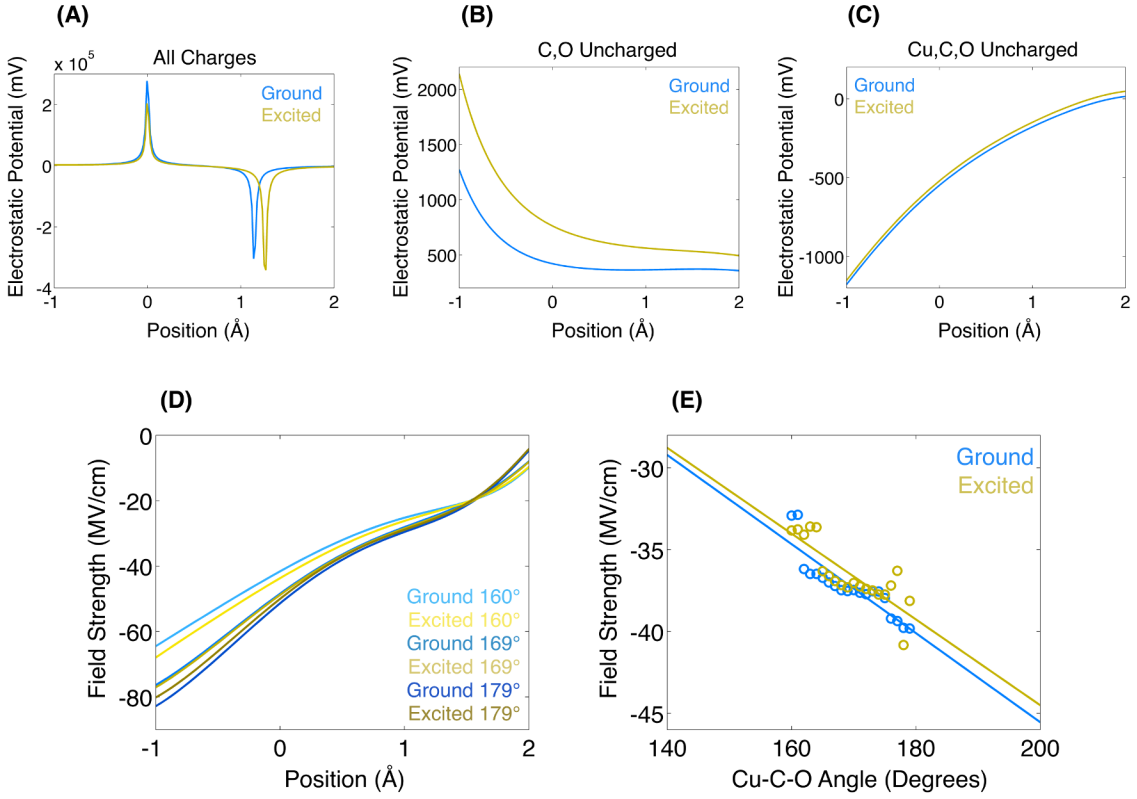

Figure A.3 (*A*) Electrostatic potential along the CO bond vector, centered on the carbon atom for both ground and vibrationally excited CO bond lengths. The potential is dominated by the carbon and oxygen atom charges. (*B*) The same electrostatic potential, but with the CO charges set to 0. There is still a noticeable influence from the copper atom. (*C*) Electrostatic potential with the Cu, C, and O atoms' charges set to zero. (*D*) Electric field strength along the carbonyl bond vector derived from electrostatic potential for three different Cu-C-O bond angles. (*E*) Average field strength at the carbon and oxygen positions as a function of Cu-C-O bond angle for the ground and vibrationally excited states.

The electric field strength was calculated from the electrostatic potential along the CO bond vector for the ground and excited states. These field strengths are shown for three different Cu-C-O bond angles in Figure A.3D. While all six fields have a similar shape and intensity, the general trend is that the ground state fields are weaker and the larger angles have stronger field strength. Taking the average of the field strength at the carbon and oxygen atom positions in the carbonyl provided a method of comparing the field strength for each angle. These values, shown in Figure A.3E, are mostly between -35 and -40 MV/cm and increase roughly linearly with increasing Cu-C-O bond angle. From the linear fits there is a difference of 2.51 MV/cm between the ground state optimized geometry (171.5° Cu-C-O angle) and the excited state optimized geometry (164.8°).

A.4 Vibrational excitation alters the charge distribution on CO: Partial Charges (Mulliken) on the Cu, C and O Atoms

Table A.2 Partial charges (Mulliken) on the Cu, C and O atoms of the copper site for the cases of no protein, with protein, and CO using two different bases. The lower level of theory is that used for the QM/MM calculations of the full peptide. The higher level of theory more faithfully captures the CO dipole moment in the ground state, whereas both return similar values for the extended geometry corresponding to the first vibrationally excited state.

	Ground (no protein)	Excite (no protein)	Ground (with protein)	Excite (with protein)	Free CO [B3LYP/6-311G(d,p)] Ground	Free CO [B3LYP/6-311G(d,p)] Excite	Free CO [B3LYP/6-311++G(2d,2p)] Ground	Free CO [B3LYP/6-311++G(2d,2p)] Excite
q(Cu), C	1.094350	1.119054	1.105311	1.129153	0.079896	0.13866	0.059075	0.136604
q(C), C	-0.135865	-0.116676	-0.163153	-0.143809	-0.079896	-0.13866	-0.059705	-0.136604
q(O), C	-0.124328	-0.195784	-0.193973	-0.273272	0.159792	0.27732	0.11878	0.273208
q(C) - q(O), C	-0.011537	0.079108	0.03082	0.129463	1.127	1.227	1.125692	1.2375
d_{CO}, Å	1.13577	1.24934	1.14543	1.25999	0.18008	0.34027	0.13370	0.33809
dipole moment, D	-0.010157	0.06331	0.02690	0.10274	0.07989	0.13866	0.05907	0.13660

A.5 Stark effect frequency shifts

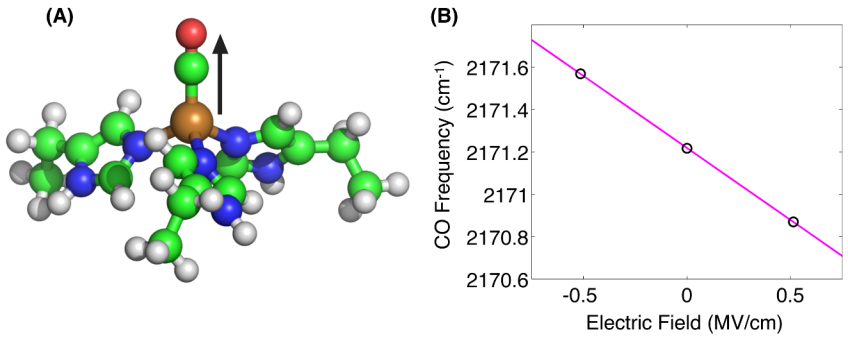

Figure A.4 (*A*) Geometry of the $Cu(EtIm)_3CO^+$ system with an arrow pointing in the direction of a positive applied electric field, aligned with the Cu-C bond vector. (*B*) Unscaled CO stretching frequencies from DFT calculations for three different applied electric field values. The magenta line is a linear fit of the three points that gives a Stark tuning rate of 0.7 cm^{-1}/(MV/cm).

The rather large electric field magnitude could provide a rationale for both the vibrational frequency shift and the coupling of the carbonyl stretching mode to the angle coordinate which drives the nonequilibrium dynamics. The argument is as follows: vibrational excitation alters the charge distribution on the CO (see partial charges above), causing it to realign in the field produced by the protein environment. In the new geometry, the projection of the field onto the CO bond changes, altering the frequency due to a Stark effect. In our model of the electric field, we find that the CO experiences a reduced electric field projection as the Cu-C-O angle deviates from 180°. In fact, the 6° geometrical change corresponds to a change in electric field magnitude of roughly -2 MV/cm, or 5% of the initial field magnitude. To estimate the frequency shift associated with the field change, we carried out vibrational Stark effect calculations by computing vibrational frequencies of optimized geometries of the smaller cluster $[Cu(EtIm)_3CO]$ in the presence of finite fields. Using field values of -0.5, 0, and +0.5 MV/cm oriented parallel to the CuCO bond in the field-free geometry, we obtained a linear Stark tuning rate of 0.68 cm^{-1}/(MV/cm), which, when combined with the electric field change, yields a 1.4 cm^{-1} frequency shift.[12] The discrepancy of a factor of 2 in the magnitude of the frequency shift is likely to be within the range of uncertainty in our electrostatic potential calculation, but given the general agreement with other CO Stark tuning rates, it is unlikely that our DFT derived Stark tuning rate is incorrect by such a

large magnitude. Instead of ascribing the majority of the frequency shift to a typical vibrational Stark effect, we argue below that the primary origin of the shift is the geometrical change, which is itself driven by the long-range electrostatics.

A.5.1. Calculation of Stark Tuning Rate

The Stark tuning rate of the carboxymetalloenzyme was estimated by performing geometry optimizations and frequency calculations on the small molecule analogue discussed previously with an applied electric field of varying strength using the Gaussian09 package. The dipole field was aligned with the Cu-C bond in the $Cu(I)(EtIm)_3(CO)^+$ system, pointing towards the oxygen atom in the carbonyl when the field was positive, as shown in Figure A.4A. Field strengths of +0.5 and -0.5 MV/cm were used and resulted in small shifts of the CO stretching frequency from the field-free frequency calculation, as shown in Figure A.4B.[12] A Stark tuning rate of 0.679 cm^{-1}/(MV/cm) was calculated by fitting the unscaled frequency change of these three points as a function of the electric field strength. This value should be reasonably close to the tuning rate of the actual peptide, and is accurate enough for the rough calculations we wanted to perform.

A.5.2. Application to APBS Results

We wanted to obtain frequency distributions of the 0-1 and 1-2 transitions of the CO stretching mode to characterize how the Stark effect would influence the bands observed with 2D-IR spectroscopy when only accounting for the Stark tuning rate. This was done using Cu-C-O bond angle distributions, the electric field present from the peptide at each angle, and the Stark tuning rate calculated previously. Two different angle distributions (Figure A.5B) were generated for the ground and excited state potential energy of the Cu-C-O bond angle, shown in Figure A.5A, by assuming a Boltzmann distribution for the Cu-C-O angle potentials at a temperature of 298.15 K. These two distributions correspond to equilibrium distributions for the ground and vibrationally excited states of the peptide. The angle distributions were converted to electric field distributions using the field mapping discussed previously and shown in

Figure A.3E. These field distributions were then translated into frequency distributions using the calculated Stark tuning rate of 0.68 cm^{-1}/(MV/cm). These frequency distributions were then centered around the 0-1 or 1-2 transition frequency to simulate the diagonal or off-diagonal peak present in the 2D-IR spectra.

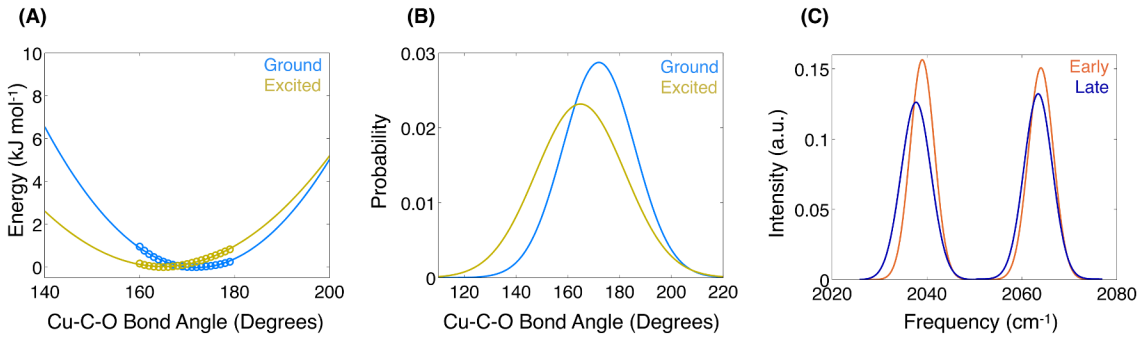

Figure A.5 (*A*) Potential energy of the Cu-C-O bond angle with ONIOM calculated energies shown as circles and quadratic fits shown as lines. The blue and yellow data refer to the ground and vibrationally excited states, respectively. (*B*) Boltzmann distributions at a temperature of 298 K for the ground and excited states. (*C*) In orange is the frequency distributions for the 0-1 and 1-2 transitions expected from the Stark tuning rate, the electric field strength as a function of Cu-C-O bond angle, and the bond angle distribution. In blue is the same frequency distribution after vibrational excitation and the angle distribution has had time to reach the excited distribution.

To simplify the frequency distribution calculations, two different situations were considered. First, early waiting times were considered, where molecules that propagate through the waiting time in the excited state do not relax to an equilibrium angle distribution. In this case, both the ground and excited state would be expected to have the same angle distribution. Both the 0-1 and 1-2 distributions are expected to have similar widths, as shown in Figure A.5C in the orange curve. The second situation is at later times, when the excited molecules have relaxed to an equilibrium angle distribution. This means that there are three total species to account for in the late time frequency distributions: molecules that spend the waiting time in the ground state and therefore will still have the ground state angle distribution and a center frequency of 2064 cm^{-1}. The other two frequency distributions are from molecules that propagate the waiting time in the excited state and are then either excited again, giving them a frequency near the normal 1-2 frequency, or undergo stimulated emission and have a frequency near the regular 0-1 frequency. Both of these later frequencies will be

redshifted by a few wavenumbers, as the excited equilibrium angle distribution is centered on an angle that has a less negative field present, so the frequencies are expected to be slightly less, as shown in Figure A.4B. The end result of this is shown in Figure A.5C as the blue peaks. Both peaks are redshifted, but because only part of the 0-1 peak frequencies are expected to redshift the entire band does not shift as much as the 1-2 peak. From this we would expect the 0-1 band to redshift by 0.57 cm^{-1} and the 1-2 band to redshift by 1.3 cm^{-1}, assuming the shift was due only to the change in electric field because of the Cu-C-O bond angle decreasing after vibrational excitation. Because the 1-2 band actually blueshifts, we suspect there are additional factors affecting the CO frequency, such as the geometry distortion upon excitation.

A.5.3. Comparison with heme proteins

From the work of Hochstrasser,[13] we can correlate Fe-C-O bond angle with the CO stretching frequency. Since small model compounds do not exhibit such distorted bond angles, we rely upon the protein environment to provide the distortion driving force.

Table A.3 Correlation of CO frequency and FeCO angle[13]

Species	MbCO	MbCO	HbCO
CO frequency (cm^{-1})	1933	1944	1951
FeCO angle (degrees)	157	174	172

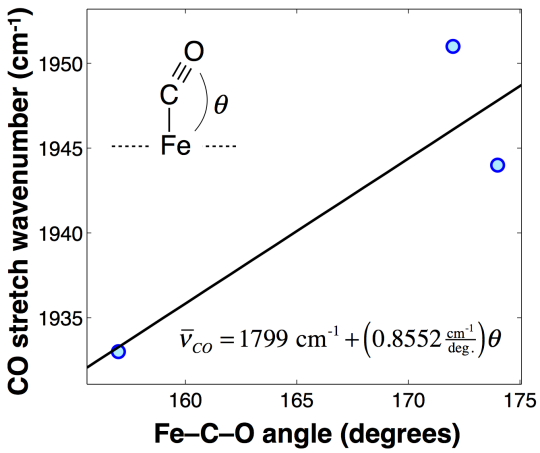

Figure A.6 Correlation between CO stretching frequency and the FeCO bond angle from Ref. 13. The fit allows a rough estimate of CO stretch for a given change in bond angle. In our case, we find a 6° bond tilt upon vibrational excitation, which would correspond to a 5 cm^{-1} frequency shift, which is similar to our 3-4 cm^{-1} observation.

A.6 Histidine Distortion in ONIOM and DFT Calculations

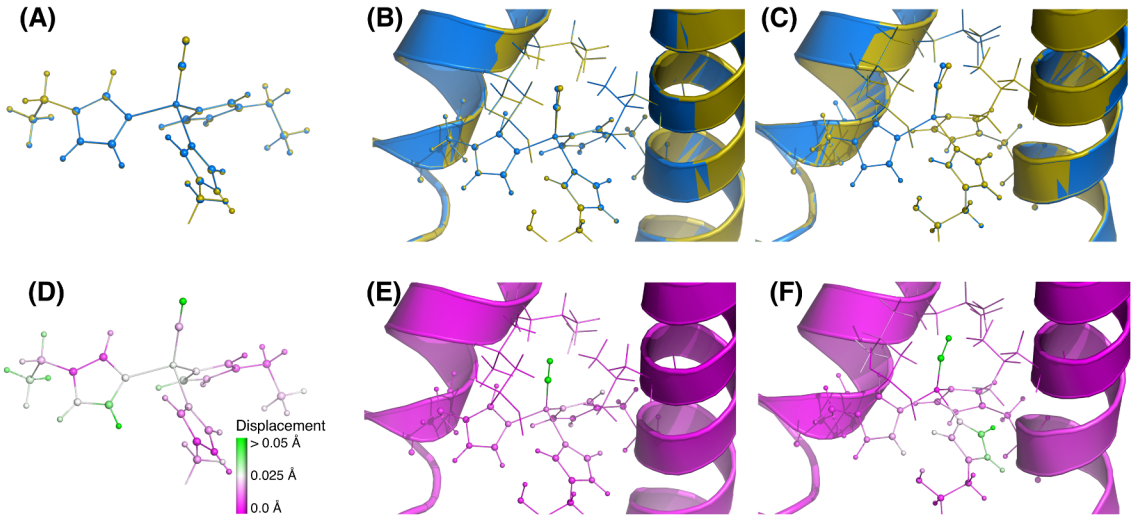

Figure A.7 The optimized structures of the ground (blue) and vibrationally excited (yellow) states for the small molecule analogue (*A*), peptide calculated with ONIOM without electronic embedding (*B*), and peptide modeled with ONIOM including electronic embedding (*C*). The average of those two structures are shown (*D-F*) color coded to show the amount of displacement upon vibrational excitation with pink atoms remaining stationary and green atoms having the greatest displacement.

As seen in Figure A.7, most of the non-carbonyl atoms in the vibrationally labeled peptide are not displaced when the CO stretching mode is excited. The atoms in the small molecule analogue are more easily displaced because the rigid peptide backbone is not present, but the change in geometry is still fairly small, with an RMSD of

0.023 Å for the non-carbonyl atoms, compared to 0.015 and 0.008 Å for the same atoms in the ONIOM geometries with and without electronic embedding, respectively. There does not appear to be an obvious geometrical change associated with the carbonyl tilting, such as a large change in the histidine-copper-carbonyl dihedral angle or the histidine-copper bond distance. The C_δ-N_ε-Cu-C dihedral angle does differ in each of the three cases pictured in Figure A.7 – the dihedral angles (in the ground state) for the small molecule are 48.9, 48.9, and 48.0°, in the ONIOM calculation without electronic embedding the angles are 59.8, 56.3, and 65.4°, and in the ONIOM calculation with electronic embedding the angles are 81.6, 57.6, and 79.8°. All nine of these angles change by less than 3 degrees upon vibrational excitation, meaning this difference would not be expected to have a significant on the Cu-C-O bond angle. This difference from excitation is especially small in comparison to the difference between the three different structures. The relationship between the dihedral angle and the Cu-C-O angle was explored by freezing the dihedral angle for each of the three ethylimidazole rings in the small molecule analogue and allowing the rest of the geometry to optimize. This was done for the ground state and the vibrationally excited state as described in the main text, resulting in the trend shown in Figure A.8.

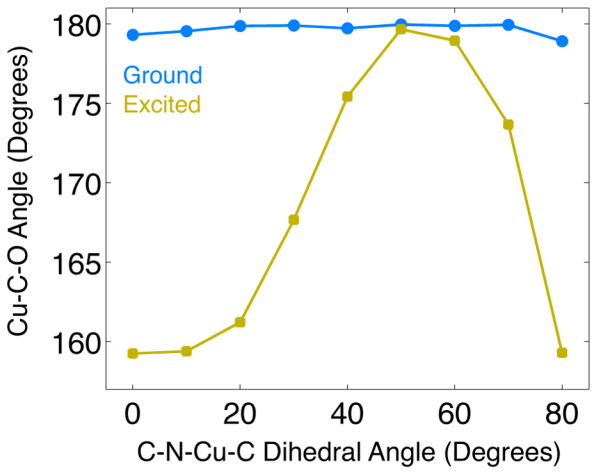

Figure A.8 Calculated Cu-C-O bond angles when the C-N-Cu-C dihedral angles are frozen at a particular value for the $(EtIm)_3CuCO$ small molecule analogue. The ground state shows little dependence on the dihedral angle, while the excited state changes considerably when the dihedral angle is sufficiently distorted.

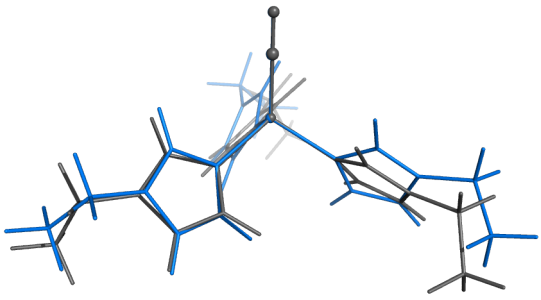

Figure A.9 Geometries of DFT optimized (grey) and dihedral angle constrained at 20° (blue) for the CO vibrational ground state. Despite the large change in His coordination, the Cu-C-O bond angle is not altered.

For fixed dihedral angles near the optimized angle (average 48.6° from the three rings), there was little difference in the Cu-C-O angle when the geometry was optimized with the carbonyl 10% longer. However, the coupling between the Cu-C-O tilting and CO stretching modes was greater when the dihedral became more distorted. From this small molecule DFT calculation alone, we would expect an angle difference of ~1° upon excitation for the dihedral angles from the ONIOM geometry without electronic embedding, when the actual angle was found to change by 2.8°. Similarly, the expected change given the dihedral angles from the ONIOM geometry with electronic embedding is ~10°, while the calculated difference is 6.7°. The small difference from the expected angle change is a reasonable error, considering the frozen dihedral angle calculations were performed on only the small molecule analogue and the dihedral angles were not allowed to change upon vibrational excitation.

A.7 Morse Potential Parameters

The Morse oscillator potential function is:

$$V(x) = D_e\left[\left(1 - e^{-a(x-x_e)}\right)^2 - 1\right] \qquad \text{(A1)}$$

where the two parameters are the dissociation energy, D_e, and the stiffness, a. The equilibrium position, x_e, is independently adjustable.

The solutions to the Morse oscillator eigenvalue problem are:

$$\psi_n(x) = z^{A\rho_n} \exp(-z)\, {}_1F_1(-n, 1+2A\rho_n, 2z) \qquad \text{(A2)}$$

in which the following definitions are made:

1. $$z = \frac{\sqrt{2D_e\mu}}{ah}\exp(-ax) \qquad \text{(A3)}$$

where *m* is the reduced mass and *h* is Planck's constant.

2. $$A = \frac{\sqrt{2\mu}}{ah} \qquad \text{(A4)}$$

3. $$\rho_n = \sqrt{D_e} - \frac{n+\frac{1}{2}}{A} \qquad \text{(A5)}$$

4. ${}_1F_1(-n, 1+2A\rho_n, 2z)$ is the confluent hypergeometric function of the first kind.

The energy eigenvalues are:

$$E_n = -D_e + hc\omega_e\left(n+\tfrac{1}{2}\right) - \frac{\left(hc\omega_e\right)^2}{4D_e}\left(n+\tfrac{1}{2}\right)^2 \qquad \text{(A6)}$$

where $\omega_e = \frac{a}{2\pi c}\sqrt{\frac{2D_e}{\mu}}$.

The values of the constants that yield the observed fundamental frequency and initial anharmonicity are:

$m = 1.1386 \times 10^{-26}$ kg

$a = 2.21$ Å^{-1}

$D_e = 1.803 \times 10^{-18}$ J

$x_e = 1.10$ Å

With these parameters, the $n = 0$ to $n = 1$ transition is 2063.24 cm^{-1}, and the anharmonicity is 23.9986 cm^{-1}.

The expectation values of position are found to be:

$$\langle x \rangle = \int_{-\infty}^{\infty} \psi_n^*(x)(x - x_e)\psi_n(x)dx \qquad \text{(A7)}$$

n = 0: $\langle x \rangle$ = 1.1476 Å

n = 1: $\langle x \rangle$ = 1.24885 Å

n = 2: $\langle x \rangle$ = 1.36014 Å

The change in bond length is therefore 1.24885 Å - 1.1476 Å = 0.10125 Å, which is roughly 10% of the *n* = 0 bond length.

A.8 Additional 2D-IR spectra

There is an increase in the noise in the spectra, especially at later times when the signal level is lower, but we do not expect that to have a significant effect on the fitted frequencies. To quantify this increase in noise, we compared the standard deviation of the fit residual for each detection-axis slice at each waiting time point for three different windows: 2020-2080 cm^{-1}, 1960-2020 cm^{-1}, and 2080-2140 cm^{-1} to get an idea of how noisy the spectra are along the region of interest compared to an equivalent range at lower and higher frequency. For an offset two-Gaussian function (one Gaussian for each peak, as used in the main text), the standard deviation is about 4 times higher in the range with our peaks than the background regions. When using two Gaussian functions for each peak with an offset, to better account for the lineshape, the standard deviation is reduced to less than twice that of the background region. Because of this, we do not feel the noise is substantially higher, or high enough to account for the frequency shifts.

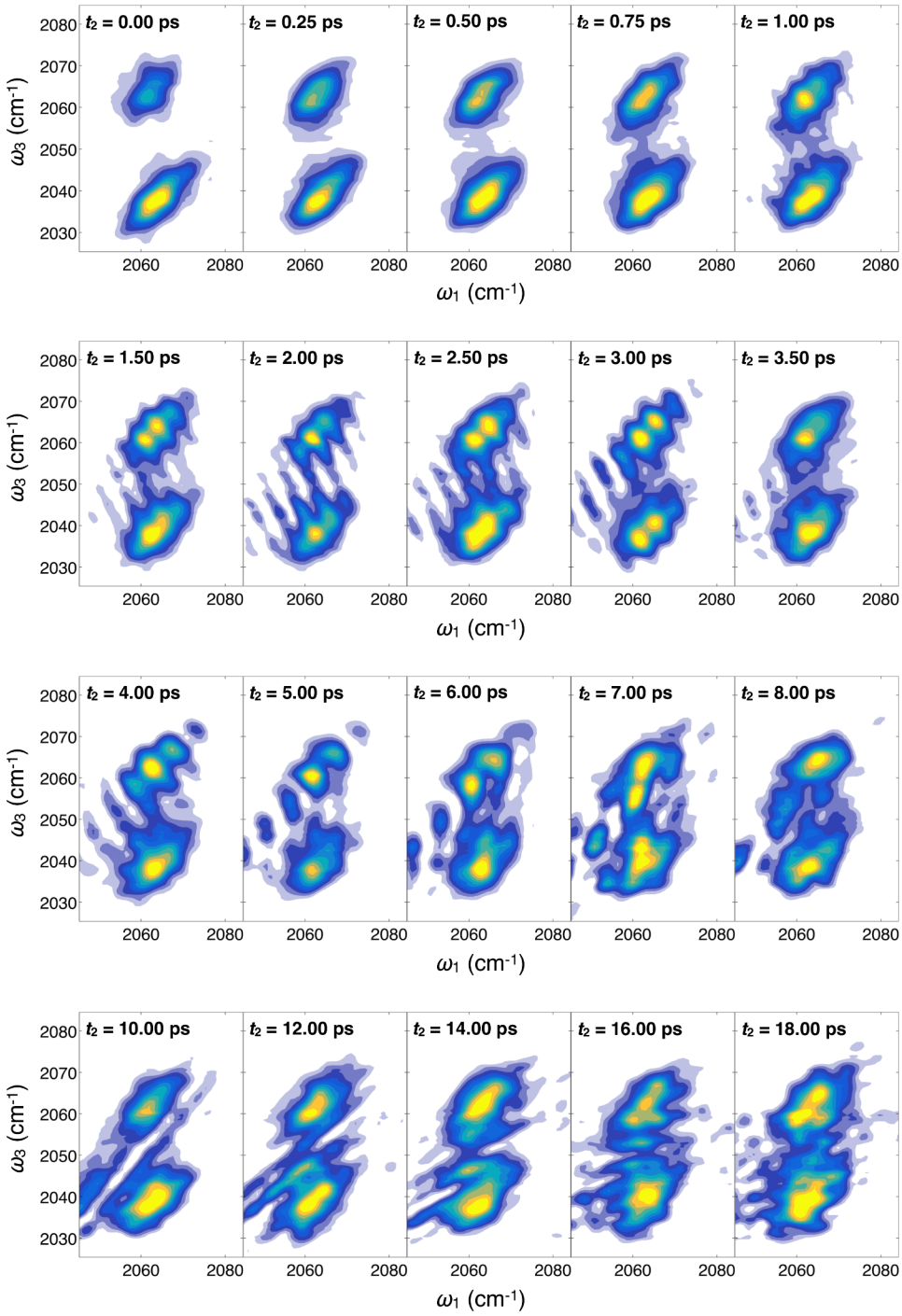

Figure A.10 Absolute magnitude 2D rephasing spectra of Cu(I)(TRIL2WL23H)$_3$(CO)$^+$ at various waiting times.

A.9 Determination of vibrational lifetime

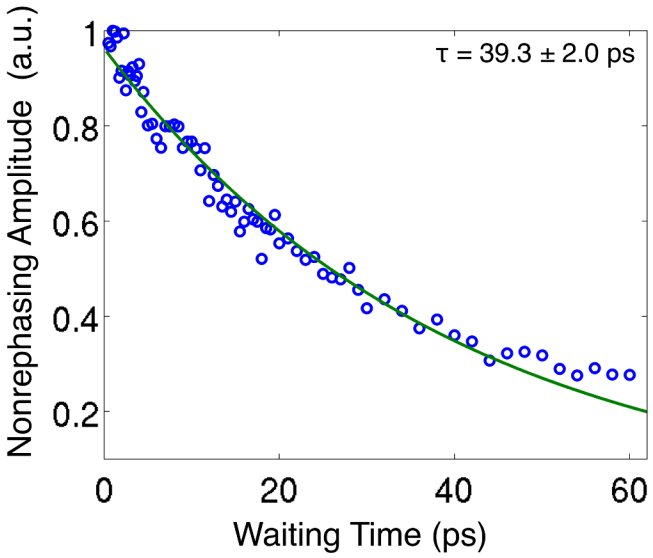

Figure A.11 The vibrational lifetime of the carbonyl was determined to be 39 ps by finding the decay time of the excited state absorption band in the nonrephasing spectra.

A.10 Calculation of Histidine Dipole Moment

The average atomic charges from the ONIOM calculations using the Merz-Singh-Kollman scheme for reproducing electrostatic potential [8, 9] are found to be comparable to the RESP charges obtained for the Cu_B site in cytochrome c oxidase, [14] shown in Table A.4. There is a greater charge separation, and thus a larger dipole moment, between the C_ε-H, C_δ-H, and N_δ-H pairs, which could produce increased hydrogen bonding to the carbonyl or nearby side chains. Using the charges above, plus the calculated atomic charge of 0.1827 *e* on the alpha-carbon, the dipole moment of each histidine residue was calculated from the center of the imidazole ring, as shown in Figure A.12. This average dipole moment of 3.6 D is large enough to induce a torque when exposed to the electric field of the peptide, distorting the C_δ-N_ε-Cu-C dihedral angle.

Table A.4 Average partial charges for atoms in histidine residues of Cu(I)(TRIL2WL23H)$_3$(CO)$^+$ (this work) and cytochrome c oxidase Cu$_B$ (Ref. 14)

Atom	TRI charge	CCO charge
CB	-0.4566	0.0971
HB1	0.0679	-0.0113
HB2	0.1253	-0.0113
CG	0.4615	0.1642
ND1	-0.5290	-0.1160
HD1	0.4383	0.0616
CE1	0.1454	-0.0109
HE1	0.2233	0.0088
NE2	-0.1904	0.1528
CD2	-0.4412	-0.2485
HD2	0.2642	0.1410
Cu	0.1546	-0.0741

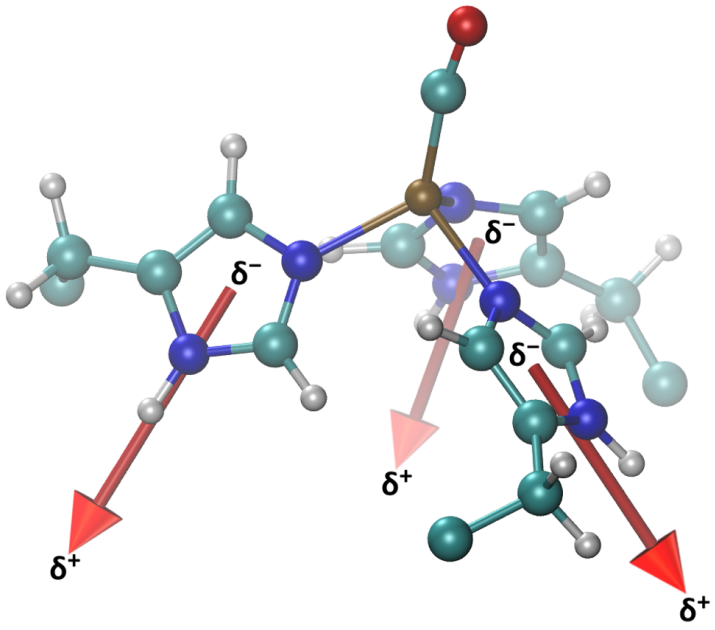

Figure A.12 Dipole moment of each histidine ring, in Cu(I)(TRIL2WL23H)$_3$(CO)$^+$ with average magnitude of 3.6 D

A.11 References

1. Jackson, C. S.; Schmitt, S.; Dou, Q. P.; Kodanko, J. J., Synthesis, Characterization, and Reactivity of the Stable Iron Carbonyl Complex [Fe(CO)(N4Py)](ClO4)(2): Photoactivated Carbon Monoxide Release, Growth Inhibitory Activity, and Peptide Ligation. *Inorg. Chem.* **2011,** *50*, 5336-5338.

2. Bagchi, S.; Nebgen, B. T.; Loring, R. F.; Fayer, M. D., Dynamics of a Myoglobin Mutant Enzyme: 2D IR Vibrational Echo Experiments and Simulations. *J. Am. Chem. Soc.* **2010,** *132*, 18367-18376.

3. Ventalon, C.; Fraser, J.; Vos, M.; Alexandrou, A.; Martin, J.; Joffre, M., Coherent vibrational climbing in carboxyhemoglobin. *Proc. Natl. Acad. Sci. U. S. A.* **2004,** *101*, 13216-13220.

4. Adamczyk, K.; Simpson, N.; Greetham, G. M.; Gumiero, A.; Walsh, M. A.; Towrie, M.; Parker, A. W.; Hunt, N. T., Ultrafast infrared spectroscopy reveals water-mediated coherent dynamics in an enzyme active site. *Chemical Science* **2015,** *6*, 505-516.

5. Baker, N. A.; Sept, D.; Joseph, S.; Holst, M. J.; McCammon, J. A., Electrostatics of nanosystems: Application to microtubules and the ribosome. *Proc. Natl. Acad. Sci. U. S. A.* **2001,** *98*, 10037-10041.

6. Cornell, W. D.; Cieplak, P.; Bayly, C. I.; Gould, I. R.; Merz, K. M.; Ferguson, D. M.; Spellmeyer, D. C.; Fox, T.; Caldwell, J. W.; Kollman, P. A., A Second Generation Force Field for the Simulation of Proteins, Nucleic Acids, and Organic Molecules. *J. Am. Chem. Soc.* **1995,** *117*, 5179-5197.

7. Frisch, M. J.; Trucks, G. W.; Schlegel, H. B.; Scuseria, G. E.; Robb, M. A.; Cheeseman, J. R.; Scalmani, G.; Barone, V.; Mennucci, B.; Petersson, G. A.; Nakatsuji, H.; Caricato, M.; Li, X.; Hratchian, H. P.; Izmaylov, A. F.; Bloino, J.; Zheng, G.; Sonnenberg, J. L.; Hada, M.; Ehara, M.; Toyota, K.; Fukuda, R.; Hasegawa, J.; Ishida, M.; Nakajima, T.; Honda, Y.; Kitao, O.; Nakai, H.; Vreven, T.; Montgomery Jr., J. A.; Peralta, J. E.; Ogliaro, F.; Bearpark, M. J.; Heyd, J.; Brothers, E. N.; Kudin, K. N.; Staroverov, V. N.; Kobayashi, R.; Normand, J.; Raghavachari, K.; Rendell, A. P.; Burant, J. C.; Iyengar, S. S.; Tomasi, J.; Cossi, M.; Rega, N.; Millam, N. J.; Klene, M.; Knox, J. E.; Cross, J. B.; Bakken, V.; Adamo, C.; Jaramillo, J.; Gomperts, R.; Stratmann, R. E.; Yazyev, O.; Austin, A. J.; Cammi, R.; Pomelli, C.; Ochterski, J. W.; Martin, R. L.; Morokuma, K.; Zakrzewski, V. G.; Voth, G. A.; Salvador, P.; Dannenberg, J. J.; Dapprich, S.; Daniels, A. D.; Farkas, Ö.; Foresman, J. B.; Ortiz, J. V.; Cioslowski, J.; Fox, D. J. *Gaussian 09, Revision A.02*, Gaussian, Inc.: Wallingford, CT, USA, 2009.

8. Besler, B. H.; Merz, K. M.; Kollman, P. A., Atomic Charges Derived from Semiempirical Methods. *J. Comput. Chem.* **1990,** *11*, 431-439.

9. Singh, U. C.; Kollman, P. A., An Approach to Computing Electrostatic Charges for Molecules. *J. Comput. Chem.* **1984,** *5*, 129-145.

10. Dolinsky, T. J.; Czodrowski, P.; Li, H.; Nielsen, J. E.; Jensen, J. H.; Klebe, G.; Baker, N. A., PDB2PQR: expanding and upgrading automated preparation of biomolecular structures for molecular simulations. *Nucleic Acids Res.* **2007,** *35*, W522-W525.

11. Dolinsky, T. J.; Nielsen, J. E.; McCammon, J. A.; Baker, N. A., PDB2PQR: an automated pipeline for the setup of Poisson-Boltzmann electrostatics calculations. *Nucleic Acids Res.* **2004,** *32*, W665-W667.

12. Franzen, S., An electrostatic model for the frequency shifts in the carbonmonoxy stretching band of myoglobin: Correlation of hydrogen bonding and the Stark tuning rate. *J. Am. Chem. Soc.* **2002,** *124*, 13271-13281.

13. Moore, J. N.; Hansen, P. A.; Hochstrasser, R. M., Iron Carbonyl Bond Geometries of Carboxymyoglobin and Carboxyhemoglobin in Solution Determined by Picosecond Time-Resolved Infrared Spectroscopy. *Proc. Natl. Acad. Sci. U. S. A.* **1988,** *85*, 5062-5066.

14. Tipmanee, V.; Blumberger, J., Kinetics of the Terminal Electron Transfer Step in Cytochrome c Oxidase. *J. Phys. Chem. B* **2012,** *116*, 1876-1883.